SLAC-R-668
UC-414

Measurement of the Average B Hadron Lifetime Using Reconstructed Vertices in Three-Dimensions*

Sumit Sen

Stanford Linear Accelerator Center
Stanford University
Stanford, CA 94309

SLAC-Report-668
January 1997

Prepared for the Department of Energy
under contract number DE-AC03-76SF00515

Printed in the United States of America. Available from the National Technical Information Service, U.S. Department of Commerce, 5285 Port Royal Road, Springfield, VA 22161.

- Ph.D. thesis, Yale University, New Haven, CT 06511

ABSTRACT

Measurement of the Average B Hadron Lifetime
Using Reconstructed Vertices in Three-Dimensions

Sumit Sen
January 17, 1997

This thesis describes a measurement of the average B hadron lifetime using data collected with the SLD detector at the Stanford Linear Collider in 1993. An inclusive analysis selects three-dimensional vertices with B hadron lifetime information in a sample of 50000 Z^0 decays. A lifetime of $1.564 \pm 0.030(\text{stat}) \pm 0.036(\text{syst})$ ps is extracted from the decay length distribution of these vertices using a binned maximum likelihood method.

Measurement of the Average B Hadron Lifetime Using Reconstructed Vertices in Three-Dimensions

A Dissertation
Presented to the Faculty of the Graduate School
of
Yale University
in Candidacy for the Degree of
Doctor of Philosophy

By
Sumit Sen

Disseration Director: C. Baltay

January 17, 1997

Acknowledgments

There are many people I would like to thank for their help and friendship during my graduate career.

I would like to thank my thesis advisor, Charlie Baltay, for the experience I have gained working with him. As his student I have sharpened my critical thinking and found inspiration in his intuitive approach to physics.

My deepest thanks to Steve Manly for his efforts in steering this analysis to completion. It would have been difficult to accomplish what I did without his ideas on vertexing, as well as his cheerfulness and willingness to help.

I am also grateful to Stéphane Willocq for his work on the analysis, and for his help in getting it ready for publication.

I would like to acknowledge my thesis committee: Charlie, Steve, Michael Schmidt, Peter Parker, and Dimitri Kusnezov, who very willingly read my thesis, despite the short notice, and made many useful comments, which, combined with the interesting questions they posed during my defense, have made this dissertation more complete. I would like to acknowledge my external reader, Rick Van Kooten, for devoting the time and effort to read this dissertation.

I had the incredible good fortune to have known Susie Engelman, Sara Batter and Jean Belfonti who all helped me in countless ways in dealing with the administrative tasks at Yale while being genuinely interested in my welfare.

I would like to thank my colleagues on the fifth floor for their many and varied contributions: Elliott Wolin for getting me started in GEM, for his refreshing approach, and for his friendship; Basem Barakat for our matinal physics discussions; Peter Martin for his miracles; Carole Devore for her knitting tips; and Will Emmett,

Jeff Snyder, Ram Ben-David, Ming Liu, Jeff Turk, Ken Barish and Lawrence Ho for their camaraderie.

A special thanks to Brenda Kuhn. Her patience, good humor and dedication can fell any nature of administrative beast! Pam and I also have her to thank for introducing us to country line dancing and Pennsylvania Dutch cuisine.

My work at SLAC has been enhanced by the contributions of many people, among them Homer Neal and Mike Hildreth, who were always willing to set aside time to help out with things I was working on; Ken Baird for his solidarity on the Endcap CRID; Dick Plano and his wife for their hospitality; the B lifetime group (Stéphane, Tracy Usher, Greg Punkar, Roberto Massetti, Nety Krishna and Tom Markiewicz) and many others in the B physics group who have helped to beat the analysis into its eventual fine shape; Dave Jackson for our talks on CP violation; Adrian McKemey for all his help and his friendship. Thanks!

I remember my times with Moshe and Helen Gai very fondly, and would also like to thank the other folks I worked with at WNSL: Steve Rugari and Zhiping Zhao, as well as Joe Cimino and the others in the shop.

My time in California was made memorable by my 'family' in Palo Alto: Soo, Jerry, Chris and Carl, who adopted me as their own and made me feel immediately at home.

I am most fortunate in having had the encouragement of Anna Shapiro, whose curiosity about the world has been an inspiration and a model of the scientific spirit. I am also grateful to all my family in India for their interest, despite the distance.

I can't begin to thank my wife Pam, who, through her love, humor and companionship, has provided me with the endless encouragement necessary to complete a project of this magnitude.

This thesis would not have been possible without my parents, Gina and Surojit Sen. I want to thank them for their love and belief in me, and for the freedom and encouragement to pursue my interests.

I dedicate this thesis to the memory of my father.

Contents

List of Tables

List of Figures

Chapter 1

Introduction

This thesis presents a measurement of the average B hadron lifetime τ_B using data collected at the Z^0 resonance with the SLD detector during the 1993 run at the Stanford Linear Collider (SLC). Approximately 50000 Z^0 decays were recorded from which a sample of 4299 $Z^0 \to b\bar{b}$ events was extracted. This measurement uses a topological technique to select a sample of vertices that is sensitive to τ_B and extracts the lifetime from a fit to the vertex position. The measurement takes advantage of the excellent vertex resolution, and the small and stable interaction point to resolve secondary vertices with high efficiency. The analysis is inclusive and has a low statistical error even with the modest size of the event sample used. The result is limited by the systematic error and is competitive with other recent measurements.

This chapter prevents an overview of the Standard Model and the physics that is being explored at SLD. The physics of B hadrons is discussed with a summary of recent and prospective measurements. The various techniques of measuring the average lifetime and individual lifetimes of B hadrons are also discussed.

1.1 The Standard Model

Throughout history physicists have tried to find organizing principles to unify the diverse phenomena of nature. In modern times, physicists have been able to explain the interactions of matter in terms of fewer and fewer forces, leading to the four basic

Interaction	Range (m)	Typical Coupling	Field Quanta		Typical Lifetime (s)
Gravity	∞	10^{-38}	graviton	$m = 0$	–
Electromagnetic	10^{-2}	∞	photon	$m_\gamma = 0$	10^{-20}
Weak	10^{-18}	10^{-6}	$W^\pm$	$m_W = 80$ GeV/c^2	10^{-8}
			Z^0	$m_Z = 92$ GeV/c^2	
Strong	$\leq 10^{-15}$	1	gluon	$m_g = 0$	10^{-23}

Table 1: Properties of the fundamental forces

interactions shown in Table 1, two of which are unified at the energy scale of current experiments. At the turn of the century Maxwell formulated electromagnetism, a unified theory of electricity and magnetism. During the first half of the twentieth century the development of relativity and quantum mechanics led to quantum electrodynamics (QED), a quantum field theoretic description of electromagnetism. More recently, Glashow, Salam and Weinberg postulated a common origin to the weak interaction and electromagnetism. The discovery of point structure inside hadrons led to the quark model and the concept of color, which allowed the strong interaction to be described in the theory of quantum chromodynamics (QCD) as a force between color charges mediated by gluons. Together, the electroweak theory and QCD make up the Standard Model of elementary particles, which has been very successful in describing existing phenomena and predicting new ones. There are unresolved theoretical questions in the Standard model, such as the origin of mass and the need to experimentally determine the coupling constants, which extensions to the Standard Model attempt to explain.

1.1.1 QED

For a field theory to be renormalizable it must be gauge invariant. Gauge invariant theories work by imposing a local invariance on the free-particle lagrangian describing a system. To preserve this invariance a new field must be introduced and the lagrangian must have additional terms that couple the new field to the original fields, i.e. the new field interacts with the original ones. A simple example of a gauge theory

is electromagnetism (QED).

A gauge-invariant description of the electromagnetic interaction comes from imposing a local U(1) invariance (invariance under 1-d rotations) on the free-particle lagrangian.

$$\mathcal{L}_{\text{free}} = i\bar{\psi}\gamma^{\mu}\partial_{\mu}\psi - m\bar{\psi}\psi \tag{1}$$

$$\psi \rightarrow \psi' = e^{ie\alpha(x)}\psi(x) \tag{2}$$

$$\begin{aligned} \mathcal{L}_{\text{free}} \rightarrow \mathcal{L}'_{\text{free}} &= ie^{-i\alpha(x)}\bar{\psi}\gamma^{\mu}\left(e^{i\alpha(x)}\partial_{\mu}\psi - ie^{i\alpha(x)}\psi\partial_{\mu}\alpha\right) - m\bar{\psi}\psi \\ &\neq \mathcal{L}_{\text{free}} \end{aligned} \tag{3}$$

The $\partial_{\mu}\alpha$ terms are not invariant under this transformation. They can be replaced with a 'covariant' derivative, D_{μ}, which is designed to be gauge invariant:

$$D_{\mu}\psi \rightarrow (D_{\mu}\psi)' = e^{ie\alpha(x)}D_{\mu}\psi \tag{4}$$

This is done by introducing a new vector field, the gauge field $A_{\mu}(x)$, and defining the covariant derivative as

$$D_{\mu}\psi(x) \equiv (\partial_{\mu} - iqA_{\mu}(x))\,\psi(x) \tag{5}$$

Then the gauge field transforms as

$$A_{\mu} \rightarrow A'_{\mu} = A_{\mu} + \partial_{\mu}\alpha \tag{6}$$

in order to satisfy equation (4). A mass term for the gauge field is not allowed, as this would be of the form $m^2 A_{\mu}A^{\mu}$, which is not gauge invariant. Thus,

$$\mathcal{L} = \bar{\psi}\,(iD_{\mu}\gamma^{\mu} - m)\,\psi \tag{7}$$

The lagrangian includes the following interaction term, which shows the link between the gauge field A_{μ} and the fermion field ψ, and has a coupling strength q.

$$\mathcal{L}_{\text{int}} = -qA_{\mu}\bar{\psi}\gamma^{\mu}\psi \tag{8}$$

Comparing this to $-J^\mu A_\mu$ from the classical electromagnetic lagrangian $\mathcal{L} = -\frac{1}{4}F_{\mu\nu}F^{\mu\nu} - J^\mu A_\mu$, we can equate A_μ with the photon field ($(\phi, \vec{A})$ classically). For a full electromagnetic lagrangian, we must also include the kinetic term (involving derivatives of the gauge fields), which is fully covariant and gauge invariant.

$$\begin{aligned} \mathcal{L}_{\text{QED}} &= \mathcal{L}_\psi + \mathcal{L}_{\text{int}} + \mathcal{L}_A & (9) \\ &= \bar{\psi}\left(i\gamma^\mu\partial_\mu - m\right)\psi + e\bar{\psi}\gamma^\mu A_\mu\psi - \frac{1}{4}F_{\mu\nu}F^{\mu\nu} & (10) \end{aligned}$$

where

$$F_{\mu\nu} = \partial_\mu A_\nu - \partial_\nu A_\mu \tag{11}$$

The equations of motion obtained from this lagrangian can be solved to an arbitrary level of precision using perturbation theory to a given order in q.

1.1.2 Non-Abelian Gauge Theories

The gauge group of QED is U(1), which is Abelian, i.e., successive transformations commute. Most groups are non-Abelian, including SU(2) and SU(3), the groups used to describe the weak and strong interactions. The different properties of Abelian and non-Abelian groups lead to important differences in the properties of the interactions they describe. The non-commutativity of non-Abelian gauge transformations requires an extra term to be added to the transformation of the gauge fields G^a_μ (cf. equation (6)) to make them gauge invariant.

$$G^a_\mu \to G^a_\mu - \frac{1}{g}\partial_\mu\alpha_a - f_{abc}\alpha_b G^c_\mu \tag{12}$$

The lagrangian thus acquires terms describing interactions between the gauge fields. Consequently, the behavior of the couplings as a function of q^2 will be different from the Abelian case, giving rise to asymptotic freedom and quark confinement in QCD (and to a lesser extent in SU(2)). Asymptotic freedom is the phenomenon where the coupling becomes small at short distances, or high $|q|^2$. Because of this, partons can be treated as free particles. Confinement refers to the way the coupling gets stronger at large distances, i.e. at small $|q|^2$, thus explaining why free quarks are not observed.

1.1.3 The Electroweak Interaction

The weak interaction is responsible for beta decay in nuclei and other long-lived decays such as $\pi^- \to \mu^- \bar{\nu}_\mu$. Its most basic feature is parity non-conservation, which implies that the left and right helicity components of the fermion field have different 'weak' charges. The lepton and quark charged currents were postulated to be a combination of vector minus axial vector currents: (V-A). Thus, considering only electrons and neutrinos, we have

$$J_\mu^+ = \frac{1}{2}\bar{e}\gamma_\mu\left(1-\gamma^5\right)\nu_e = \bar{e}_{_L}\gamma_\mu\nu_{e_L} \tag{13}$$

$$J_\mu^- = \frac{1}{2}\bar{\nu}_e\gamma_\mu\left(1-\gamma^5\right)e = \bar{\nu}_{e_L}\gamma_\mu e_{_L} \tag{14}$$

where

$$\psi_{\substack{L\\R}} = \frac{1}{2}\left(1\mp\gamma^5\right)\psi \tag{15}$$

This can be expressed more compactly by combining the leptons into a doublet

$$\chi_{_L} = \begin{pmatrix} \nu_e \\ e \end{pmatrix}_{_L} \tag{16}$$

and using linear combinations of the Pauli spin matrices τ^i $(i = 1,2,3)$ to express the weak charged current as

$$\begin{aligned} J_\mu^+ &= \bar{\chi}_{_L}\gamma_\mu\tau^+\chi_{_L} \\ J_\mu^- &= \bar{\chi}_{_L}\gamma_\mu\tau^-\chi_{_L} \end{aligned} \tag{17}$$

where $\tau^\pm = \frac{1}{2}\left(\tau^1 \pm i\tau^2\right)$. The structure of the weak currents supports the assumption that the currents are described by SU(2). The third generator of the group, τ^3, has a corresponding weak isospin current J_μ^3

$$\begin{aligned} J_\mu^3 &= \frac{1}{2}\bar{\chi}_{_L}\gamma_\mu\tau^3\chi_{_L} \\ &= \frac{1}{2}\left(\bar{\nu}_{e_L}\gamma_\mu\nu_{e_L} - \bar{e}_{_L}\gamma_\mu e_{_L}\right) \end{aligned} \tag{18}$$

Right-handed neutrinos are assumed not to exist in the Standard Model, which is consistent with the observation of only massless left-handed neutrinos. Thus, the right-handed electron $e_{_R}$ can be treated as an SU(2) singlet.

From equation (8), the electromagnetic current $J_\mu^{\rm em}$ is $-\bar{e}_{_L}\gamma_\mu e_{_L} - \bar{e}_{_R}\gamma_\mu e_{_R}$. Thus, the three weak isospin currents are not sufficient to include $J_\mu^{\rm em}$ and at least one more group generator is required. By analogy with strong isospin, one can postulate a weak hypercharge Y in terms of electric charge and weak isospin

$$Y = Q - T^3 \tag{19}$$

The corresponding weak hypercharge current is defined as

$$J_\mu^Y = J_\mu^{\rm em} - J_\mu^3 = -\frac{1}{2}\bar{\chi}_{_L}\gamma_\mu\chi_{_L} - \bar{e}_{_R}\gamma_\mu e_{_R} \tag{20}$$

Thus the left-handed doublet has $Y = -\frac{1}{2}$ and the right-handed singlet has $Y = -1$. A gauge invariant lagrangian can now be constructed using the following covariant derivative

$$D_\mu = \partial_\mu + \frac{i}{2}g\vec{\tau}\cdot\vec{W}_\mu + ig'YB_\mu \tag{21}$$

In this lagrangian, weak hypercharge is coupled to a U(1) gauge field B_μ with strength g' and weak isospin is coupled to the SU(2) gauge fields $W_\mu^i (i = 1, 2, 3)$ with coupling g.

$$\mathcal{L}_{\rm EW} = \mathcal{L}_{\rm fermion} + \mathcal{L}_{\rm gauge} \tag{22}$$

$$\mathcal{L}_{\rm gauge} = -\frac{1}{4}\vec{W}_{\mu\nu}\cdot\vec{W}^{\mu\nu} - \frac{1}{4}B_{\mu\nu}B^{\mu\nu} \tag{23}$$

where

$$B_{\mu\nu} = \partial_\mu B_\nu - \partial_\nu B_\mu \tag{24}$$

$$W_{\mu\nu}^i = \partial_\mu W_\nu^i - \partial_\mu W_\nu^i - g\epsilon_{ijk}W_\mu^j W_\nu^k \tag{25}$$

The last term of equation (25) is the gauge boson self-interaction term found in non-Abelian groups. The covariant derivative introduces the interaction between the fermions and gauge bosons.

$$\mathcal{L} = \bar{\chi}_{_L}\gamma^\mu\left(i\partial_\mu - g\frac{1}{2}\vec{\tau}\cdot\vec{W}_\mu + g'\frac{1}{2}B_\mu\right)\chi_{_L} + \bar{\psi}_{_R}\gamma^\mu\left(i\partial_\mu + g'B_\mu\right)\psi_{_R} \tag{26}$$

From this, the charged current terms can be extracted

$$\mathcal{L}_{\rm int}^{\rm CC} = -\frac{g}{2\sqrt{2}}\left(J_\mu^+ W^{+\mu} + J_\mu^- W^{-\mu}\right) \tag{27}$$

where

$$W_\mu^\pm = \frac{1}{\sqrt{2}}\left(W_\mu^1 \mp i W_\mu^2\right) \tag{28}$$

The remaining part of the lagrangian describes neutral currents

$$\mathcal{L}_{\text{int}}^{\text{NC}} = g J_\mu^3 W^{3\mu} + g' J_\mu^Y B^\mu \tag{29}$$

and must include the interaction term of $\mathcal{L}_{\text{QED}}$, i.e. a term coupling A_μ to J_μ^{em} with strength e. The following orthogonal linear combinations of $W^{3\mu}$ and B^μ provide the physical states A_μ and Z_μ

$$B_\mu = \cos\theta_W A_\mu - \sin\theta_W Z_\mu \tag{30}$$

$$W_\mu^3 = \sin\theta_W A_\mu + \cos\theta_W Z_\mu \tag{31}$$

Consistency with QED requires

$$e = g\sin\theta_W = g'\cos\theta_W \tag{32}$$

The neutral current part of the lagrangian is

$$\mathcal{L}_{\text{int}}^{\text{NC}} = -e J_\mu^{\text{em}} A^\mu + \frac{g}{\cos\theta_W}\left(J_\mu^3 - \sin^2\theta_W J_\mu^{\text{em}}\right) Z^\mu \tag{33}$$

The weak mixing (or Weinberg) angle θ_W parameterizes the embedding of $\mathrm{U}(1)_{\text{em}}$ in $\mathrm{SU}(2)_L \times \mathrm{U}(1)_Y$. Thus, the weak interaction and QED have been unified by having one coupling describing the strength of both interactions. The lagrangian also describes a second neutral current Z_μ. Weak neutral currents were first observed in 1974, validating the predictions of the theory.

The electroweak interaction can be generalized to the other lepton generations and quarks. To apply it to quarks, the quark charge Qe should be used in place of $-e$ yielding $J_\mu^{\text{em}} = \bar{\psi}\gamma Q\psi$.

Expanding the Z_μ term in equation (33) gives

$$\frac{g}{\cos\theta_W}\left(J_\mu^3 - \sin^2\theta_W J_\mu^{\text{em}}\right) Z^\mu = \frac{g}{\cos\theta_W}\bar{\psi}_f\gamma_\mu\left[\frac{1}{2}\left(1-\gamma^5\right)T^3 - Q\sin^2\theta_W\right]\psi_f Z^\mu \tag{34}$$

Using this, the vector and axial couplings of fermions to the Z^0 can be extracted.

$$v = T^3 - 2Q\sin^2\theta_W \tag{35}$$

$$a = T^3 \tag{36}$$

fermion	v	a	g_L	g_R
ν_e, ν_μ, ν_τ	$+\frac{1}{2}$	$+\frac{1}{2}$	0	$+1$
e, μ, τ	$-\frac{1}{2} + 2\sin^2\theta_W$	$-\frac{1}{2}$	$+2\sin^2\theta_W$	$-1 + 2\sin^2\theta_W$
u, c, t	$+\frac{1}{2} - \frac{4}{3}\sin^2\theta_W$	$+\frac{1}{2}$	$-\frac{4}{3}\sin^2\theta_W$	$+1 - \frac{4}{3}\sin^2\theta_W$
d, s, b	$-\frac{1}{2} + \frac{2}{3}\sin^2\theta_W$	$-\frac{1}{2}$	$+\frac{2}{3}\sin^2\theta_W$	$-1 + \frac{2}{3}\sin^2\theta_W$

Table 2: The fermion couplings to the Z^0

Another useful parameterization is in terms of the couplings to left- and right-handed fermions.

$$g_L = v - a \tag{37}$$

$$g_R = v + a \tag{38}$$

Table 2 shows the values of these couplings.

1.1.4 The Higgs Mechanism

Gauge invariant theories do not allow the gauge bosons to have non-zero masses because this breaks the invariance of the lagrangian. This contradicts what is experimentally observed, especially in the case of the weak interaction, which has extremely heavy gauge bosons ($M_Z = 91.187$ GeV/c^2 and $M_W = 80.22$ GeV/c^2). This apparent paradox is resolved by spontaneous symmetry breaking (SSB) in which the symmetry displayed by the system as a whole is not displayed by the ground state; it is spontaneously broken. This is done by introducing a field ϕ and a lagrangian for the field $\mathcal{L}_\phi$ that are invariant under the original symmetry of the system. $\mathcal{L}_\phi$ has the form

$$\mathcal{L}_\phi = \partial_\mu \phi^\dagger \partial^\mu \phi - V(\phi) \tag{39}$$

The symmetry is broken by the choosing an appropriate potential $V(\phi)$ such that the vacuum expectation value of the field ϕ_0 is non-zero.

In the case of the electroweak lagrangian, the specific way in which the symmetry is broken is called the Higgs mechanism. The SU(2)×U(1) symmetry of the electroweak

lagrangian must be broken in such a way that the W and Z bosons acquire mass while the photon remains massless. In other words, the Higgs mechanism preserves a $\mathrm{U}(1)_{\mathrm{em}}$ invariance in order to match experimental fact. This is achieved by introducing the Higgs field as a weak isospin doublet of complex scalar fields with hypercharge $Y = \frac{1}{2}$.

$$\phi = \begin{pmatrix} \phi^+ \\ \phi^0 \end{pmatrix} \tag{40}$$

With these isospin and hypercharge assignments ϕ^+ is positively charged and ϕ^0 is neutral. The symmetry-breaking Higgs potential is

$$V(\phi) = \mu^2 \phi^\dagger(x)\phi(x) + \lambda \left[\phi^\dagger(x)\phi(x)\right]^2 \tag{41}$$

For renormalizability, $\lambda > 0$, and for a non-zero vacuum expectation value, $\mu^2 < 0$. The potential has a minimum at

$$|\phi|^2 = -\frac{\mu^2}{2\lambda} = \frac{v^2}{2} \tag{42}$$

There is still a choice of the orientation of the ground state $\langle\phi\rangle_0$ in 2-d isospin space, i.e. a choice of how to break the symmetry. This choice is made so that only the neutral component of the Higgs field has a non-zero vacuum expectation value

$$\langle\phi\rangle_0 = \begin{pmatrix} 0 \\ v/\sqrt{2} \end{pmatrix} \tag{43}$$

Thus, the vacuum remains invariant under U(1) transformations of the Higgs field and charge conservation is not affected, as shown below.

$$Q\phi_0 = \left(T^3 + Y\right)\phi_0 = 0 \tag{44}$$

$$\phi_0 \to \phi_0' = e^{i\alpha(x)Q}\phi_0 = \phi_0 \tag{45}$$

$\phi(x)$ is coupled to the gauge fields via the usual covariant derivative

$$\mathcal{L}_{\mathrm{Higgs}} = \left(D_\mu\phi\right)^\dagger \left(D^\mu\phi\right) - V(\phi) \tag{46}$$

Substituting for $\phi(x)$ in the lagrangian gives the following mass terms

$$\mathcal{L}_{\mathrm{mass}} = \left(\frac{1}{2}vg\right)^2 W_\mu^+ W^{-\mu} + \frac{1}{2}\begin{pmatrix} A_\mu & Z_\mu \end{pmatrix}\begin{pmatrix} 0 & 0 \\ 0 & \frac{1}{4}(g+g')^2v^2 \end{pmatrix}\begin{pmatrix} A^\mu \\ Z^\mu \end{pmatrix}_L \tag{47}$$

which gives the following masses:

$$M_{W^\pm} = \frac{1}{2}gv \tag{48}$$

$$M_Z = \frac{1}{2}\sqrt{g^2 + g'^2}v \tag{49}$$

$$M_\gamma = 0 \tag{50}$$

The masses of the weak bosons are related by the weak mixing angle:

$$\cos\theta_W = \frac{M_{W^\pm}}{M_Z} \tag{51}$$

Fermions acquire mass from their SU(2) invariant couplings with the Higgs field

$$\mathcal{L}_{\text{ferm}} = -g_e(\bar{\chi}_L \phi e_R + \phi^\dagger \bar{e}_R \chi_L) \tag{52}$$

where g_e is an arbitrary constant that is determined by experiment. Using the vacuum expectation value gives the following for electrons:

$$\mathcal{L}_{\text{ferm}} = \frac{g_e v}{\sqrt{2}}(\bar{e}_L e_R + \bar{e}_R e_L) \tag{53}$$

$$m_e = \frac{g_e v}{\sqrt{2}} = \sqrt{2}\frac{g_e}{g}M_W \tag{54}$$

$$m_\nu = 0 \tag{55}$$

With the gauge choice made in breaking the symmetry of the vacuum, the four components of the Higgs field are reduced to one real field. In effect, the other three fields have become the longitudinal polarization states of the three massive gauge bosons. The physics of the remaining Higgs boson can be examined by treating it as an expansion around the vacuum

$$\phi(x) = \begin{pmatrix} 0 \\ \frac{v+H(x)}{\sqrt{2}} \end{pmatrix} \tag{56}$$

This gives rise to a mass term in the lagrangian with mass

$$M_H = \frac{\mu}{\sqrt{2}} \tag{57}$$

which is arbitrary and needs to be determined experimentally.

There is no direct experimental evidence for the existence of the Higgs boson. Direct observation of the Higgs boson is expected at higher energies, such as those at LHC. Several modifications to the basic Higgs mechanism have been postulated and further experiments are necessary to test their validity.

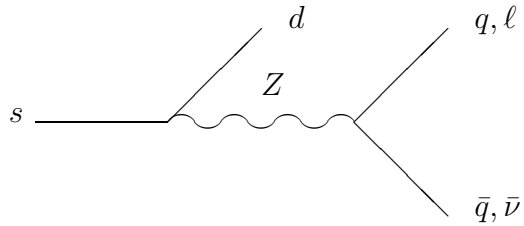

Figure 1: Flavor-changing neutral currents

1.1.5 The CKM Matrix

The electroweak interaction as described above does not allow flavor changing transitions between quark (or lepton) generations, e.g. $s \to d$, as shown in Figure 1. In other words, the lighter quark in each generation would have to be stable. Since this is not the case experimentally, one can hypothesize that the quark eigenstates of the electroweak hamiltonian are not the same as the eigenstates of the mass hamiltonian. For simplicity, if we look at the first two generations of quarks, we have

$$\begin{pmatrix} d' \\ u' \end{pmatrix}_L = \begin{pmatrix} \cos\theta_c & \sin\theta_c \\ -\sin\theta_c & \cos\theta_c \end{pmatrix} \begin{pmatrix} d \\ s \end{pmatrix}_L \tag{58}$$

where the q' are the weak eigenstates and the q are the mass eigenstates. Adapting the weak charged current we have

$$J^{\mu}_{wk} = \begin{pmatrix} \bar{u} & \bar{c} \end{pmatrix} \gamma^{\mu} \left(1 - \gamma^5\right) \begin{pmatrix} d' \\ s' \end{pmatrix} \tag{59}$$

All the flavor-changing transitions that are observed between the first two quark generations ($u \to d, c \to s, s \to u, c \to d$) are allowed by this mechanism, but with different vertex factors. For three quark generations, this is generalized to a 3×3 unitary matrix (the CKM matrix). This can be reduced to a canonical form with three angles and one phase parameterizing all quark mixing. The phase allows for the existence of CP violation in the Standard Model.

$$\begin{pmatrix} d' \\ s' \\ b' \end{pmatrix} = V_{\substack{\text{CKM} \\ 3\times 3}} \begin{pmatrix} d \\ s \\ b \end{pmatrix} \quad \text{or} \quad D'_i = V_{ij} D_j \tag{60}$$

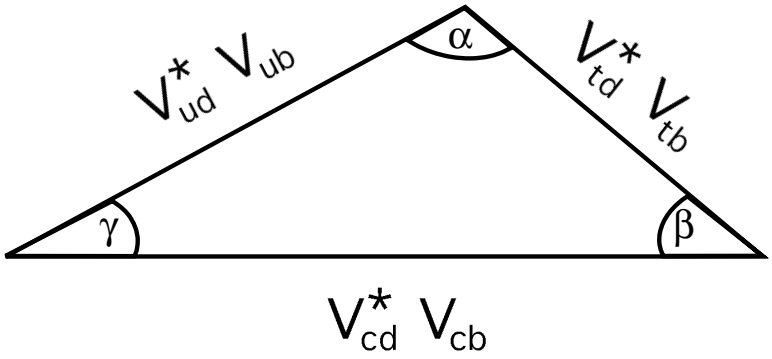

Figure 2: The unitarity triangle

The matrix is unitary in order to satisfy conservation of probability and suppress flavor-changing neutral currents (FCNCs). The weak neutral current can be written as

$$J^3_\mu = \frac{1}{2}\left(\bar{U}_{iL}\gamma_\mu U_{iL} - D_{iL}\gamma_\mu D_{iL}\right) \tag{61}$$

The FCNC terms cancel one another; this mechanism (the GIM mechanism) was invoked to explain the absence of FCNCs for u, d, and s quarks by postulating the existence of a fourth quark c.

Because the CKM matrix is nearly diagonal the following approximation can be used:

$$V_{\text{CKM}} = \begin{pmatrix} 1 & \theta & \theta^3 r e^{-i\delta} \\ -\theta & 1 & \theta^2 \\ \theta^3(1 - r e^{i\delta}) & -\theta^2 & 1 \end{pmatrix} \begin{pmatrix} d \\ s \\ b \end{pmatrix} \tag{62}$$

The following relation holds

$$\sum_k V_{k\mu} V^*_{k\nu} = \delta_{\mu\nu} \tag{63}$$

In discussing B physics and CP violation, the following special case is useful

$$V_{tb}V^*_{td} + V_{cb}V^*_{cd} + V_{ub}V^*_{ud} = 0 \tag{64}$$

$$V^*_{td} - \theta^3 + V_{ub} \approx 0 \tag{65}$$

This can be represented in the complex plane by the unitarity triangle (see Figure 2). The size of the CP-violating phase is related to the non-zero area of the triangle.

Experimental measurements of the CKM elements are attempting to overconstrain the unitarity triangle and ultimately see whether CP violation is fully described by the Standard Model.

1.2 Production and Decay of the Z^0 Boson

The differential cross-section for $e^+e^- \to \bar{f}f$ at $s \sim M_Z^2$ in the center-of-mass frame is given by

$$\frac{d\sigma}{d\Omega} = \frac{1}{64\pi^2 s}\frac{p_f}{p_i}\left|\mathcal{M}_Z\right|^2 \tag{66}$$

where p_f and p_i are the momenta of the initial and final states. The matrix element $\mathcal{M}_Z$ is given by

$$\mathcal{M}_Z = -\frac{g^2}{4\cos^2\theta_W}\left[\bar{f}\gamma^\nu\left(v_f - a_f\gamma^5\right)f\right]\left(\frac{g_{\nu\sigma} - k_\nu k_\sigma/M_Z^2}{k^2 - M_Z^2}\right)\left[\bar{e}\gamma^\sigma\left(v_e - a_e\gamma^5\right)e\right] \tag{67}$$

Evaluating this for the case of longitudinally polarized electrons with polarization $\mathcal{P}$ and ignoring fermion masses gives the following [1]

$$\begin{aligned}\frac{d\sigma}{d\cos\theta} &\propto \left(\frac{v_e^2 + a_e^2}{\sin^2\theta_W}\right)\left(\frac{v_f^2 + a_f^2}{\sin^2\theta_W}\right) \\ &\times \left\{(1 + \mathcal{P}A_e)(1 + \cos^2\theta) - 2A_f(\mathcal{P} + A_e)\cos\theta\right\}\end{aligned} \tag{68}$$

where θ is the angle of the fermion momentum with respect to the electron momentum and

$$A_f = \frac{2v_f a_f}{v_f^2 + a_f^2} \tag{69}$$

The total cross-section for $e^+e- \to \gamma/Z^0 \to f\bar{f}$ ($f \neq$ electron) follows the Breit-Wigner form [1]

$$\sigma_Z^{f\bar{f}}(s) = \left(\frac{12\pi}{M_Z^2}\right)\frac{s\Gamma_{ee}\Gamma_{ff}}{\left(s - M_Z^2\right)^2 + s^2\Gamma_Z^2/M_Z^2} \tag{70}$$

where

$$\Gamma_{ff} = \frac{G_F M_Z^3}{3\sqrt{2}\pi}N_c\left(a_f^2 + v_f^2\right) = \frac{G_F M_Z^3}{6\sqrt{2}\pi}N_c\left(\left(g_L^f\right)^2 + \left(g_R^f\right)^2\right) \tag{71}$$

and N_c is the color factor (3 for quarks, 1 for leptons). Initial state radiation has been neglected, which will shift the peak upwards and cause substantial Z^0 production

above the pole. The t-channel component can be neglected except at small angles ($\theta \sim 0$), where it is predominantly a QED effect useful for measuring luminosity at e^+e^- colliders.

The left- and right-handed electron contributions can be separated to give the following polarized cross-sections:

$$\sigma_L \equiv \sigma\left(e^-_L e^+_R \to Z \to f\bar{f}\right) = \sqrt{2}G_F M_Z \frac{s\Gamma_{f\bar{f}}}{\left(s - M_Z^2\right)^2 + s^2\Gamma_Z^2/M_Z^2} \left|g_L^e\right|^2 \tag{72}$$

$$\sigma_R \equiv \sigma\left(e^-_R e^+_L \to Z \to f\bar{f}\right) = \sqrt{2}G_F M_Z \frac{s\Gamma_{f\bar{f}}}{\left(s - M_Z^2\right)^2 + s^2\Gamma_Z^2/M_Z^2} \left|g_R^e\right|^2 \tag{73}$$

These polarized cross-sections are useful for investigating electroweak physics at the Z^0 resonance.

1.3 Cross-section Asymmetries at the Z^0 Resonance

By measuring asymmetries of the cross-section, one can isolate various couplings to the Z^0 boson. A polarized beam can both enhance some of these asymmetries and allow new ones to be measured. Thus SLC is a powerful tool for measuring the Z^0 couplings and testing the Standard Model. A brief description of the asymmetries measured at SLD is given below.

1.3.1 The Left-Right Asymmetry, A_{LR}

The left-right asymmetry of the $e^+e^- \to Z^0$ cross-section is a measure of the difference in the cross-section for right-handed electrons and left-handed electrons

$$A_{LR} = \frac{\sigma_L - \sigma_R}{\sigma_L + \sigma_R} \tag{74}$$

$$= \frac{2v_e a_e}{v_e^2 + a_e^2} \tag{75}$$

$$= A_e \tag{76}$$

A_{LR} is very sensitive to the value of $\sin^2\theta_W$ and currently provides the most precise measurement of it ($\sin^2\theta_W = 0.2292 \pm 0.0009(\text{stat}) \pm 0.0004(\text{syst})$) [2]. It is insensitive

to the final states, allowing all Z^0 decays to be used. The experimentally measured quantity is $A_{LR}^{\rm exp}$

$$A_{LR}^{\rm exp} = \frac{N_L - N_R}{N_L + N_R} \tag{77}$$

$$= P_- A_{LR} \tag{78}$$

which is enhanced by the high electron beam polarization available at SLD.

1.3.2 The Forward-Backward Asymmetry, A_{FB}^f

The forward-backward asymmetry A_{FB}^f measures a combination of the initial and final state couplings to the Z^0. The identity of the final state is necessary for this measurement.

$$A_{FB}^f = \frac{\sigma_F^f - \sigma_B^f}{\sigma_F^f + \sigma_B^f} \tag{79}$$

where

$$\begin{aligned} \sigma_F^f &\equiv \int_0^1 \frac{d\sigma}{d\cos\theta} d\cos\theta \\ \sigma_B^f &\equiv \int_{-1}^0 \frac{d\sigma}{d\cos\theta} d\cos\theta \end{aligned} \tag{80}$$

$$A_{FB}^f = \frac{3}{4}\left[\frac{(g_L^e)^2 - (g_R^e)^2}{(g_L^e)^2 + (g_R^e)^2}\right]\left[\frac{\left(g_L^f\right)^2 - \left(g_R^f\right)^2}{\left(g_L^f\right)^2 + \left(g_R^f\right)^2}\right] \tag{81}$$

$$= \frac{3}{4} A_e A_f \tag{82}$$

At SLD, this asymmetry is not important because individual measurements of A_e and A_f can be made using the asymmetries A_{LR} and $A_{LR}^{FB,f}$ which are also enhanced by the electron beam polarization.

1.3.3 The Polarized Forward-Backward Asymmetry, $A_{LR}^{FB,f}$

The polarized forward-backward asymmetry $A_{LR}^{FB,f}$ measures the final state couplings to the Z^0. It requires a knowledge of the polarization of the initial state and the

identity of the final state.

$$A_{FB}^{LR,f} = \frac{\left(\sigma_F^f - \sigma_B^f\right)_L - \left(\sigma_F^f - \sigma_B^f\right)_R}{\left(\sigma_F^f - \sigma_B^f\right)_L + \left(\sigma_F^f - \sigma_B^f\right)_R} \quad (83)$$

$$= \frac{3}{4}\left[\frac{\left(g_L^f\right)^2 - \left(g_R^f\right)^2}{\left(g_L^f\right)^2 + \left(g_R^f\right)^2}\right] \quad (84)$$

$$= \frac{3}{4}A_f \quad (85)$$

The experimentally measured quantity is $\frac{3}{4}P_- A_f$ and is thus enhanced by the high polarization at SLC/SLD.

Table 3 summarizes the results from measurements of asymmetries at SLD [2, 3, 4].

Asymmetry	Value
A_{LR}	0.1628 ± 0.0071
$A_{FB}^{LR,b}$	$A_b = 0.87 \pm 0.11 \pm 0.09$

Table 3: Summary of recent asymmetry measurements at SLD

1.4 The Physics of B Hadrons

The study of the b quark, its couplings, and the decays of its bound states is an active area of research today because B hadrons can be produced with the energies accessible by many current experiments. Many different topics can be explored through the study of B hadron decays. The electroweak couplings of the b quark to the Z^0 can be measured with both the unpolarized and polarized forward-backward asymmetry, as described earlier. Like the K^0 system, neutral B mesons (B_s and B_d) exhibit mixing between their mass eigenstates. CP violation is expected to occur in B hadron decays according to Standard Model predictions and can be investigated through asymmetries in B^0 and $\bar{B}^0$ decays. B hadrons have long lifetimes ($\tau \sim 1$ ps) because their decays are Cabibbo suppressed due to the larger mass of the top quark. Measurement of the average B hadron lifetime and the individual B hadron

lifetimes provides information about the decay mechanism and the level at which it can be approximated by the decay of a b quark. The identification of rare decay modes, e.g. penguin decays, provides further information about the B decay mechanism. The CKM matrix elements V_{cb} and V_{ub} can be measured in several ways using B hadron decays, and V_{td} can be measured from B_d mixing. These provide a limit on the expected level of CP violation that can be expected in B decays; discrepancies can point to the need for extensions to the Standard Model.

Currently B physics is being investigated in three different environments, each with their own advantages. CLEO and ARGUS operate at the $\Upsilon(4s)$ resonance ($E_{CM} \sim 11$ GeV), which is a $b\bar{b}$ bound state. This is just above threshold for the production of B_d and B_u mesons which are produced in large numbers because of the high luminosities of these experiments. Thus, these experiments are best suited to high statistics measurements of branching ratios and the identification of rare decay modes, while they lack the resolution for lifetime measurements that is available at higher energies because the B mesons are produced essentially at rest. LEP and SLD operate at the Z^0 resonance ($E_{CM} \sim 91$ GeV) where B hadrons, including the B_s meson and B baryons, are produced from the decay $Z^0 \to b\bar{b}$. Smaller numbers of B hadrons are produced compared to CLEO because of the much lower luminosity, even though the cross-section for $b\bar{b}$ production is higher (6.3 nb compared to 1.2 nb). However, because of the much higher energy B hadrons, are boosted ($\beta\gamma \sim 7$) and travel ~ 3 mm before decaying, which allows one to identify B decay vertices more easily and measure their decay lengths with greater precision. The large mass difference between the b quark and lighter quarks means that the decay products of a B meson should have high p_T which can be used to separate charm hadron decays from B decays. SLD is especially well-suited to B physics measurements because of the excellent vertex resolution due to the small beampipe and precision CCD vertex detector. Particle identification is also available (though not used in this thesis) to remove backgrounds. The polarization of the electron beam at SLD allows the direct measurement of the couplings of the b quark to the Z^0 to be made using the left-right forward-backward asymmetry. B physics is also pursued at the Tevatron at FNAL (in particular the CDF experiment) where $b\bar{b}$ pairs are produced in $p\bar{p}$ collisions.

Measurements at the Tevatron extract samples of B hadron decays from a very large QCD background by reconstructing exclusive decay modes with a corresponding hit in efficiency. However, because of the extremely high $p\bar{p}$ cross-section, sufficiently large samples of events can be collected. At the Tevatron, B hadrons are boosted which allows lifetimes and time-dependent measurements to be made with reasonable accuracy.

1.4.1 Models of B Hadron Decays

The measurement of lifetimes and branching ratios sheds light on the mechanism of B hadron decay. In turn, further improvement of these models makes their predictions more accurate which has a direct bearing on the precision of measurements that are heavily model-dependent. Several models of the underlying mechanism of B hadron decay exist. The major difficulty in modeling these decays is in relating the theoretically well-understood quark decays to the decays of experimentally observed objects: hadrons. The spectator or free-quark model [5, 6] examines inclusive heavy hadron decay solely in terms of the heavy quark (Q) in the hadron ($Q\bar{q}$ or Qqq), and the lighter quarks (q) are assumed to have no role in the decay (see Figure 3). Thus, the decays $b \to q\bar{l}\nu_l$ and $b \to qq'\bar{q}'$ fully describe B hadron decay in the spectator model. B hadron decays, in particular, are modeled better than the decays of lighter hadrons because non-spectator decays are much smaller. Figure 4 shows the two types of non-spectator decays: W-exchange, which is purely hadronic, and annihilation which can be either leptonic or hadronic. Both of these processes are helicity disfavored unless they are accompanied by virtual gluon emission, and their decay rates scale as m_Q^2. The spectator decay rate scales as m_Q^5 and will therefore be much more dominant for B decays than for charm decays [7, 8, 9]. Nevertheless, some rare decay modes do take place via non-spectator decays because the spectator decays are suppressed or not possible. The description of semileptonic decays matches experiment most closely because fewer non-spectator modes are available, and as there are fewer quarks in the decay, the modeling of the hadronization is less crucial to a description of the physics than in a hadronic decay.

The width for semileptonic B decays in the spectator model is just the decay

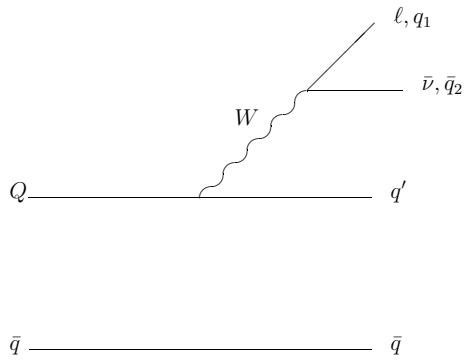

Figure 3: Spectator diagram for B hadron decay

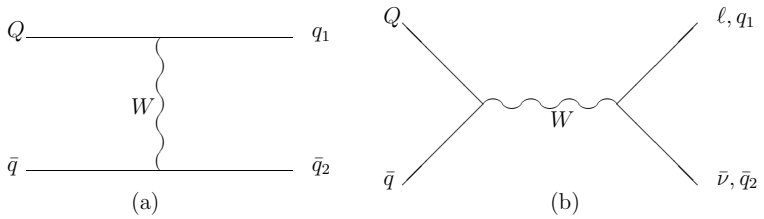

Figure 4: Non-spectator diagrams for B hadron decay

width for $b \to q\bar{l}\nu_l$, which to a first approximation is the analog of the width for the decay $\mu^- \to e^-\nu_\mu\bar{\nu}_e$:

$$\Gamma\left(b \to q\bar{l}\nu_l\right) = \frac{G_F^2 m_b^5}{192\pi^3}\left|V_{qb}\right|^2. \tag{86}$$

Corrections can be made to the naive spectator model to account for massive final state particles [10] and the radiation of soft gluons [11, 12]. The semileptonic width is then modified with the phase-space factor Φ

$$\begin{aligned}\Phi\left(x_1, x_2, x_3\right) &= 12\int_{(x_1+x_2)^2}^{(1-x_3)^2} \frac{ds}{s}\left(s - x_1^2 - x_2^2\right)\left(1 + x_3^2 - s\right) \\ &\quad \times \left\{\left[s - \left(x_1 - x_2\right)^2\right]\left[s - \left(x_1 + x_2\right)^2\right]\right. \\ &\quad \left. \times \left[\left(1 + x_3\right)^2 - s\right]\left[\left(1 - x_3\right)^2 - s\right]\right\}^{\frac{1}{2}}\end{aligned} \tag{87}$$

where $x_1 = \frac{m_q}{m_b}$, $x_2 = \frac{m_l}{m_b}$, and $x_3 = \frac{m_\nu}{m_b}$. The masses of the final state leptons can be neglected to give

$$\Phi\left(x, 0, 0\right) = 1 - 8x^2 + 8x^6 - x^8 - 24x^4\ln x \tag{88}$$

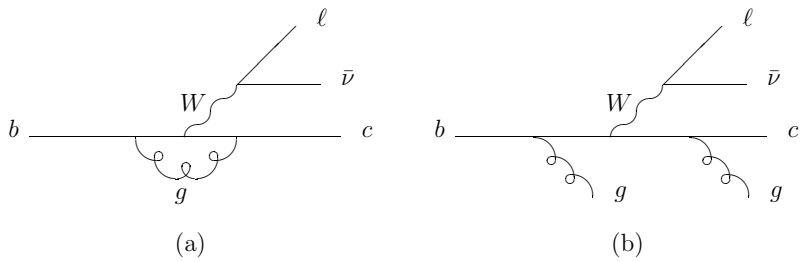

Figure 5: Radiative gluon corrections in semileptonic b decays

Assuming $m_b \sim 5$ GeV/c^2, $\Phi = 0.44$ and 0.21 for $b \to c\bar{l}\nu_l$ and $b \to u\bar{l}\nu_l$, respectively. To lowest order in $\mathcal{O}(\alpha_s)$ the correction for gluon radiation in Figure 5 gives

$$\Gamma_{\rm sl} = \Gamma^0_{\rm sl}\left(1 - \frac{2}{3}\frac{\alpha_s(m_b)}{\pi} g\left(\frac{m_q}{m_b}\right)\right) \tag{89}$$

where

$$\begin{aligned} g(\epsilon) &= \left(\pi^2 - \frac{31}{4}\right)\left(1-\epsilon^2\right) + \frac{3}{2} \\ &= 2.44 \quad \text{for} \quad \epsilon_c = 1.65/4.95 \\ &= 3.45 \quad \text{for} \quad \epsilon_u = 0.20/4.95 \text{ for } \alpha_s = 0.20 \end{aligned} \tag{90}$$

This provides a correction of -10% and -14% for $b \to c$ and $b \to u$, respectively.

Measurements at ARGUS [13] and CLEO [14] of the prompt electron spectrum from B hadron decays show that $|V_{ub}|^2 / |V_{cb}|^2 \sim 0.01$. Thus, the expression for the total decay width can be simplified by ignoring $b \to u$ transitions

$$\Gamma^{\rm total}_{\rm sl} = \frac{G_F^2 m_b^5}{192\pi^3}|V_{cb}|^2 \Phi\left(\frac{m_b}{m_c}, 0, 0\right)\left(1 - \frac{2}{3}\frac{\alpha_s(m_b)}{\pi} g\left(\frac{m_q}{m_b}\right)\right) \tag{91}$$

Hadronic decays of B hadrons ($b \to cq_2\bar{q}_3$) can also be described by the spectator model if the massive final state and hard gluon effects are accounted for. The full expression for the phase-space factor Φ in equation (87) must be used, which will suppress massive final states, e.g. $b \to cs\bar{c}$. The decay width must also now include the factor $|V_{q_2q_3}|$. In the dominant spectator decay of Figure 6(a), the quark pair from the virtual W^- forms one of the final state hadrons and the c quark forms the other hadron with the spectator antiquark $\bar{q}$. Hard gluon exchange between initial and final quark lines creates an additional process (color-suppressed decay) as in

Figure 6(b) in which the quark pair from the virtual W^- may no longer be in a color singlet [9]. Therefore the quark pairings into hadrons are now different and the expression for the spectator hadronic decay width must now include contributions from both processes and the interference between them. The strengths of the color-favored (normal spectator) and color-suppressed contributions can be calculated in QCD with the leading-log approximation [15] evaluated at the mass scale $\mu \sim m_b^2$.

$$c_\pm(\mu) = \left(\frac{\alpha_s\left(M_W^2\right)}{\alpha_s\left(\mu\right)}\right)^{\frac{-6\gamma_\pm}{\left(33-2n_f\right)}} \tag{92}$$

where $\gamma_- = -2\gamma_+ = 2$ and n_f is the number of active flavors, which is 5 in this case. At the B mass scale, $c_+ \approx 0.85$ and $c_- \approx 1.4$. The amplitudes for the color-favored and color-suppressed decays are $\frac{1}{2}(c_+ + c_-)$ and $\frac{1}{2}(c_+ - c_-)$, respectively and the hadronic decay width is now proportional to

$$\Gamma_{\rm had} \propto \left[\frac{3}{4}\left(c_+ + c_-\right)^2 + \frac{3}{4}\left(c_+ - c_-\right)^2 + \frac{1}{2}\xi\left(c_+ + c_-\right)\left(c_+ - c_-\right)\right]\Gamma_{\rm sl} \tag{93}$$

$$\propto \left[\frac{3}{2}\left(c_+^2 + c_-^2\right) + \frac{1}{2}\xi\left(c_+^2 - c_-^2\right)\right]\Gamma_{\rm sl}, \tag{94}$$

where ξ is a color matching factor that is model dependent and varies between 0 and $\frac{1}{3}$. The hadronic decay modes are enhanced by $\sim 13\%$, which reduces the semileptonic branching ratio to $\sim 12 - 14\%$ from the naive expectation of $\frac{1}{11}$.

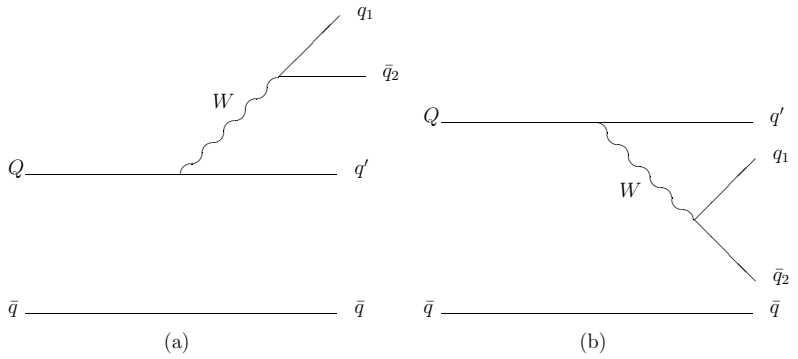

Figure 6: (a) Color favored and (b) color suppressed decays

A major feature of the expressions for the decay width in the spectator model (see equations (86) and (91)) is the large sensitivity to m_b, which is not well-defined.

Models of the decay of the B hadron attempt to remove this dependence by relating m_b to tunable parameters that can be determined from experiment. The ACM model [16] describes semileptonic decays inclusively in terms of a modified spectator model. The effect of the spectator and non-spectator quark being in a bound state is simulated by assigning a Fermi motion to the quarks inside the B hadron and assessing the "off-shellness" or mass-defect W^2 of the b quark inside the B hadron. The spectator quark is assigned a mass $m_{\rm sp}$ and its momentum is given a gaussian spread of p_F. The heavy quark is treated as virtual particle:

$$W^2 = m_b^2 = m_B^2 + m_{\rm sp}^2 - 2m_B\sqrt{p^2 + m_{\rm sp}^2}. \tag{95}$$

where m_B is the B hadron mass. The momentum spectrum $d\Gamma_{\rm sl}/dx$ from the decay of a quark of invariant mass W is folded with the momentum spectrum $\Phi(p)$ of the spectator quark to give the total theoretical lepton spectrum that can then be tuned to experimental data.

$$\frac{d\Gamma_{\rm sl}}{dx} = \int_0^{p_{\rm max}} \Phi(p)p^2 dp \frac{d\Gamma_b(W,p)}{dx} \tag{96}$$

The dependence on m_b has been removed in favor of three parameters that can be tuned to experimental results: $p_F, \epsilon_c = m_c/m_b$ and $m_{\rm sp}$. The main dependence is on p_F, which fixes the average value of m_b.

Other models of semileptonic decay such as WSB [17] and ISGW [18] use detailed models of the initial and final state hadronic wave functions which requires choosing a particular parameterization of the QCD potential. A discrete set of final state particles, e.g. D, D^* and D^{**}, is considered. Only decays to single mesons are considered, which is considered to be good approximation for $b \to c$ transitions [19]. All possible decay modes to the discrete set of final states are summed over to provide an inclusive spectrum that can be fitted to experimental results. The exclusive decay models all start by defining form factors as q^2 dependent functions that are adjusted to data. The various models use different assumptions in defining these functions and normalize them differently. The form of the meson wave functions is also model dependent. The WSB model uses monopole form factors normalized at $q^2 = 0$. The wave functions are obtained using a relativistic harmonic oscillator potential. The

semileptonic decay width obtained is about 20% lower than from the ACM model which may be due to the limited number of final states summed over [20, 17]. The ISGW model uses exponential form factors normalized at maximum q^2, when $p_D = 0$. The wave functions are extracted from a Coulomb plus linear QCD potential and all final states are summed over for their $1S$, $2S$ and $1P$ states. The motivation behind the ISGW calculations is to model the endpoint of the lepton spectrum and thus reliably calculate $|V_{ub}/V_{cb}|$. The inclusive semileptonic width matches the ACM model very closely [20].

Exclusive two-body hadronic decays can also be modeled by assuming that factorization is valid, i.e. the matrix element is expressed as a product of two hadronic currents. This is thought to be a good approximation because the large energy release in B decay suggests that the two color singlets should be traveling apart fast enough to not influence each other. In color-suppressed and penguin decays, this may not hold, but they are not the dominant decay mechanisms and should have little influence on calculations. At present, experimental data suggests that factorization can be a working model of B decay [7, 19]. The BSW model [21] uses a phenomenological approach: an effective charged current and an effective neutral current are defined with strengths a_1 and a_2, respectively. The two coefficients are related to the color-suppressed and color-favored amplitudes and the color-matching factor ξ in equation (94). These are determined from a fit to a subset of experimental data from charm decay and extrapolated to $\alpha_s(m_b)$. There is a good match to data [21, 7], i.e. the modified spectator model is the dominant mechanism for energetic 2-body decays of B mesons. The value of $\xi \sim 0$ which suggests that quarks from different color singlet currents do not readily combine to form mesons.

A recent development in the theory of B decays is Heavy Quark Effective Theory (HQET) [22, 7, 23, 19, 4]. In the limit of infinitely heavy quark mass, the heavy quarks become irrelevant to the non-perturbative dynamics of the light quarks. Thus, the heavy quark degrees of freedom can be treated separately from those of the light quarks, and all the form factors can be related to one universal function: the Isgur-Wise function ξ. Corrections due to the finite masses of the b and c quarks and for gluon exchange need to be made. Thus, the form factors can be determined in a

model-independent way. Calculations of branching ratios based on HQET appear to be consistent with data [7, 24].

1.4.2 Electroweak Asymmetries in B decays

As described in section 1.3, the forward-backward and the left-right forward-backward asymmetries for b quarks can be measured at SLD. Both quantities measure the axial and vector couplings of the b quark to the Z^0. The latter asymmetry makes use of polarized electron beam at SLC, and is large and independent of the couplings of the Z^0 to the electron. The current SLD result for $A_{LR}^{FB,b}$ is [3] expressed as A_b is

$$A_b = 0.87 \pm 0.11(\text{stat}) \pm 0.09(\text{syst}) \tag{97}$$

1.4.3 Measurement of CKM Matrix Elements

The magnitudes of the CKM matrix elements V_{ub} and V_{cb} can be extracted from measurements of semileptonic B decays. Semileptonic decays are used because they can be modeled more accurately. The value of $|V_{cb}|$ is gradually becoming known more accurately but our knowledge of $|V_{ub}|$ is still dominated by theoretical uncertainties.

$|V_{cb}|$ can be calculated using the inclusive semileptonic branching ratio BR_{sl} and the B meson lifetime.

$$|V_{cb}| = \sqrt{\frac{\text{BR}_{\text{sl}}}{\gamma_c \tau_B}} \tag{98}$$

The constant γ_c is model-dependent and is the main source of uncertainty in such a measurement. CLEO II [25] has measured it to be

$$|V_{cb}| = 0.041 \pm 0.001(\text{expt}) \pm 0.003(\text{theory}) \tag{99}$$

$|V_{cb}|$ can also be measured using exclusive semileptonic decays by fitting to the lepton momentum spectrum. The results are obviously sensitive to the model used. CLEO II has measured $|V_{cb}|$ using the decay $B \to D^* \ell^- \bar{\nu}$ and the result is consistent with the inclusive result.

$|V_{ub}|$ is hard to determine accurately because it is so small. The ratio $|V_{ub}|/|V_{cb}|$ can be measured by examining the inclusive lepton spectrum beyond the kinematic

endpoint for $b \to c$ decays. Because the u quark is lighter, this region of the spectrum should only be populated by $b \to u$ decays. However, the result is very sensitive to the modeling of the endpoint of the spectrum and has a large range. At CLEO II [26] $|V_{ub}|/|V_{cb}|$ varies from 0.076 – 0.101. Thus, $|V_{ub}|$ appears to be non-zero, which is necessary for CP violation to occur within the Standard Model framework.

1.4.4 B-$\bar{B}$ Mixing

The two neutral B meson systems, B_d and B_s are known to mix [27], i.e. the eigenstates of mass and the weak interaction are not the same. The description of B mixing is similar to that of K mixing, involving the box diagrams shown in Figure 7. The

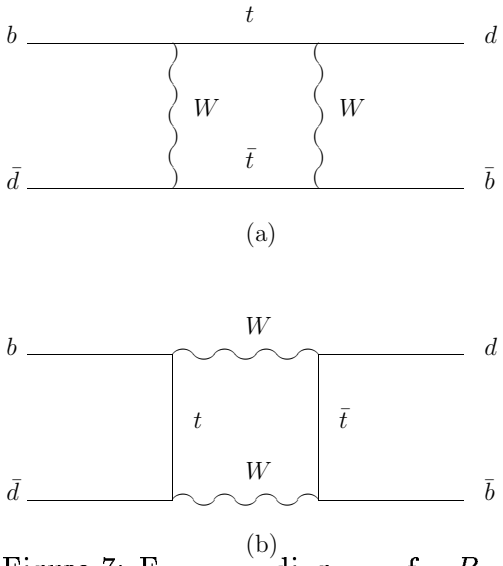

Figure 7: Feynman diagrams for B mixing

mixing is expected to be dominated by the t quark contribution [28]:

$$\left(\frac{\Delta m}{\Gamma}\right)_{B_d} \sim \tau_{B_d} |V_{tb}|^2 |V_{td}|^2 m_t^2 \tag{100}$$

$$\left(\frac{\Delta m}{\Gamma}\right)_{B_s} \sim \tau_{B_s} |V_{tb}|^2 |V_{ts}|^2 m_t^2 \tag{101}$$

The mixing parameter X is defined as

$$X = \frac{\text{Mixed}}{\text{Mixed} + \text{Unmixed}} \tag{102}$$

$$= \frac{(\Delta m/\Gamma)^2 + \left(\frac{1}{2}\Delta\Gamma/\Gamma\right)^2}{2 + 2(\Delta m/\Gamma)^2} \quad (103)$$

$$\approx \frac{1}{2}\frac{(\Delta m/\Gamma)^2}{(1 + (\Delta m/\Gamma)^2)} \quad (104)$$

Here one assumes that $\Delta\Gamma/\Gamma$ is small because, unlike the K system, decay rates are not limited by phase space due to the much higher B meson mass. Time-independent measurements indicate that the mixing parameter X is ~ 0.7 for B_d and approaches its asymptotic value of $\frac{1}{2}$ for B_s [27]. Further understanding of mixing, especially in the B_s system, requires measuring the time evolution of the mixing from which $\Delta m/\Gamma$ can be directly measured.

Semileptonic decays of B and $\bar{B}$ mesons ($B \to D\ell^+\nu$) will produce leptons of opposite sign. Thus, in the absence of mixing, leptons of opposite sign are produced from the decay of a $B\bar{B}$ pair. Mixing can be measured by counting events with leptons of the same sign. The signal is diluted by semileptonic decays of the charm meson produced in the B decay, which produce leptons of opposite sign. This background can be removed by applying a cut on the transverse momentum of the lepton. The time dependence of the mixing can be measured by counting the number of positively and negatively charged leptons as a function of the proper decay time of the B meson. A disadvantage of this method is that high p_T leptons are required in both event hemispheres, so a very small fraction of events are tagged. The method does not remove charged B mesons which dilute the mixing signal. At SLD an alternate method can be employed that takes advantage of the polarized electron beam and the excellent vertex resolution available. The forward-backward asymmetry for $Z^0 \to b\bar{b}$, which is large for the polarization available at SLD, can be used to tag the flavor of the B mesons when they are produced. Thus, only one B meson decay per event needs to be found and a flavor assigned to it by finding the charge of the lepton from the decay. In this way, the large cut in efficiency that occurs by requiring two high p_T leptons is avoided. The forward-backward asymmetry can be defined as

$$A_{FB}^b = \frac{(B^0 \text{ in } e^- \text{ direction}) - (\bar{B}^0 \text{ in } e^- \text{ direction})}{(B^0 \text{ in } e^- \text{ direction}) + (\bar{B}^0 \text{ in } e^- \text{ direction})} \quad (105)$$

The asymmetry will be diluted by mixing compared to its value for $B^\pm$ decays. The

time dependence of the mixing can be explored by expressing the asymmetry as a function of the proper time of the B decay.

1.4.5 CP Violation in B Decays

By inspection of the unitarity triangle that is most relevant to B decay (see section 1.1.5, Figure 2) it is apparent that the sides are all of similar length, i.e. the product $V_{\mu b}V_{\mu d}^*$ is of order θ^3 in each case. Thus, the angles of the unitarity triangle should be large and because these are directly related to the CP violating phase of the CKM matrix, CP violating effects should be large in B decays. CP violation in B decays can be understood by starting with the description of the time evolution of the eigenstates of the neutral B system. The weak eigenstates are analogous to the $K^0\bar{K}^0$ system:

$$|B_L(t)\rangle = p\,|B^0\rangle + q\left|\bar{B}^0\right\rangle = e^{-\Gamma_L t/2}e^{im_L t}\,|B_L(0)\rangle \tag{106}$$

$$|B_H(t)\rangle = p\,|B^0\rangle - q\left|\bar{B}^0\right\rangle = e^{-\Gamma_H t/2}e^{im_H t}\,|B_H(0)\rangle \tag{107}$$

Without CP violation $p = q$; because the violation is a small effect one can assume that $p \approx q$. For B decays, the mass splitting $\Delta m = m_H - m_L$ should be much larger than the splitting in decay widths $\Delta\Gamma$ because a lot of phase space is available and the different CP eigenstates typically differ by a pion mass. Thus, $\Gamma_H \approx \Gamma_L \equiv \Gamma$. The evolution of the strong eigenstates is [9, 29]

$$\left|B^0(t)\right\rangle = e^{-\Gamma t/2}\left[\cos\left(\frac{\Delta m t}{2}\right)\left|B^0(0)\right\rangle + \frac{iq}{p}\sin\left(\frac{\Delta m t}{2}\right)\left|\bar{B}^0(0)\right\rangle\right] \tag{108}$$

$$\left|\bar{B}^0(t)\right\rangle = e^{-\Gamma t/2}\left[\frac{ip}{q}\sin\left(\frac{\Delta m t}{2}\right)\left|B^0(0)\right\rangle + \cos\left(\frac{\Delta m t}{2}\right)\left|\bar{B}^0(0)\right\rangle\right] \tag{109}$$

If CP is conserved, the decay rate of $B \to f$ should be the same as for $\bar{B} \to \bar{f}$. Thus a difference in these decay rates can be used to define a CP-violating asymmetry:

$$A(t) = \frac{\Gamma\left[B^0(t) \to f\right] - \Gamma\left[\bar{B}^0(t) \to \bar{f}\right]}{\Gamma\left[B^0(t) \to f\right] + \Gamma\left[\bar{B}^0(t) \to \bar{f}\right]} \tag{110}$$

The decay rate $\Gamma[B(t) \to f] \propto |\langle f|B(t)\rangle|^2$. If f and $\bar{f}$ are CP eigenstates and can both be reached by B and $\bar{B}$ (through mixing) then the decay rate can be simplified

to

$$\Gamma[B(t) \to f] \propto e^{-\Gamma t} |\langle f|B\rangle|^2 \left[1 - Im\left(\frac{p}{q}\rho\right)\sin(\Delta m t)\right] \tag{111}$$

with a similar expression for $\bar{B} \to f$ but with a plus sign. The asymmetry is

$$A(t) = -Im\left(\frac{p}{q}\rho\right)\sin(\Delta m t) \tag{112}$$

Two sources contribute to the phase measured by the asymmetry: the mixing p/q and the decay amplitudes (ρ).

To evaluate the asymmetry for B decays, (p/q) and ρ must be assessed. The ratio (p/q) can be calculated from the matrix elements for the $B - \bar{B}$ mixing box diagrams

$$\left(\frac{p}{q}\right)_{B_d^0} = \frac{V_{tb}^* V_{td}}{V_{tb} V_{td}^*} = e^{2i\phi_{td}} \tag{113}$$

$$\left(\frac{p}{q}\right)_{B_s^0} = \frac{V_{tb}^* V_{ts}}{V_{tb} V_{ts}^*} = e^{2i\phi_{ts}} \sim 1 \tag{114}$$

and

$$\begin{aligned} \rho &= \frac{\left\langle f|\bar{B}\right\rangle}{\langle f|B\rangle} = \frac{V_{qb}^*}{V_{qb}} = e^{-2i\phi_{qb}} \\ &= 1 \qquad \text{for } b \to c \\ &= e^{-2i\phi_{ub}} \qquad \text{for } b \to u \end{aligned}$$

Thus, the CP-violating asymmetry is

$$A_{B_d}(t) = -\sin 2(\phi_{td} - \phi_{qb})\sin(\Delta m t) \tag{115}$$

$$A_{B_s}(t) = -\sin 2(\phi_{td} - \phi_{qb})\sin(\Delta m t) \tag{116}$$

The asymmetry can be measured in different B decays to constrain the angles of the unitarity triangle [9, 30, 31] (see Table 4), and thus verify whether CP violation is fully described by the Standard Model. One can also look for CP violation in same-sign dilepton production from semileptonic B^0 decays. In the presence of CP violation, the decay rates Γ_{++} and Γ_{--} for $B\bar{B} \to \ell^+\ell^+ X$ and $B\bar{B} \to \ell^-\ell^- X$, respectively will not be the same.

$$A(\ell\ell) = \frac{\Gamma_{++} - \Gamma_{--}}{\Gamma_{++} + \Gamma_{--}} = \frac{|p/q|^2 - |q/p|^2}{|p/q|^2 + |q/p|^2} \tag{117}$$

Quark process	B_d mode	$\phi_{td} - \phi_{qb}$
$b \to c\bar{c}s$	$J/\psi K_S^0$ $J/\psi K_L^0$ $J/\psi K^{0*}$	β
$b \to c\bar{c}d$	D^+D^- $D^{+*}D^{-*}$ $D^{\pm *}D^{\mp}$	β
$b \to u\bar{u}d, d\bar{d}d$	$\pi^+\pi^-$ $\rho^{\pm}\pi^{\mp}$ $a_1^{\pm}D^{\mp}$	α

Table 4: The angles of the unitarity triangle accessible with CP-violating asymmetry measurements

This is a much smaller asymmetry because it is not enhanced by the large CP violating phases.

CP-violation in B decays is now a very active area of research with the construction of several new experiments. Two B factories which will operate at the $\Upsilon(4s)$ resonance are being built at SLAC and KEK. These both will be high luminosity asymmetric colliders, i.e. the electron and positron beams will be of unequal energy, so that the B mesons produced in the decay of the $\Upsilon(4s)$ will be boosted and separated from each other. One meson will be used to tag the sign of the B quark and the other will be fully reconstructed and used to look for CP-violating effects. In addition, experiments at DESY, FNAL and CERN are expected to search for CP violation in B decays.

1.4.6 Penguin Decays

Flavor changing neutral currents (FCNCs) are suppressed to first order by the GIM mechanism. However decays of the form $b \to s\gamma$ are possible through a higher order process: penguin decays (see Figure 8). The ratio of the penguin decay width to a typical lower order decay width is [9]

$$\frac{\Gamma(b \to s\gamma)}{\Gamma(b \to c\bar{u}d)} \quad \propto \quad \frac{V_{tb}^2 V_{ts}^2 \left(\frac{m_t}{m_W}\right)^4}{V_{cb}^2 V_{ud}^2} \tag{118}$$

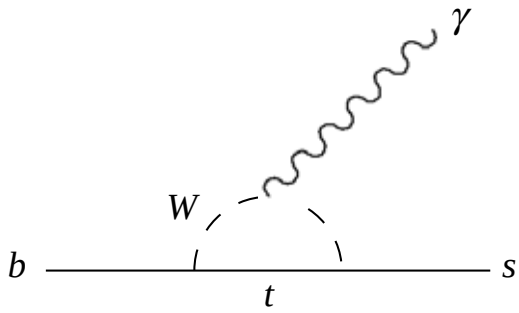

Figure 8: The electromagnetic penguin decay $b \to s\gamma$

$$\propto \left(\frac{m_t}{m_W}\right)^4 \tag{119}$$

Thus with the large top quark mass, this is not as rare as it might have been. A theoretical estimate [9] of the branching ratio of $b \to s\gamma$ is $\sim 2 \times 10^{-3}$. Recently, this has been measured at CLEO [45]: $\mathrm{BR}(b \to s\gamma) = (2.32 \pm 0.57 \pm 0.35) \times 10^{-4}$. The measurement consists of looking for γ candidates with energies that are consistent with coming from a penguin decay, i.e. in the range 2.2 to 2.7 GeV. The background from the continuum is reduced in one of two ways: by cuts on event shape, or by reconstructing the $B \to X_s\gamma$ decay, where X_s is either a kaon or pions. For the latter sample, the best B candidate is found after applying cuts on invariant mass and angle. The branching ratio is extracted from a background-subtracted E_γ spectrum by fitting to the Monte Carlo. The CLEO result is consistent with the Standard Model prediction.

1.4.7 Measurements of the Lifetimes of B Hadrons

Measuring the lifetimes of B hadrons as a whole and each species individually provides information that can be used to better model these decays. Knowledge of B hadron lifetimes is also useful for extracting results from other measurements. For example, CKM matrix elements can be extracted from branching ratio and mixing measurements but the value determined will depend in part on the value of τ_B that is used. Accurate measurements of the differences between the lifetimes of different B hadrons allows one to estimate the effect of non-spectator decays. This section reviews recent measurements of the average B hadron lifetime, including a preview

of the measurement presented in this thesis, and measurements of the lifetimes of individual B hadrons.

Measurements of the Average B Hadron Lifetime

The average B hadron lifetime is a somewhat artificial construct, as its value depends on the exact mix of B hadrons in the sample, which in turn depends on the center-of-mass energy of the experiment. However, as mentioned earlier, the differences in the lifetimes of the different B meson species are expected to be small because spectator decays are expected to predominate. As long as the composition of one's sample is known, measurements of the average B hadron lifetime can be compared and are a useful indication of the value of the individual B meson lifetimes. Although it has already been measured accurately several times, the average B hadron lifetime remains interesting because until recently the world average value had not stabilized, but was drifting upwards [32, 4]. The measurements of the average B hadron lifetime τ_B can be divided into two classes: those using all B decays and those using only semileptonic B decays. It is interesting to note that measurements using only semileptonic B decays tend to be lower than the other measurements, though this is not statistically significant, and further measurements using all B decays are of interest.

In order to measure the B hadron lifetime, a sample of B hadron decays needs to be selected from the data and the proper decay time of each B hadron needs to be measured. The large b quark mass gives rise to B meson decay products with high p_T, and consequently large impact parameters which can be used to select these decays. The proper decay time is measured from the displacement of the decay vertex from the primary vertex, and the boost of the B hadron. The various methods differ in how these two quantities are measured: some measure both quantities directly while others use quantities that are sensitive to the decay length but which are easier to measure, e.g. impact parameter. The boost can be measured directly or estimated to a greater or lesser degree using the Monte Carlo.

Many measurements of τ_B use only semileptonic B decays as they can be modeled more reliably than hadronic decays, and it can be easier (compared to hadronic B decays) to tag a pure sample of semileptonic B decays and locate the decay vertex by

looking for leptons characteristic of B decays. The leptons are used both for tagging a B decay and for calculating the lifetime. The method suffers from low statistics because of the semileptonic branching ratio and the lepton identification efficiency, as well as the event selection cut on the lepton transverse momentum. However, the LEP experiments with their large event samples are able to obtain small statistical errors. The basic procedure used by ALEPH [33] is to start with a sample of hadronic Z^0 decays and identify muon and electron candidates in them. The transverse momentum of the leptons is measured with respect to the jet axes in the event and is required to be > 2 GeV/c to remove lighter quark events giving a sample purity of 73%. The impact parameter, or distance of closest approach to the primary vertex, is measured for the selected leptons. The impact parameter is signed according to standard conventions. Without the effect of finite detector resolution the impact parameter should be positive for leptons from a B decay. The negative tail is a measure of the detector resolution and the uncertainty in measuring the B direction using jet axes, and is used in the construction of a likelihood function for the lifetime fit. The lifetime is extracted from a fit to the lepton impact parameter distribution. The likelihood function is a convolution of the resolution function and the impact parameter distributions for the signal and background. The impact parameter distributions and sample composition are obtained by performing the same analysis on Monte Carlo event samples. The impact parameter distributions for B decays and cascade c decays are parameterized as a function of τ_B.

$$\tau_B = 1.29 \pm 0.06(\text{stat}) \pm 0.10(\text{syst}) \text{ ps} \tag{120}$$

L3 [34] and OPAL [35] have measured τ_B using a similar method yielding

$$\tau_B = 1.535 \pm 0.035(\text{stat}) \pm 0.028(\text{syst}) \text{ ps} \tag{121}$$

$$\tau_B = 1.523 \pm 0.034(\text{stat}) \pm 0.038(\text{syst}) \text{ ps} \tag{122}$$

The dominant systematic errors come from the uncertainty in parameterizing the detector resolution and the heavy quark fragmentation.

For increased statistics some measurements of τ_B use hadronic B decays or all B decays. In a similar method to the previous one, DELPHI [36] uses the impact

parameter distribution for all of the tracks in a selected B decay to determine τ_B. Events are required to be in the acceptance of the vertex detector and signed impact parameters are calculated for tracks with $p > 3$ GeV/c and $p_T > 0.8$ GeV/c (with respect to the nearest jet axis). B decays are selected from a sample of hadronic Z^0 decays by selecting event hemispheres with ≥ 2 tracks with impact parameters δ in the range 0.1 mm $\leq |\delta| \leq$ 2.0 mm. This has an efficiency of 54.6% and a purity of 38.5%. The lifetime is measured using the impact parameter of tracks in the hemisphere opposite the tagged hemisphere. This reduces biases towards picking long-lived B decays. The likelihood function was constructed in a similar way to that used in the lepton method.

$$\tau_B = 1.542 \pm 0.021(\text{stat}) \pm 0.045(\text{syst}) \text{ ps} \tag{123}$$

The modeling of hadronic B decays is not as well understood as semileptonic decays which is reflected in the large systematic error. The dominant systematic errors come from uncertainties in the resolution function and the B decay multiplicity.

DELPHI [36] has measured τ_B using a method that reconstructs secondary vertices in B decays. Secondary vertex candidates are constructed from pairs of tracks that intersect or pass close to each other in a region away from the primary vertex. Tracks are removed from a vertex if they significantly worsen the quality of the vertex fit or if they fit better to the primary vertex. Candidate vertices are required to have at least three tracks. B hadron events are selected by cutting on the number of tracks (≥ 4), distance to the primary vertex (> 1 mm) and invariant mass (> 1.7 GeV/c^2) of the vertices in the event. The proper decay length is calculated using the vertex momentum and the lab decay length and vertices are required to have a proper decay length > 1.5 mm. The sample purity (of true B hadron decay vertices) is 93.5% with an efficiency of 7.87%. τ_B is determined from the proper decay length distribution using the closest vertex to the primary vertex in each hemisphere.

$$\tau_B = 1.599 \pm 0.014(\text{stat}) \pm 0.035(\text{syst}) \text{ ps} \tag{124}$$

The systematic error comes predominantly from uncertainties in modeling the detector.

An alternate approach that uses the full B decay sample measures the lifetime with a dipole length which is defined in various ways but in general measures the distance between B decay points in opposite hemispheres. In this way the uncertainty in reconstructing the primary vertex is minimized. ALEPH [37] uses the full hadronic Z^0 event sample with cuts on track quality but no enrichment with B decays. The dipole used is a weighted average of the track intersection points with the thrust axis projected onto the $r-\phi$ plane. The tracks are weighted by their rapidity, which enhances the contribution from B decays over fragmentation tracks, and by the position error of the intersection with the thrust axis. τ_B is determined from the average dipole length which is determined as a function of τ_B using the Monte Carlo.

$$\tau_B = 1.511 \pm 0.022(\text{stat}) \pm 0.078(\text{syst}) \text{ ps} \tag{125}$$

The systematic error for this measurement is very high because of the heavy dependence on the Monte Carlo to extract the calibration curve. The main error source is from uncertainty in the modeling of heavy quark fragmentation.

At CDF [38] τ_B has been measured using the decay chain

$$B \to J/\psi X \to \mu^+\mu^- X$$

Even though the product of the two branching ratios is very low ($\sim 8 \times 10^{-4}$), the high cross-section for B production compensates for this. Candidate $\mu^+\mu^-$ events are selected by constraining μ candidates to come from a single vertex. The sample is cleaned up by cuts on the invariant mass of the vertex and on the muon p_T. A two-dimensional decay length is constructed from the projection of the vector connecting the primary and J/ψ vertices onto the transverse momentum of the J/ψ. The boost of the B hadron is calculated using the boost of the J/ψ vertex with corrections from the Monte Carlo and the vertex is kept if the proper decay time is $> 220\mu$m. The lifetime is determined from a fit to the proper time distribution with the backgrounds estimated from the sidebands of the invariant mass distribution:

$$\tau_B = 1.46 \pm 0.06(\text{stat}) \pm 0.06(\text{syst}) \text{ ps} \tag{126}$$

The main source of systematic error is the uncertainty in the production and decay kinematics.

The method described in this thesis measures the average B hadron lifetime using an inclusive sample of B decays. The sample is selected using an impact parameter tag and vertices are constructed using selected tracks in each event hemisphere. Vertices that have the most sensitivity to τ_B are chosen, and a fit is made to the distribution of the distance between the B vertex and the primary vertex. The vertex construction and selection is very efficient so the result has a low statistical error given the size of the initial event sample. However, the measurement is sensitive to the Monte Carlo, in particular to the way the backgrounds and the B hadron boost are modeled. Chapters 5 and 6 will discuss this method in more detail.

The B^0 and B^+ Lifetimes

Measurements of the differences in the B^0 and B^+ lifetimes are important for understanding the decay mechanisms of B hadrons and estimating the role of non-spectator decay processes. Experiments at the $\Upsilon(4s)$ measure the ratio of the lifetimes and not their individual values because it is difficult to make direct measurements of B mesons that are nearly at rest. The lifetime ratio can be calculated from the decay widths of the B^0 and B^+:

$$\frac{\tau(B^+)}{\tau(B^0)} = \frac{\Gamma(B^0)}{\Gamma(B^+)} = \frac{\Gamma(B^0)}{\Gamma_{sl}}\frac{\Gamma_{sl}}{\Gamma(B^+)} \tag{127}$$

$$= \frac{\mathrm{BR}(B^+ \to X\ell^+\nu)}{\mathrm{BR}(B^0 \to X\ell^+\nu)} \tag{128}$$

where the semileptonic widths for B^0 and B^+ are assumed to be equal because the spectator model predominates. At CLEO [39] a large selection of B^+ and B^0 decay channels are examined and the fraction of B events with identified leptons gives the semileptonic branching ratios and the lifetime ratio:

$$\frac{\tau(B^+)}{\tau(B^0)} = 0.93 \pm 0.18(\mathrm{stat}) \pm 0.12(\mathrm{syst}) \tag{129}$$

Direct measurements of the B^0 and B^+ lifetimes have been made at both LEP [40] and CDF [41]. At DELPHI, the lifetimes are measured by constructing a sample of vertices from B^0 and B^+ decays. The charge of the vertex is used to distinguish the two hadrons and the *udsc* background is reduced using cuts on the invariant

mass and the angle between the vertex momentum and the line connecting the vertex to the primary vertex. The boost of the B hadron is estimated using the vertex momentum with corrections from the Monte Carlo to account for neutral particles. The decay length is estimated by calculating the difference between the decay length of the candidate B vertex and the minimum distance needed to resolve a secondary vertex. This excess decay length is found to remove the dependence on modeling the acceptance. The lifetime is extracted from separate fits to the excess proper times of each B candidate in the neutral and charged samples. The neutral sample is assumed to consist of B^0, B_s^0, and Λ_b and the fit uses the world average values of the lifetimes of the latter two hadrons. The resulting lifetimes are:

$$\tau(B^+) = 1.72 \pm 0.08(\text{stat}) \pm 0.06(\text{syst}) \text{ ps} \quad (130)$$

$$\tau(B^0) = 1.68 \pm 0.15(\text{stat})^{+0.13}_{-0.17}(\text{syst}) \text{ ps} \quad (131)$$

$$\frac{\tau(B^+)}{\tau(B^0)} = 1.02^{+0.13}_{-0.10}(\text{stat})^{+0.13}_{-0.10}(\text{syst}) \quad (132)$$

At OPAL and CDF, B meson decays have been fully reconstructed in a limited number of decay channels. OPAL uses semileptonic decays to D^-, $\bar{D}^0$, and D^{*-} to partially separate charged and neutral B mesons. The charm mesons are selected by combining kaon and pion tracks to form candidates that are then combined with leptons to form candidate B decay vertices. These vertices are subjected to cuts on fit quality, momentum, invariant mass and decay length to remove random backgrounds. The signal and background are estimated from the peak and sidebands of the charm meson invariant mass distributions. The different $\bar{D}^{(*)}\ell^+$ decay modes have differing fractions of B^0 and B^+ decays which need to be determined. This is done using measured semileptonic branching ratios and the Monte Carlo. The B meson energy is reconstructed using the Monte Carlo to correct the energy of the $\bar{D}^{(*)}\ell^+$ vertex for the missing neutrino. The lifetime is extracted from a fit to the proper decay time of the $\bar{D}^{(*)}\ell^+$ vertices.

$$\tau(B^+) = 1.52 \pm 0.14(\text{stat}) \pm 0.09(\text{syst}) \text{ ps} \quad (133)$$

$$\tau(B^0) = 1.53 \pm 0.12(\text{stat}) \pm 0.08(\text{syst}) \text{ ps} \quad (134)$$

$$\frac{\tau(B^+)}{\tau(B^0)} = 0.99 \pm 0.14(\text{stat})^{+0.05}_{-0.04}(\text{syst}) \quad (135)$$

The CDF measurement uses fully reconstructed B decays to $J/\psi K^{(*)}$ and $\psi(2s)K^{(*)}$. J/ψ candidates are identified by combining oppositely charge muons to give the correct invariant mass. $\psi(2s)$ candidates are found from the decay $\psi(2s) \to J/\psi\pi^+\pi^-$, K^0_S candidates are identified by finding track pairs with the correct invariant mass and K^* is identified by the decay $K^{*+} \to K^0_S\pi^+$. The B decay vertex is reconstructed using these tracks and the boost is estimated using the J/ψ momentum. The signal region is defined around the mass peak in the B invariant mass distribution and the background is determined from the sidebands. The lifetime is determined from a fit to the proper time of the B decay.

$$\tau(B^+) = 1.68 \pm 0.09(\text{stat}) \pm 0.06(\text{syst}) \text{ ps} \quad (136)$$

$$\tau(B^0) = 1.64 \pm 0.11(\text{stat}) \pm 0.06(\text{syst}) \text{ ps} \quad (137)$$

$$\frac{\tau(B^+)}{\tau(B^0)} = 1.02 \pm 0.09(\text{stat}) \pm 0.01(\text{syst}) \quad (138)$$

Measurement of the Average Lifetime of B Baryons

The average lifetime of baryons containing a b quark has been measured at OPAL [42] using semileptonic decays. Decay chains of the form

$$\Lambda_b^0 \to \Lambda_c^+ \ell^- \bar{\nu} X$$
$$\Lambda_c \to \Lambda X$$
$$\Lambda \to p\pi^-$$

are used. The short lifetime of charmed baryons ($\sim$ 0.2 ps) allows the position of the B baryon decay to be estimated from the intersection of the Λ and the lepton. Λ candidates from the decay are found by combining identified protons with other tracks to create a vertex far from the primary vertex. The Λ candidates are combined with identified leptons of the correct sign to find candidate B baryon decay vertices which are required to have high invariant masses. The $p\pi$ invariant mass is required to be close to the masses of charm baryons for the signal. The boost of the B baryon is estimated from the momentum of the $\Lambda\ell$ vertex using the Monte Carlo to correct it. The lifetime is extracted from a fit to the decay length distribution of the $\Lambda\ell$ vertex.

$$\tau(\Lambda_b) = 1.05^{+0.23}_{-0.20}(\text{stat}) \pm 0.08(\text{syst}) \text{ ps} \quad (139)$$

The major systematic error comes from the uncertainty in estimating the decay length using the $\Lambda\ell$ momentum vector.

Measurement of the B_s^0 Lifetime

The B_s^0 lifetime $\tau(B_s^0)$ has been measured at OPAL and CDF [43, 44]. Both the OPAL and CDF measurements use the semileptonic decay $B_s^0 \to D_s^- \ell^+ \nu(X)$ and reconstruct two decay channels of the D_s^-:

$$D_s^- \to \phi\pi^- \quad \text{where} \quad \phi \to K^+K^-$$
$$D_s^- \to K^{*0}K^- \quad \text{where} \quad K^{*0} \to K^+\pi^-$$

Thus the final states in both channels are the same: $K^+K^-\pi^-$. The OPAL measurement is described below, and the CDF measurement is similar. Candidate D_s^- vertices are constructed from track combinations within each jet and are required to have the correct charge. Particle identification is used to find tracks consistent with a $KK\pi$ combination. Random combinations of tracks are removed by cutting on the vertex momentum and angles between the tracks in the vertex and the D_s^- direction. Invariant mass cuts are applied to isolate the $K^{*0}K^-$ and $\phi\pi^-$ decay modes. The B_s^0 decay vertex is constructed by looking for combinations of the D_s^- candidates and a high momentum lepton ℓ^+. The random background is reduced by cutting on the opening angle between the lepton and the $KK\pi$ momentum vector and requiring a minimum total vertex momentum. The signal is isolated by requiring the invariant mass of the $KK\pi\ell$ combination to be close to the B_s mass. The B_s decay length is extracted from a fit to the primary vertex and B_s vertex positions and the $KK\pi\ell$ momentum vector, and the D_s decay length is measured as the distance between the B_s and D_s vertices. The boost and proper decay time of the B_s is calculated from the $D_s\ell$ invariant mass and energy using the Monte Carlo to estimate the missing energy from the neutrino and fragmentation. The B_s lifetime is extracted from a fit to the decay length distribution of the candidate B_s vertices:

$$\tau(B_s^0) = 1.54^{+0.25}_{-0.21}(\text{stat}) \pm 0.06(\text{syst}) \text{ ps} \tag{140}$$

The dominant systematic errors come from modeling the background and the boost. The result from the CDF measurement is

$$\tau(B_s^0) = 1.42^{+0.27}_{-0.23}(\text{stat}) \pm 0.11(\text{syst}) \text{ ps} \tag{141}$$

A second CDF measurement of $\tau(B_s^0)$ has been made using the decay chain

$$B_s^0 \to J/\psi\phi$$
$$J/\psi \to \mu^+\mu -$$
$$\phi \to K^+K^-$$

Candidate J/ψ vertices are constructed from oppositely charge muons by constraining the invariant mass to be close to the J/ψ mass. Candidate ϕ vertices are constructed from combinations of oppositely charged kaons by constraining the invariant mass to be close to the ϕ mass. The B_s decay vertex is constructed by extrapolating from the J/ψ and ϕ candidates and constraining the invariant mass to be close to the B meson mass. The proper decay length is calculated from the B_s momentum and vertex position, and the lifetime is extracted from a fit to the mass and proper decay length distributions. The result is

$$\tau(B_s^0) = 1.74^{+0.90}_{-0.60}(\text{stat}) \pm 0.07(\text{syst}) \text{ ps} \tag{142}$$

The dominant systematic error comes from modeling the background.

Summary

Table 5 and Figure 9 summarize the average B hadron lifetime results described above. The measurements of lifetime ratios and individual lifetimes are collected in Table 6.

Experiment	method	τ_B(ps)	stat. error (ps)	syst. error (ps)
ALEPH	lepton			
	impact parameter	1.529	0.06	0.10
L3	lepton			
	impact parameter	1.535	0.035	0.028
OPAL	lepton			
	impact parameter	1.523	0.034	0.038
DELPHI	hadronic			
	impact parameter	1.542	0.021	0.045
DELPHI	vertex	1.599	0.014	0.035
ALEPH	dipole length	1.511	0.022	0.078
CDF	J/ψ	1.46	0.06	0.06
SLD	vertex	1.564	0.030	0.036

Table 5: Summary of Average B Hadron Lifetime Results

Measurement	Experiment		stat. error	syst. error
τ_{B^+}/τ_{B^0}	CLEO	0.93	0.18	0.12
	DELPHI	1.02	$^{+0.13}_{-0.10}$	$^{+0.13}_{-0.10}$
	OPAL	0.99	0.14	$^{+0.05}_{-0.04}$
	CDF	1.02	0.09	0.01
τ_{Λ_b} (ps)	OPAL	1.05	$^{+0.23}_{-0.20}$	0.08
τ_{B_s} (ps)	OPAL	1.54	$^{+0.25}_{-0.21}$	0.06
	CDF semileptonic	1.42	$^{+0.27}_{-0.23}$	0.11
	CDF J/ψ	1.74	$^{+0.90}_{-0.60}$	0.07

Table 6: Summary of Exclusive B Lifetime Measurements

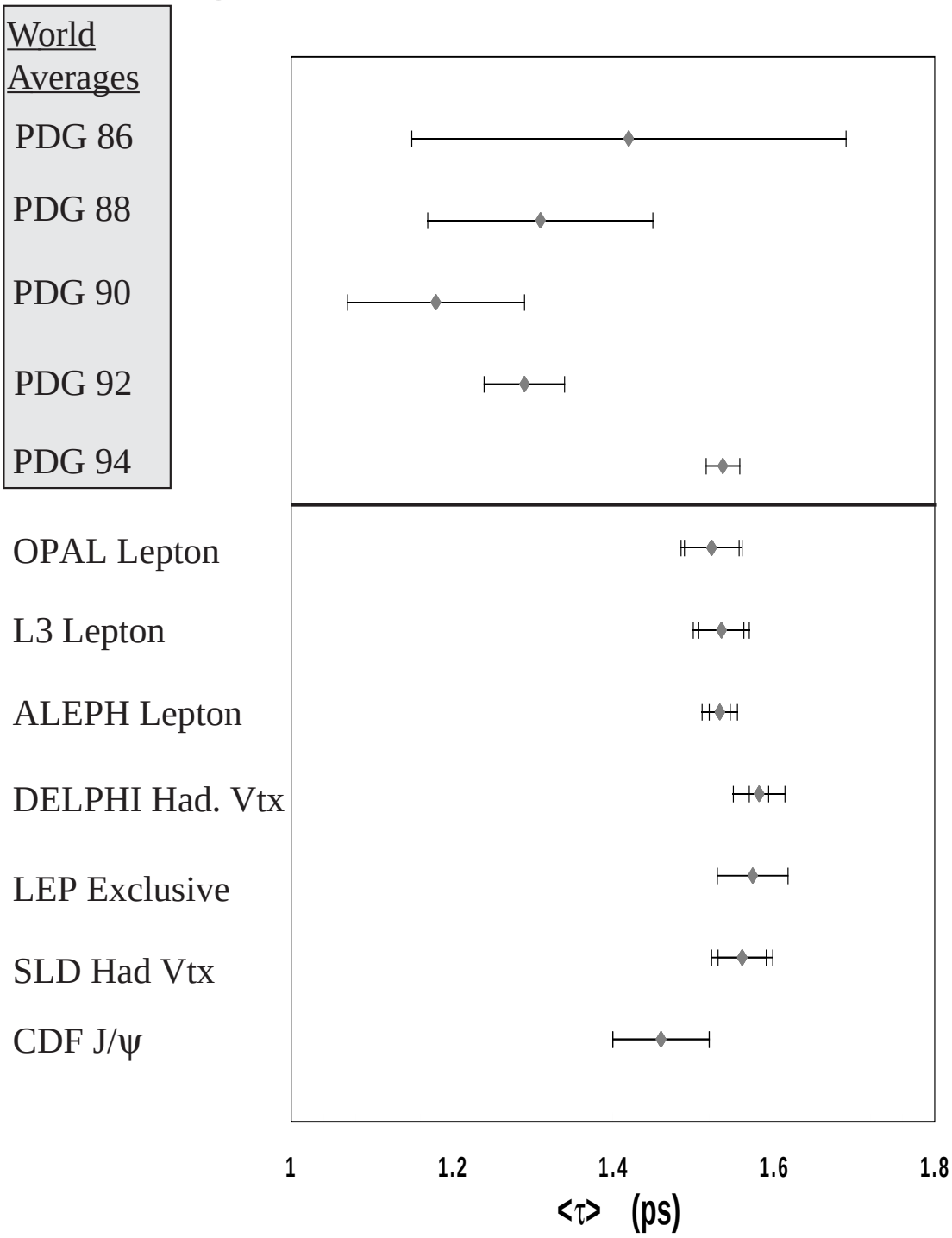

Figure 9: Recent Measurements of the Average B Hadron Lifetime

Chapter 2

The SLD Experiment

The SLD experiment operates at the Z^0 resonance and is unique in using polarized electrons in collision with unpolarized positrons. This chapter describes the production and transport of the polarized electron beam and the positron beam, and the detection of their collision by the SLD experiment.

2.1 SLC

The SLAC Linear Collider (SLC) [46] was designed to collide electrons and positrons at a center-of-mass energy of $\sim$ 92 GeV to produce Z^0 bosons at rest. Figure 10 shows the layout of the collider. The design of the SLC is a departure from the recirculating collider as exemplified by the Large Electron-Positron collider (LEP) at CERN. The SLC is a single-pass collider: its beams are brought into collision once and are then directed to beam dumps. The acceleration of the beams is provided by a single linear accelerator (linac). The electron and positron beams are then steered through separate arcs to the collision point. One motivation for this design was to develop a prototype for the next generation of colliders. It was also seen as a relatively inexpensive and quick upgrade to the pre-existing linac. Another advantage of the design is that it was relatively straightforward to collide with a longitudinally polarized electron beam[47]. Using a polarized electron beam increases the analyzing power of some electroweak measurements, such as the asymmetries

described in chapter 1.

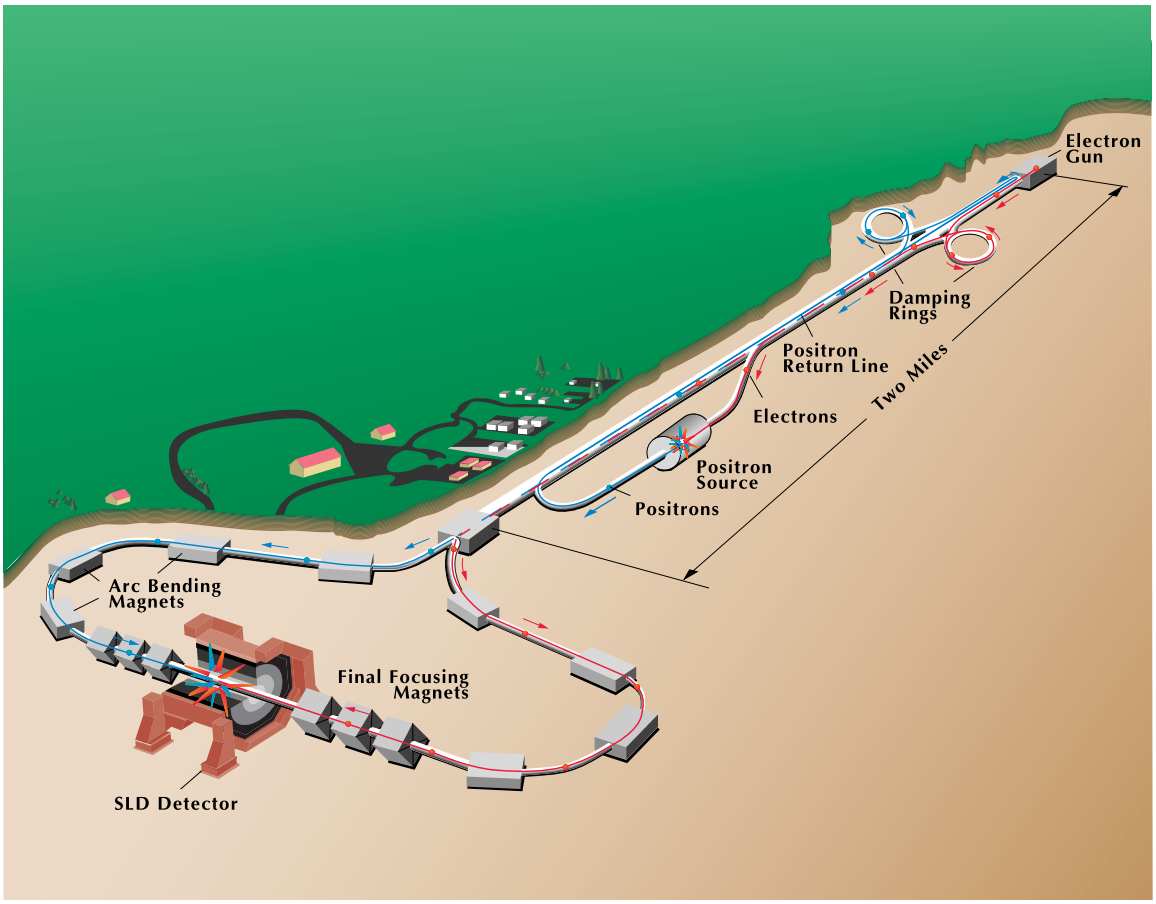

Figure 10: The layout of the SLC

Linear colliders will be necessary for the next generation of higher energy e^+e^- colliders. For relativistic electrons, the energy loss due to synchrotron radiation is proportional to E^4/R where E is the energy and R is the radius of the ring. Thus keeping these losses under control at higher energies will require larger rings than are affordable. The more practicable alternative is thought to be the use of linear accelerators to accelerate beams into each other without recirculation, even though the technology of storage rings is better understood. The SLC is in some respects a hybrid, as it uses one linear accelerator to accelerate both beams. Thus, the beams do get bent in the arcs on their way to the collision point and synchrotron radiation does cause a small energy loss of ~ 1 GeV. Nevertheless, SLC allows one to test the

feasibility of the design. Because the beams are brought into collision only once, they are tightly focused in order to produce acceptable luminosities.

2.1.1 The Polarized Electron Source

The polarized source consists of a photocathode illuminated by pulses of circularly polarized laser light from a frequency-doubled Nd:YAG laser, as shown in Figure 11. The polarization of the light was changed randomly to reduce systematic effects associated with using only one laser polarization. The knowledge of the polarization state of the laser light was transported to SLD using several methods to ensure its accuracy. The wavelength of the light was chosen to be slightly higher than the band gap energy of the photocathode for photoemission to occur. Angular momentum conservation leads to differing transition rates between different angular momentum states in the valence and conduction bands of the photocathode material. The photocathode used during the 1992 run was bulk GaAs, and photoelectrons were produced by transitions from the $S_{\frac{1}{2}}$ valence band to the $P_{\frac{3}{2}}$ conduction band. For a right-handed photon polarization, the transition rate to the $m_j = -1/2$ state is three times larger then the transition rate to the $m_j = 1/2$ state, leading to a 50% polarization. The true polarization available was less due to the excitation of conduction band electrons. In the 1992 run, the average polarization was $\sim 28\%$. For the 1993 run, a strained-lattice GaAs photocathode was used instead in order to remove the degeneracy of the $P_{\frac{3}{2}}$ state and allow higher polarization [48]. During the 1993 run the average polarization was $\sim 62\%$. For the initial $\sim 20\%$ of the run, the laser wavelength was initially set to 850 nm ($\mathcal{P}_e = \sim 55 - 60\%$ at $\lambda = 850$ nm), and was later raised to 865 nm to provide a higher polarization ($\mathcal{P}_e = \sim 62 - 67\%$ at $\lambda = 865$ nm). The photocathode was periodically cesiated to increase the photocathode current, by lowering the energy needed to free conduction electrons from the cathode.

The electrons emitted from the photocathode are bunched by a 178 MHz RF field. Two laser pulses are generated during each 120 Hz accelerator cycle, creating two electron bunches, which are then accelerated to 50 MeV, at which point they enter the linac.

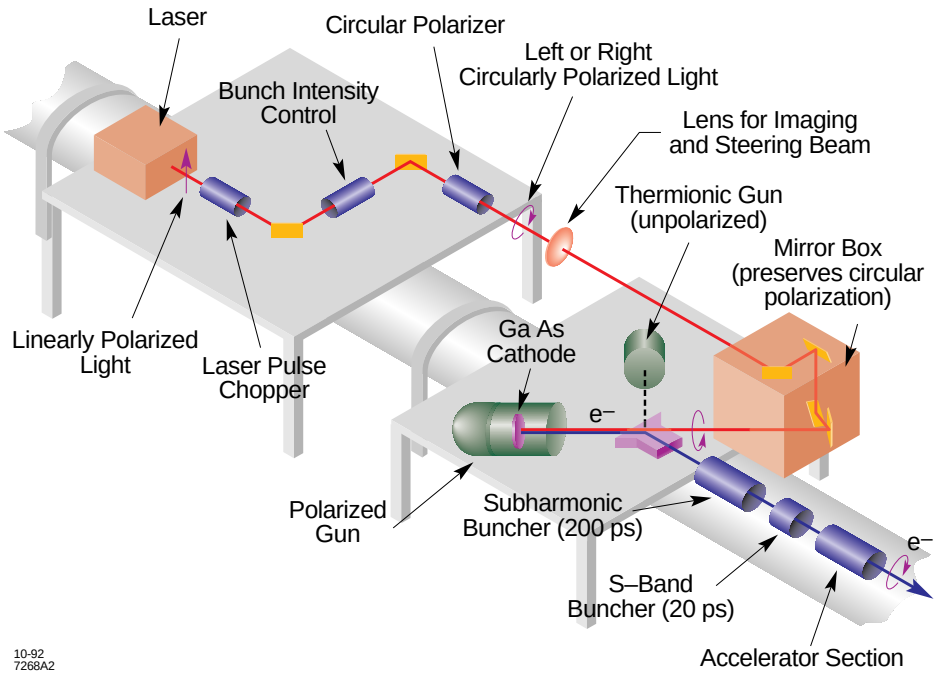

Figure 11: The Polarized Electron Source

2.1.2 The Linac and Arcs

The SLC creates electrons and positrons and transports them to the interaction point (IP) with a 120 Hz cycle. During each cycle, two electron bunches from the source and one positron bunch from the positron return line enter the linac and are accelerated by a field gradient of about 18 MeV/m down its 2 mile length. The positron bunch is produced from the second electron (scavenger) bunch of the previous machine cycle. The electron and positron bunches are accelerated to 1.2 GeV, at which point they are steered into the North and South damping rings, respectively. The damping rings reduce the spatial and energy spread of the bunches through synchrotron radiation. This is done to increase the luminosity and reduce beam-related backgrounds in the detector. The electron bunch spends one machine cycle in the North damping ring, which has been optimized to preserve the electron polarization. The energy spread of the positron bunch is much larger so it is cooled for two machine cycles.

The bunches leave the damping rings and are accelerated further down the linac. The positron bunch for the following machine cycle is produced from the scavenger

electron bunch as follows. After being accelerated to 30 GeV, the scavenger electron bunch is extracted from the linac and directed onto a water-cooled tungsten-rhenium target. The positrons are produced with energies near 1 MeV and are collected and accelerated to 200 MeV in the positron return line. Off-axis and off-energy positrons are removed from the bunch before injection into the low energy end of the linac for acceleration and cooling in the following machine cycle. Approximately one positron is produced for each incident electron, after losses involved in transporting the bunch are taken into account [47].

The first electron bunch and the positron bunch are accelerated to $\sim$ 50 GeV and are then steered through the arcs. Both bunches lose $\sim$ 1 GeV to synchrotron radiation while being steered to the IP. The bunches are focused very tightly at the final focus with three superconducting quadrupole magnets. The dimensions of the bunches were 2.4 μm in the horizontal, 0.8 μm in the vertical, and $\sim$ 1 mm along the beam axis during the 1993 run. Flat beams were found to produce higher luminosities and lower backgrounds than round beams, which had been used in part of the 1992 run. The interaction region extended $\sim$ 700 μm along the z-axis. There is some depolarization of the electron beam in the North arc. Particles that do not interact at the IP are directed to energy spectrometers and then to the beam dumps. The polarization of the electron beam is measured just in front of the beam dump.

2.1.3 The Wire Imaging Synchrotron Radiation Detector

The Wire Imaging Synchrotron Radiation Detectors (WISRDs) [49] are the spectrometers used to make real-time measurements of the energies of the two beams. They are located 150 m beyond the IP, in front of the beam dumps. The basic layout of the WISRD is shown in Figure 12. The beam goes through a series of three dipoles. The first one bends the beam and produces a stripe of synchrotron radiation. The beam is then deflected by the spectrometer magnet by an amount inversely proportional to its energy, and then the third dipole produces a second synchrotron stripe. The synchrotron stripes are focused on a screen of wires that are strung parallel to the stripes. Electrons are Compton scattered off of them and the positions of the two stripes are measured by reading out the residual charge on the hit wires. The

beam energy is calculated using the distance between the two stripes of synchrotron radiation. The resolution of the WISRD is ~ 40 MeV.

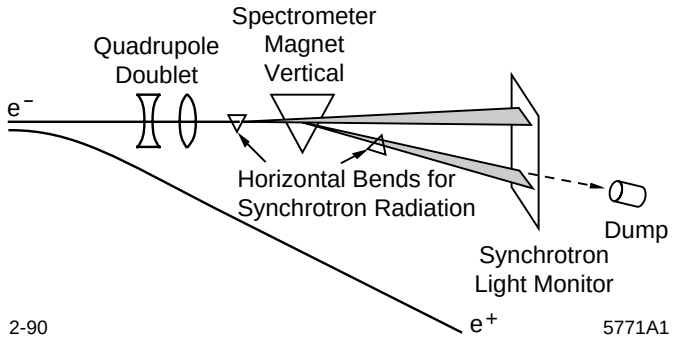

Figure 12: The WISRD spectrometer

2.1.4 The Compton Polarimeter

The magnitude of the electron beam polarization is measured near the IP using the Compton polarimeter, as shown in Figure 13. Electrons that have not interacted at the IP are transported approximately 40 m along a straight path to the Compton IP, where circularly polarized laser light is backscattered off the beam. The Compton scattered electrons are steered away from the unscattered electrons by an analyzing magnet and their momenta are measured from their deflections using a *Čerenkov* detector and a proportional tube detector. The Compton asymmetry and the photon polarization are measured, allowing the electron polarization to be extracted [50]. The Compton Polarimeter is run at 10.9 Hz and measurements are accumulated over 20,000 SLC cycles (approximately three minutes). The statistical error in the polarization measurement is $\sim 1-2\%$. The data is sent to the SLD data acquisition and written to tape. The average polarization for the 1993 run measured using the Compton polarimeter was $\sim 62\%$.

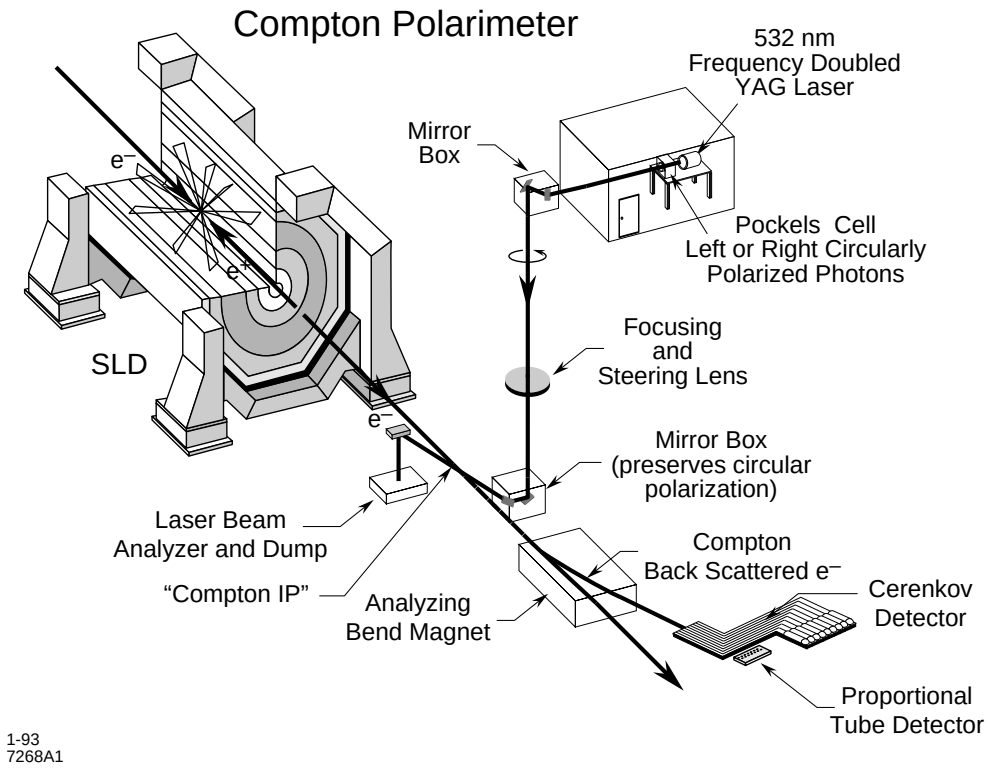

Figure 13: The Compton Polarimeter

2.2 The SLAC Large Detector

The SLAC Large Detector (SLD) is a state-of-the-art collider detector with high precision tracking, calorimetry, and particle identification (see Figure 14). The detector is cylindrically symmetric covering nearly all of the 4π solid angle, and apart from the warm-iron calorimeter (WIC) is placed in a solenoidal 0.6 T magnetic field. The small and stable interaction point (IP) allows the use of a beampipe with a small radius.

E_{cm}	91.26 ± 0.02 GeV/c
Beam spot size	2.6 μm $\times$ 0.8 μm
Number of electrons/bunch	3×10^{10}
Number of positrons/bunch	3×10^{10}
Luminosity	3.8×10^{29} cm^{-2}s^{-1}
	≈ 40 Z^0/hr

Table 7: Performance of SLC during the 1993 run

The tracking systems can thus be placed very close to the IP, providing excellent position and momentum resolution. Most subsystems are divided into a barrel and endcaps; the latter provides coverage at forward angles and can be moved aside for access to the interior of the detector.

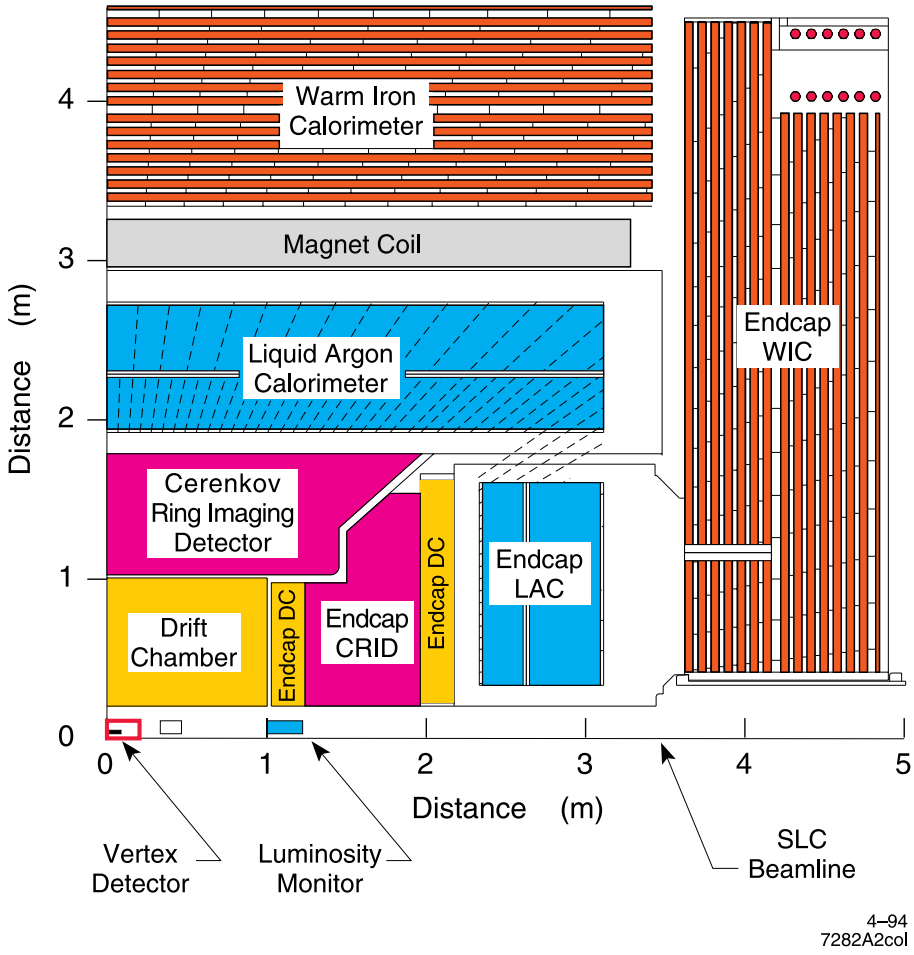

Figure 14: Schematic of SLD

2.2.1 The Vertex Detector

The vertex detector (VXD) [51, 52] is arranged in 4 concentric cylinders around the beampipe to provide tracking close to the beam axis and covers $\sim 75\%$ of 4π. Table 8 summarizes some of the important features of the VXD. Charged coupled

devices (CCDs) are used to detect charged particles passing through them. CCDs consist of a large number of small pixels, and charged particles passing through them deposit charge mostly in the $\sim 1-2$ pixels closest to them. CCDs, unlike strip detectors, are able to provide very accurate tracking along two dimensions without ambiguities. They are consequently less affected by backgrounds such as δ-rays, which can be removed by pattern recognition, and even high densities of tracks can be separated efficiently. This makes them very suitable for use at SLD where beam-related backgrounds are high. The readout time of individual CCD chips is long ($\sim$ 50 ms) because it is done serially, and 152 ms (19 beam crossings) are needed to read out the full VXD. At LEP, the higher collision rate makes the use of CCDs impractical. The long readout time does not create dead time in the VXD, but the backgrounds are consequently increased. The large number of pixels in the VXD minimizes this problem.

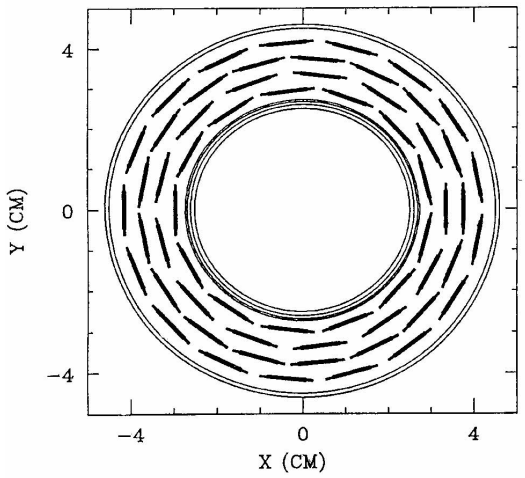

Figure 15: Transverse section through the vertex detector (VXD)

The CCDs are mounted in sets of eight on ladders made of aluminum and ceramic. Each side of the ladder has four CCDs that overlap the CCDs on the other side so that there are no holes in coverage along the length of the ladder. The ladders are arranged in two pairs of concentric barrels and the ladders in one barrel are staggered with respect to those in the other barrel in the pair. Thus, the active regions of each pair of barrels provides complete azimuthal coverage. If the polar angle θ of a

track is such that $|\cos\theta| \leq 0.77$, it will pass through at least 2 cylinders; on average, tracks from the interaction point pass through 2.3 CCDs. In this way the VXD provides three dimensional tracking information near the beam axis in the barrel region, enabling SLD to separate secondary vertices, such as in heavy flavor decays, from the primary vertex with high efficiency. The material of the VXD has been minimized to reduce multiple scattering which can adversely affect the momentum resolution of the tracking system. To help achieve this, the CCD chips are thinned to 200 μm and the ladder support system is made of beryllium. The total thickness of the material at 90° is 5.8% of a radiation length.

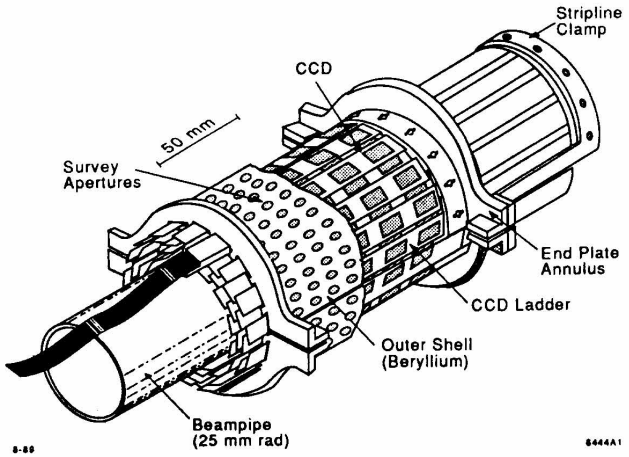

Figure 16: The vertex detector (VXD)

The VXD was optically surveyed to provide relative positions of CCDs, both on the same ladder and on different ladders. The alignment between ladders was done using Z^0 decay tracks. Tracks with ≥ 3 VXD hits are used to correct the surveyed positions, thus improving the spatial resolution. Hits in the VXD are used in combination with fitted tracks from the central drift chamber (CDC, see below). Pattern recognition is used to search for VXD hits associated with CDC tracks extrapolated to the VXD. Tracks with at least 2 VXD hits are kept if the fit quality for the combined VXD and CDC hits is good. The efficiency for linking VXD points with CDC tracks is 96% for regions where all CCDs are active ($p > 1$ GeV/c). The backgrounds (amounting to $< 0.01\%$ occupancy) caused 4% of tracks with $p < 1$ GeV/c to have incorrect clusters

associated with them; for $p > 1$ GeV/c, this was $< 0.5\%$.

The spatial resolution of the VXD was measured using CDC tracks with 3 hits in the VXD. If 2 hits are on the same ladder, the resolution is 5 μm in xy and 8 μm in rz; if the hits are on different ladders, the resolution is 10 μm in xy and 8 μm in rz. The impact parameter resolution [52, 53] has been measured from the miss distances of muons in $Z^0 \to \mu^+\mu^-$ decays: $\sigma_{xy} = 15.7\mu$m, $\sigma_{rz} = 46.5\mu$m at high p_t.

The VXD is maintained at 195 K in a cryostat by flowing cold nitrogen gas through it. By cooling the VXD, the dark current of the CCDs and electronics noise is reduced to a minimal level: < 1 hit /CCD per event.

After installation, one inefficient ladder, two dead CCDs and 3 inefficient CCDs were found which amounted to $\sim 4\%$ of the CCD channels being faulty. This reduced the linking efficiency for tracks traversing the faulty regions of the VXD.

pixel size	22 μm $\times$ 22 μm
number of pixels/CCD	222,530
active area of ladder	$8.5 \times 100\mu$m^2
number of ladders	60
barrel radii	29.5, 33.5, 37.5, 41.5 mm
thickness of material at 90°	5.8% X_0
spatial resolution (xy)	$5 - 10\mu$m
spatial resolution (rz)	8 μm
impact parameter resolution (xy)	15.7 μm
impact parameter resolution (rz)	46.5 μm
two-track resolution	40 μm

Table 8: VXD parameters

2.2.2 The Drift Chambers

Further charged particle tracking is provided by the drift chambers. There is a central drift chamber (CDC) in the barrel region and two endcap drift chambers (EDCs) in the north and south endcaps. Both drift chambers work by measuring the ionization of a gas that results from the passage of charged particles through it. An electron produced in this primary ionization drifts towards a sense wire held at high voltage,

producing an avalanche in its vicinity. By measuring the time of the cascade, the drift distance and thus the position of the primary ionization, can be deduced.

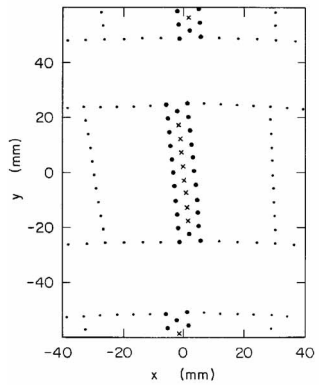

Figure 17: Schematic of a CDC cell showing the placement of guard wires, field wires and sense wires

The CDC is a 2 m long cylindrical annulus around the VXD, extending from a radius $R_{\text{inner}} = 0.2$ m to $R_{\text{outer}} = 1.0$ m. It consists of 10 superlayers that contain cells that are ~ 59 mm wide. The longest drift distance is thus ~ 30 mm, corresponding to a ~ 3.3 μs spread in drift times. Each cell has eight sense wires, 24 guard wires and 27 field wires (see Figure 17) that are strung in the axial direction. The arrangement of guard wires and field wires maintains a more constant relationship between drift time and the distance traveled by the drifting electrons than would be the case with just a single sense wire and guard wire. The sense wires are instrumented at both ends with charge amplifiers that measure a hit on a wire as a charge. The charge is inversely proportional to the resistance and therefore to the length of the wire from the hit to the end. The z coordinate of the hit can be measured using charge division in which the charges collected at the two ends of a hit wire are compared. However, this is sensitive to noise and electronics problems, and has a resolution of 6 cm. A single track traversing a CDC cell creates ~ 16 electrons through primary ionization which results in an avalanche of $\sim 3 \times 10^6$ electrons.

When a sense wire is hit, the side of the sense wire where the primary ionization occurred is ambiguous. In track reconstruction, hits are assigned to both sides of the sense wire and pattern recognition is used to remove the fake reflected image. When

σ_θ	3.7 mrad
σ_ϕ	0.45 mrad
σ_{xy}	$\sim 50 - 100$ μm for most of cell
	~ 200 μm near sense and field wires
σ_p	$0.0049 \oplus 0.0095/p$ (CDC+VXD)
$\sigma_{r\phi}$	$13 \oplus 70/p\sin^3\theta$ (CDC+VXD)
σ_{rz}	$52 \oplus 70/p\sin^3\theta$ (CDC+VXD)

Table 9: CDC parameters (p is expressed in GeV/c)

a track traverses a cell and ionizes the gas, the showers produced have finite length. This creates a dead band of $\sim$1 mm next to the sense wire, and a corresponding reflected dead band on the other side of the sense wire. Other tracks passing through these dead bands cannot be resolved by the cell. By tilting the cell by 5° from the radial direction, the reflected dead band is inclined by 10° to the interaction point. It is then less likely that the reflected dead band will kill segments of other tracks and the two-track resolution is better than it would be without the tilt.

The polar angle and z measurement are improved by having some superlayers with a stereo angle. Three (U) superlayers are tilted by a stereo angle of +41 mrad, three (V) are tilted by −41 mrad, and four (A) have no stereo angle (axial layers). The arrangement is AUVAUVAUVA. The position of a hit in the stereo layers is a function of z and when fitting all the layers together, the z coordinate of the track can be extracted with a resolution of 1 mm.

The gas used is a mixture of 74.7% CO_2, 21% Ar, 4% isobutane and 0.3% H_2O. These concentrations are maintained within $\pm$0.15% and the oxygen concentration is kept below 20 ppm. The drift velocity is sensitive to the density of the gas mixture and the voltage of the drift field. Consequently, the pressure and temperature are closely monitored and kept as constant as possible. The drift velocity is independently measured on a run-by-run basis as a cross-check using tracks. The radiation thickness is quite small: 5.3% radiation lengths in total, and 1.8% rad length is beyond the active region on the outer wall. Table 9 summarizes the resolutions achieved in the CDC.

The EDCs are each composed of two sections: an inner and outer layer. The

endcap CRIDs are sandwiched between these layers allowing better track extrapolation into the CRID. The technology employed is the same, but the wires are strung differently. Data from the EDC was not used in this analysis.

2.2.3 The Čerenkov Ring Imaging Detector

Particle identification is provided at SLD by the barrel and endcap Čerenkov Ring Imaging Detectors (CRIDs). The CRIDs exploit the Čerenkov effect to measure velocities of charged particles. Combined with a momentum measurement from the tracking system, the CRID can separate particles by their masses. The CRIDs are useful for the following identifications: e, π, K.

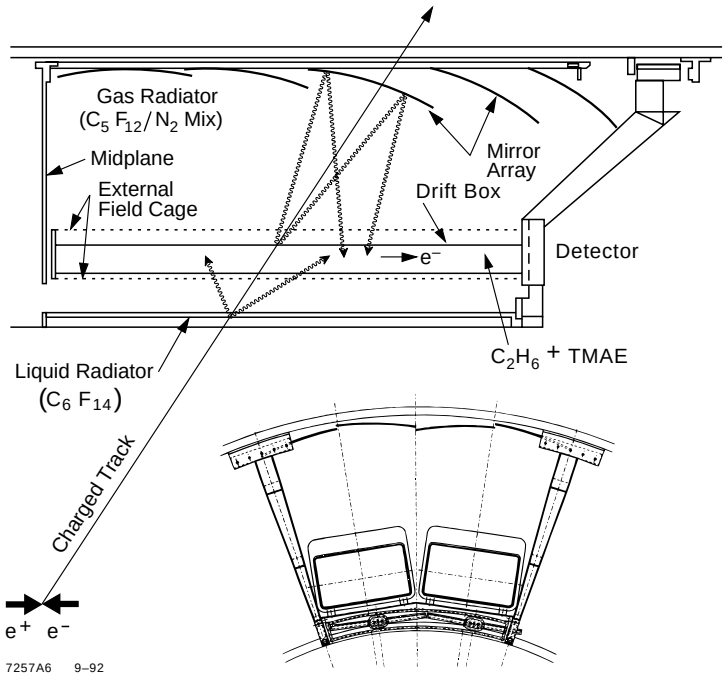

Figure 18: Schematic of the barrel CRID

The Čerenkov effect occurs when the velocity of a charged particle exceeds the velocity of light in the dielectric medium it is traversing. The particle polarizes atoms in its vicinity which then coherently emit radiation at an angle θ that is related to

momentum threshold (for 3 p.e.) (GeV/c)	liquid	gas
e	~ 0.001	~ 0.0095
π	0.23	2.6
K	0.80	9.1
p	1.50	17.3

Table 10: Momentum thresholds for the gas and liquid radiator in the barrel CRID

the velocity β of the particle and the refractive index n of the medium by

$$\cos\theta = \frac{1}{\beta n} \tag{143}$$

Thus, for the effect to occur, $\beta n > 1$, i.e. there is a threshold velocity $\beta_t = 1/n$ below which light will not be emitted. Above this threshold, the Čerenkov angle θ increases with velocity β. There is thus a maximum Čerenkov angle that corresponds to $\beta = 1$:

$$\theta_{max} = \cos^{-1}(1/n) \tag{144}$$

In media with different n, the Čerenkov angle will have its greatest velocity resolution in different ranges of velocities.

The CRIDs work by imaging cones of Čerenkov light as rings. The radii of the rings measure the Čerenkov angle. The yield of photons is very low but this is not a problem. In principle, the radius of a ring can be fixed even if only one photon is detected if the center of the ring is known from the tracking systems. In practice, because of detector inefficiencies and a high multiplicity environment, more photons are needed to measure a ring radius. To maximize the photon yield, the CRID collects photons from the ultraviolet where Čerenkov radiation is strongly peaked. In this region of the spectrum, they can also be detected with very high efficiency using the photoelectric effect. Consequently, the CRID must be made transparent to the ultraviolet.

The barrel CRID uses both a liquid radiator, C_6F_{14}, and a gas radiator, a mixture of 70% C_5F_{12} and 30% N_2. The refractive index of the gas ($n = 1.00173$ at 6.5 eV) is much lower than that of the liquid ($n = 1.277$ at 6.5 eV), making it more sensitive to high energy particles. The momentum thresholds for detecting at least three photoelectrons are shown in Table 10.

A schematic of the barrel CRID is shown in Figure 18. A particle entering the CRID from the drift chamber passes through a 1 cm layer of liquid radiator enclosed in a box with a quartz window (for transmission in the ultraviolet). Čerenkov radiation from the liquid radiator propagates a short distance and then forms rings inside a drift box situated behind the liquid radiator. Typical liquid rings have a 17 cm radius and are 1.5 cm thick. After the liquid radiator, a charged particle will traverse a ~ 45 cm gas radiator volume. The Čerenkov radiation that is produced is focused onto the drift box by an array of spherical mirrors on the far side of the CRID. A typical gas ring has a 3 cm radius and is 3 mm thick.

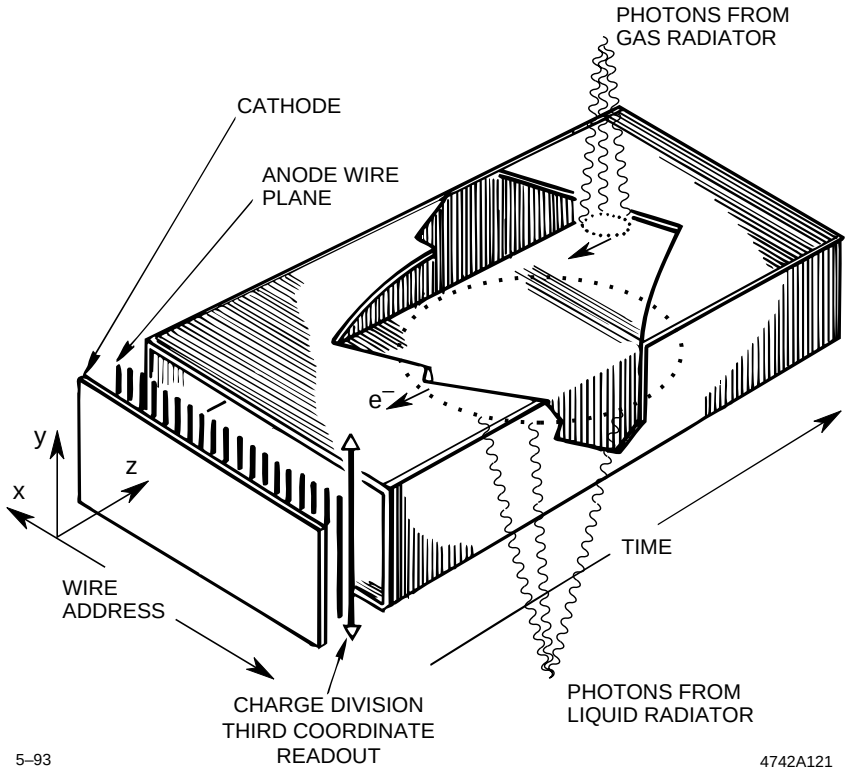

Figure 19: Schematic of a drift box in the CRID

The drift box is shown in Figure 19. It has an active area of 126.8 cm $\times$ 30.7 $\times$ 5.6 cm and is filled with a mixture of C_2H_6 and 0.1% TMAE (Tetrakis Dimethyl Amino Ethylene). TMAE has an extremely low ionization threshold of 5.36 eV and has a very high quantum efficiency in the range 1700 to 2200 $\mathring{A}$. At $\beta = 1$, liquid rings

have $\sim 13-16$ photoelectrons and gas rings have $\sim 7-9$. The drift box has quartz walls for ultraviolet transparency, and is enclosed in a cage of field wires that provide a uniform drift field of 400 V/cm. The drift velocity is ~ 4.385 cm/μs and is closely monitored, as it is strongly affected by impurities in the drift gas. Photoelectrons are drifted towards the end of the box where they are detected by a MWPC which has an anode wire plane containing 93 thin high-resistivity carbon wires spaced 3.175 mm apart. A position in x, y, and z can be measured for each photoelectron from the address of the hit wire, charge division along the wire, and the drift time, respectively, with resolutions of 1 mm, 2 mm, and 1 mm, respectively.

particle separation range at 90° (3 σ level)	gas and liquid
e/π	0.2-6.2 GeV/c
μ/K	0.2 - 1.1 GeV/c liquid
	2.1 - 3.8 GeV/c gas
π/K	0.23 - 23 GeV/c
K/p	0.8 - 37 GeV/c

Table 11: Momentum ranges for particle separation in the barrel CRID

Table 11 shows the momentum ranges over which different particles can be separated. Figure 20 shows results from the liquid radiator in the barrel CRID during the 1992 run. The separation into π, K, and p bands can be easily seen. The slices in Figure 20 (b) and (c) show the different degree of separation between particles in different momentum ranges.

The endcap CRID [51, 54] has a similar design to the barrel CRID, but with no liquid radiator. The radiator gas is a mixture of 85% C_2H_6, 15% CO_2, and 0.05% TMAE. The photoelectrons drift perpendicular to the magnetic field, so there is a non-zero Lorentz angle ($\theta_L \sim 10°$) that needs to be compensated for in the MWPC focusing structures. Without a liquid radiator, the endcap CRID is sensitive to particles with medium to high momenta. The momentum thresholds are 2.5 Gev/c for pions, 8.9 GeV/c for kaons, and 17.0 GeV/c for protons. $\pi/K/p$ separation is achievable up to momenta of ~ 30 GeV/c.

The Endcap CRID was being commissioned during the 1993 run. Neither the

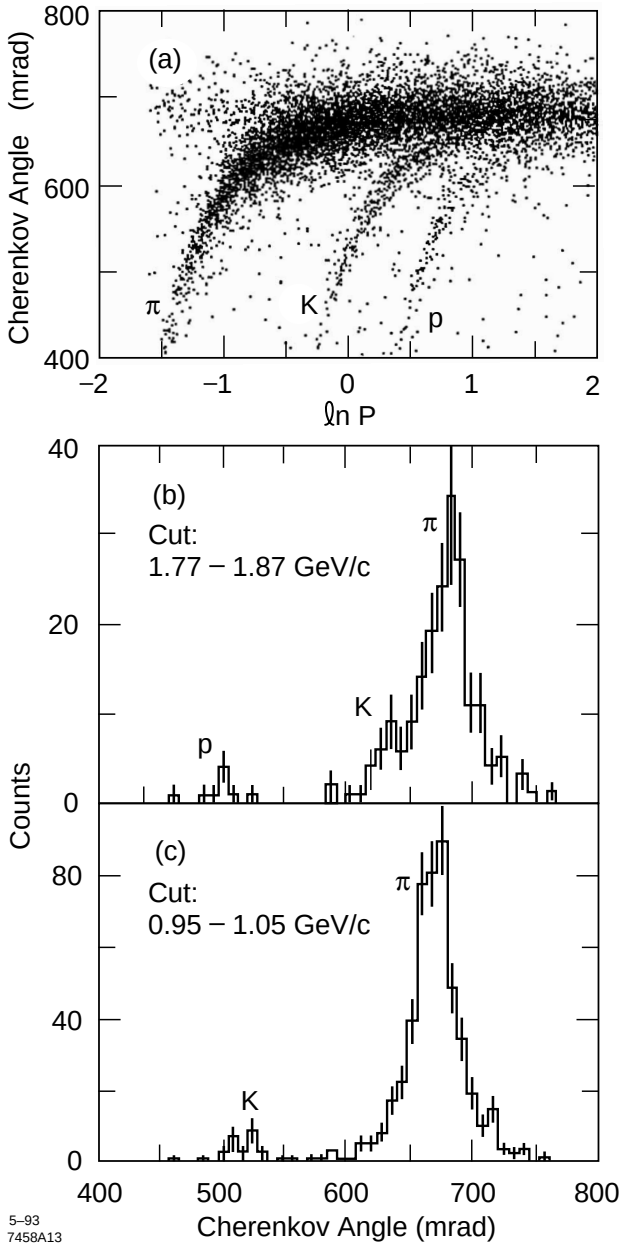

Figure 20: Results from liquid rings in the barrel CRID during the 1992 run: (a) spectrum, (b) and (c) slices of (a) for different ranges of momenta.

barrel nor the endcap CRID are used in this analysis.

2.2.4 The Liquid Argon Calorimeter

The LAC is the primary electromagnetic and hadronic calorimeter in SLD, employing lead as an absorber and liquid argon as the active medium. The LAC is divided into three regions: a barrel ($|\cos\theta| < 0.83$) and two endcaps ($0.82 < |\cos\theta| < 0.99$), but is treated as a single entity by the data acquisition. Each region has its own cryostat in which the lead plates are immersed in liquid argon. The liquid argon is cooled by liquid nitrogen flowing through tubes in each cryostat.

The passage of particles through the lead creates showers of lower energy particles that then ionize the liquid argon as they pass through it. The lead layers are alternately held at ground and at 2 kV, so that the ionization of the liquid argon can be measured. Lead is a useful material for both electromagnetic and hadronic calorimetry because it has both a short radiation length ($X_0 = 0.56$ cm) and a short interaction length ($\lambda = 17.1$ cm). Liquid argon has numerous advantages as the active medium. Ionization can be measured locally within the active volume, so the readout does not impose as stringent constraints on the geometry as with a scintillator system. There are fewer dead regions because the active medium is a liquid. Liquid argon is radiation hard, so the LAC calibration remains stable and depends only on the electronics. Liquid argon has unity gain so there are no fluctuations associated with the signal which would come about from an amplification process.

The LAC has a projective tower geometry, and the towers are divided in depth into EM1, EM2, HAD1, and HAD2 to give information on longitudinal shower development. The segmentation of the towers in the electromagnetic section is $\delta\phi = 33$ mrad and $\delta\theta$ ranges from 36 mrad at $z = 0$ to 21 mrad at $z = 3.1$ m, which fully contains the lateral spread of a typical electromagnetic shower. In the hadronic section, the towers are twice as wide in ϕ and θ. The endcaps are segmented similarly except at small polar angles, where the ϕ segmentation is coarser. There are a total of 32448 towers in the barrel and 8640 in the endcaps.

The towers are composed of unit cells (see Figure 21) that consist of the ground plane, which is a continuous sheet of lead and a lead tile held at 2 kV, with a 2.75

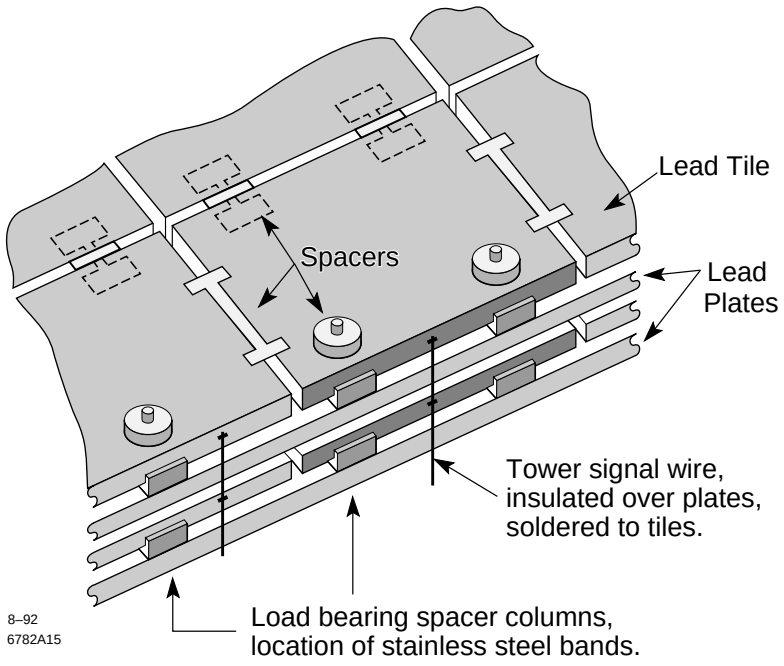

Figure 21: Layout of a LAC cell

mm thick layer of liquid argon separating them. The charge accumulated on the lead tiles is read out and digitized. The lead layers are 2.0 mm thick in EM1 and EM2, and 6.0 mm thick in HAD1 and HAD2. Thus, the sampling fraction is 18.5% in the electromagnetic section and 7% in the hadronic section. The electromagnetic section has a total thickness of 21.11 radiation lengths and 0.84 interaction lengths, which contains $\sim 99\%$ of a typical electromagnetic shower. The hadronic section has a total thickness of 2.84 interaction lengths and 56.74 radiation lengths. The LAC contains $\sim 85\%$ of typical hadronic showers.

The energy resolution of the electromagnetic section is $\sigma_E/E = 15\%/\sqrt{E}$, which was calculated using Bhabha electrons. The hadronic resolution was calculated to be $\sigma_E/E = 55\%/\sqrt{E}$ from a comparison of isolated tracks in the drift chamber and LAC.

The LAC Energy Scale

The conversion of ADC counts to an energy value needs to be well defined for the LAC [55]. However, the response of the LAC depends on the type of particle that is depositing energy. A standard scale is defined using minimum ionizing particles (MIPs) such as muons:

EM 1 ADC count = 2.04 MeV

HAD 1 ADC count = 5.41 MeV

Both electromagnetic showers and hadronic showers deposit more of their energy in the lead, i.e. a smaller fraction of their energy is deposited in the liquid argon. Thus, the standard scale energies need to be scaled by 0.68 and 0.42 for electromagnetic and hadronic showers [49], respectively. This is done during reconstruction when clusters are identified as arising from either electromagnetic or hadronic showers.

2.2.5 The Magnet

The magnet is located between the barrel LAC and the barrel WIC. It is a 5.9 m diameter, 6.4 m long and 29 cm thick aluminum coil, and is water-cooled. It is wound with $\sim$ 10 km of 5×5 cm^2 aluminum conductor in four layers of 127 turns. The magnet is run at a current of 6600 A and its field is measured to be:

$$B_z = 0.0203 \text{ T and } B_r = 0.0203 \text{ T}. \tag{145}$$

The field has been modeled and the agreement with the measured field is within 0.05% in the CDC. Thus, the 3% variation of the field that exists within the CDC can be calibrated away.

2.2.6 The Warm Iron Calorimeter

The Warm Iron Calorimeter (WIC) has three functions. It acts as a secondary hadronic calorimeter: approximately 5% of the energy of a typical hadronic Z^0 decay is deposited in the WIC. As a flux return, it ensures the uniformity of the magnetic

field within the barrel, in particular the CDC. The WIC also detects muons that are able to traverse the rest of the detector.

The WIC has octagonal symmetry in ϕ and has a projective tower geometry that is a continuation of the LAC towers. It is also segmented longitudinally into two layers that are each 2.1 interaction lengths thick. There are 14 layers of 5 cm thick iron separated by 3.2 cm gaps containing Iarocci tubes. An extra set of Iarocci tubes follows the seventh and fourteenth layers. Iarocci tubes are long plastic tubes lined with conductive paint with a Cu-Be wire at 4.75 kV inside. The tubes are filled with a mixture of 88% CO_2, 9.5% isobutane and 2.5% argon. The tubes are sandwiched between electrode sheets which are segmented either into rectangular pads or as strips that run parallel to the wires. The extra Iarocci tubes on layers 7 and 14 have 2 sets of strips: one transverse and one longitudinal to the wire. Charged particles traversing an Iarocci tube ionize the gas mixture and an avalanche is created as the electrons drift to the wire. A signal is induced on the electrodes surrounding the tube. An analog signal is read from the strips, which with charge division can track muons in x, y and z. The pads are read out digitally.

Muon candidates are found by eliminating hadron showers from the sample. Hadronic showers are more widely dispersed in angle and position than muons. Pattern recognition using tracking and LAC information is used to further separate muon candidates from hadrons. However, π and K decays into muons in the drift chambers or CRIDs can create a fake primary muon signal. Studies [56] indicate that this can be reduced to the level of 10^{-3}.

The combined hadronic energy resolution of the LAC and WIC is $\sigma_E/E = 60\%/\sqrt{E}$ where E is in GeV.

2.2.7 The Luminosity Monitor and Forward Calorimetry

Electromagnetic calorimetry in the forward region and luminosity monitoring are provided by the Medium Angle Silicon Tagger (MASiC) and the luminosity monitor/small angle tagger (LMSAT), respectively. There are identical MASiC and LMSAT on the north and south ends of the detector. The construction of the two systems is very similar; they are both silicon-tungsten sampling calorimeters.

The MASiC consists of 10 layers of tungsten, each 1.74 radiation lengths thick with silicon diodes between them. It is divided into two longitudinal sections, EM1 and EM2, consisting of the first three layers and the last seven, respectively. The angular coverage of the MASiC is 68 mrad $< \theta <$ 190 mrad. The MASiC is arranged into towers with $\delta\theta = 36$ mrad and $\delta\phi = 11.25°$ for the outer portion and $\delta\phi = 22.5°$ for the inner portion.

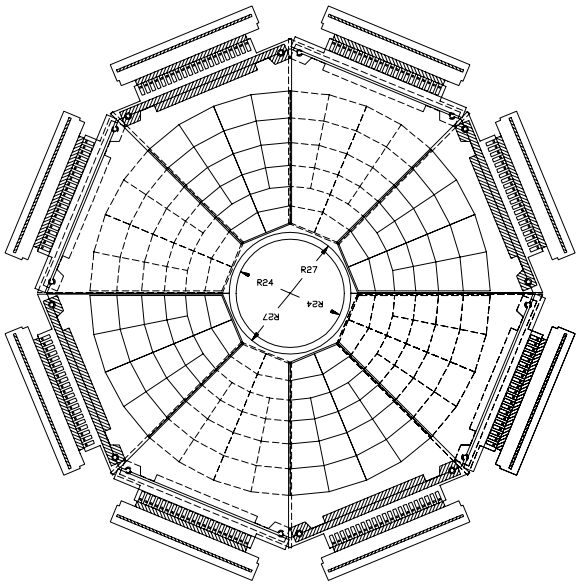

Figure 22: Schematic of the luminosity monitor

The LMSAT consists of silicon diodes sandwiched between 23 tungsten layers that are 0.92 radiation lengths thick. Figure 22 shows a schematic of the LMSAT. The angular coverage is 28 mrad $< \theta <$ 65 mrad. It is longitudinally divided into EM1 and EM2 which are 5.5 and 15.6 radiation lengths thick, respectively. It is segmented into towers with the same ϕ segmentation as in the MASiC and $\delta\theta = 9$ mrad. The LMSAT provides an excellent measurement of low-angle Bhabha electrons, containing $> 99.5\%$ of their energy. The energy resolution is $\sigma_E/E = 20\%/\sqrt{E}$. The low-angle Bhabha cross-section is dominated by t-channel photon exchange and can thus be calculated to high precision. There are ~ 2.5 low-angle Bhabha events per hadronic

Z^0 decay. The integrated luminosity can be measured by counting these events:

$$\int \mathcal{L}dt = \frac{\text{number of low-angle Bhabha events}}{\text{calculated low-angle Bhabha cross-section}} \tag{146}$$

2.3 Data Acquisition

[57] The trigger rate at SLD is dominated by beam background because of the relatively low e^+e^- cross-section and low collision rate. Thus, the acquisition does not have to run as fast as at a hadron collider. The low radiation environment of an e^+e^- collider allows the front-end electronics to be placed directly on the detector thus improving signal quality. The signals can be time multiplexed before being sent from the detector, thus reducing the channel count (and its associated cables) further down the acquisition chain. The beam crossing rate of 120 Hz implies that trigger decisions must be made within 8.3 ms.

After each beam crossing the signals from each subsystem are amplified, shaped and stored in preparation for a relatively slow digital readout. The details pertaining to each subsystem are described below.

VXD

Because of their design, each CCD in the VXD must be read out serially. The signals are amplified, filtered and digitized by electronics on the ladders. Two dimensional clusters are constructed before they are sent to FASTBUS. The VXD takes 160 ms to be read out and is not used by the trigger.

Drift Chambers and CRIDs

The drift chambers and CRIDs process and transport their signals in similar ways. The sense wires are instrumented with preamplifiers that are connected to Hybrid Analog Memory Units (HAMUs) that sample and store 512 waveform points. If the trigger requests it, the waveforms in the HAMUs are read out, digitized and shipped to FASTBUS which takes $\sim$ 64 ms. The CRIDs handle a higher dynamic range than the DCs and have preamplifiers that are modified to cope with this. The drift

chamber is also used by the trigger and a stripped version of CDC information is supplied: the output from each preamplifier is discriminated, providing a list of hit wires in the drift chamber (1 bit/wire).

LAC and WIC

The LAC and WIC pads are read out in a similar fashion. The signal from each channel is preamplified and stored in a Calorimeter Data Unit (CDU). The CDU samples the data at two gain ranges. The CDU signal is digitized, serialized and multiplexed before being transmitted to FASTBUS. The LAC can be read out in 2 ms which is fast enough for the trigger to use. The WIC strips are preamplified and discriminated, and then read out and clustered by the Digital Readout Module (DRM).

2.3.1 FASTBUS

FASTBUS coordinates and receives data from all the subsystems on the detector. The data is processed further in specialized modules, e.g. WSMs for DCs and CRIDs and CDMs for the calorimetry. The data is corrected by applying calibration constants, and then compacted to contain only the pulse and its leading and trailing edges. Timing and Control Modules (TCMs) synchronize the detector to the CDMs and WSMs and control the configuration of the electronics on the detector. Each subsystem has an Aleph Event Builder (AEB) that further organizes the data and prepares it for transmission to the data acquisition computer that writes the data to tape.

The trigger decisions are processed by FASTBUS. The drift chamber information is further reduced to 1 bit/cell, and various weighted energy sums are calculated by the CDMs and organized by the calorimeter AEB. This trigger information is sent to the trigger AEB which uses a lookup table to find tracks and makes trigger decisions in ~ 3 ms. The trigger will be described in more detail in chapter 4.

Chapter 4

Triggering and Event Selection

The final sample of events used in physics analyses is collected and separated from background events in several stages. First, data from the detector is written to tape if it passes the selection criteria of the trigger. The trigger is designed to be very efficient at selecting Z^0 decays at the expense of purity. The event filter reduces the large sample of events on tape by removing mainly beam-related backgrounds. Event selection cuts are applied to the filtered event sample to extract events of interest for an analysis, viz. hadronic Z^0 decays for this measurement.

4.1 The Event Trigger

The basic task of a trigger is to identify events of interest and write them to tape while rejecting the background. In order to write as many 'interesting' events as possible, purity is sacrificed in the interests of efficiency, as the event sample will be filtered afterwards. The beam crossing rate is 120 Hz which gives the trigger 8.3 ms to make its decision. For the SLD trigger to makes its decision quickly, it must use event quantities that are immediately available, e.g. calorimetry information or primitive tracking information, as described in section 2.3.1. The 1993 run at SLD employed eight triggers [74] as shown below. During a run, all or a subset of these triggers can be armed. The energies are all expressed in the standard/m.i.p. scale (see explanation in section 2.2.4).

Random This trigger is used for collecting minimum bias events for modeling backgrounds in the detector. The full detector is read out every 2400 ± 50 beam crossings. These events do not have to satisfy any trigger requirements.

Energy This trigger requires a total LAC energy greater than 12 GeV from at least 8 towers. Towers contribute if they are above the following thresholds: 60/60/120/120 ADC counts for EM1/EM2/HAD1/HAD2 respectively. Only the calorimeter is read out. Typical rate < 0.01 Hz.

Bhabha This trigger is a small-angle Bhabha trigger using the LUM. It is used in determining the luminosity from the Bhabha cross-section. It requires back-to-back deposition of electromagnetic energy in the LUM: greater than 10 GeV in both LUM monitors with towers in LUM-EM2 contributing if they are above the threshold of 1 GeV. Only the calorimeter is read out. Typical rate ~ 0.25 Hz.

Track This trigger requires at least 2 CDC tracks with an opening angle greater than 30°. The full detector is read out. Typical rate ~ 0.05 Hz and this is rate limited to 0.1 Hz.

Hadron This trigger requires at least 1 CDC track and a total LAC energy of at least 15 GeV. At least 10 towers must contribute to the sum and at least one tower must be in the forward and one in the backward section of the barrel. Towers contribute to the energy sum if they are above the same thresholds as for the energy trigger. Most energy triggers also satisfy this trigger. The full detector is read out. Typical rate 0.01 Hz.

WAB This trigger requires a total LAC EM energy greater than 30 GeV with towers contributing if above 60 ADC counts. The full detector is read out. Typical rate < 0.01 Hz.

laser_acq This trigger is used in calibrating the drift chambers and is not normally armed. It requires the drift chambers to be read out every time the drift chamber calibration laser is fired.

There are three beam-related backgrounds that the trigger (and the event filter) removes: low energy electrons and photons that scatter off beamline components, SLC muons, and beam-splash. Low energy electrons and photons are vetoed by the LAC energy thresholds, the minimum track momentum ($p_t > 180$ MeV) recognized by Fastbus pattern recognition [51] and the opening angle requirement of the tracking trigger. SLC muons are created by the tails of the electron and positron bunches when they strike collimators in the beam-line. While most of these muons do not reach SLD and are absorbed in the ground or deflected by 'muon spoiler' magnets, some do get trapped and accelerated down the beamline. They leave a distinctive signature of energy deposition in the WIC endcaps and ionization trails parallel to the beam axis in the barrel LAC and WIC. Beam-splash is caused by a 'catastrophic' failure of SLC (which can be caused by just a klystron misfire on one pulse) in which at least one bad bunch is accelerated to the interaction point producing a large shower of energy in the process. This can be recognized by large deposits of energy in the calorimeter and large numbers of uncorrelated hits in the tracking systems. These backgrounds can set the track trigger which is therefore rate-limited to 0.1 Hz to reduce the impact of noisy beam conditions. The CDC trigger is also vetoed if more than 275 CDC cells have at least 6 hit wires. High energy thresholds reduce this background in the energy trigger.

In the middle 40% of the 1993 run, a hardware problem occurred in the CDC. This was interpreted by the trigger as an increase in the CDC occupancy which caused the CDC occupancy veto to occur more frequently than it should have. As a result, approximately 12% of hadronic events do not have tracking information, i.e. the hadronic trigger is vetoed but not the energy trigger. This is simulated in the Monte Carlo by rejecting a larger proportion of events in this part of the 1993 run.

4.2 Event Filtering

Useful physics events make up only a small fraction of the large number of triggers recorded. The general procedure is to filter out the events of interest and then fully reconstruct these, after which further selection cuts can be applied to extract the

events required by a particular analysis. The event filtering for the 1993 run at SLD is done in two stages called Pass 1 and Pass 2.

4.2.1 Pass 1

The Pass 1 filter eliminates $\sim 97\%$ of events that are triggered and written to tape in the 1993 run [75]. The remaining events are classified into physics and non-physics categories according to the triggers they satisfy and the cuts they pass in the Pass 1 filter. The physics event categories are:

- Z decay products (hadronic, tau-pairs and mu-pairs)
- LUM Bhabhas
- track triggers

and the remaining event categories are:

- Compton polarimeter records
- DC laser records
- random triggers
- 120 Hz trigger records
- almost all LUM triggers.

Because this analysis uses hadronic Z decays, the filtering of these events is now described. Events are classified as hadronic Z decays if they pass either the LAC energy trigger (EIT) filter or the KAL Z (KZ0F) filter. The EIT filter requires the following LAC quantities to be defined

- E_{HI}: the total energy from all LAC towers that are above a 'high' threshold. The 'high' threshold is 60 ADC counts ($\sim$ 250 MeV) for the EM sections and 120 ADC counts ($\sim$ 1.3 GeV) for the HAD sections.

filter quantity	cut value
E_{HI}	> 15 GeV
E_{LO}	< 140 GeV
E_{HI}	$> 1.5(E_{LO} - 70)$ GeV
N_{HI}^{EM}	≥ 10
N_{HI}^{EM}(north only)	> 0
N_{HI}^{EM}(south only)	> 0

Table 13: Pass 1 LAC energy (EIT) filter cuts

- E_{LO}: the total energy from all LAC towers that are above a 'low' threshold. The 'low' threshold is 8 ADC counts ($\sim$ 33 MeV) for the EM sections and 12 ADC counts ($\sim$ 130 MeV) for the HAD sections.

- N_{HI}^{EM}: the number of towers in the EM section above the 'high' threshold.

For an event to pass the EIT Pass 1 selection, it must have satisfied the energy trigger conditions and pass the cuts shown in Table 13. N_{HI}^{EM} correlates well with the particle multiplicity of the event and should be high for events with hadron-like multiplicities. Backgrounds populate low values of N_{HI}^{EM} and are reduced by the cut. The SLC muon background manifests itself as large numbers of low energy hits in the LAC and it can be reduced by the cuts on E_{LO}. The north-south energy requirement reduces beam-splash background which can be asymmetrical along the beam axis.

The KAL Z filter uses the following quantities.

- E_{WIC}^{ec}: the sum of the energy in the endcap WIC towers that have less than 6000 ADC counts and non-isolated hits.

- E_{LAC}: the energy sum of LAC towers above 0, 60, 120, and 120 ADC counts for the EM1, EM2, HAD1 and HAD2 layers respectively.

- N_{LAC}: the number of LAC towers above the readout thresholds (see previous chapter, section 2.2.4), which are 2, 3, 6 and 6 for the EM1, EM2, HAD1 and HAD2 layers respectively.

The cuts are shown in Table 14. The fourth cut is optimized for rejecting the SLC muon background.

filter quantity	cut value
N_{LAC}	$> 0, < 3000$
E_{LAC}	> 14 GeV
E^{ec}_{WIC}	< 11 GeV
$1.45E_{LAC} - E^{ec}_{WIC}$	> 8.7 GeV

Table 14: Pass 1 KAL Z filter cuts

4.2.2 Pass 2

All physics events passing the Pass 1 filter are then processed by the Pass 2 filter which reconstructs the events and applies cuts to classify them further. Hadronic Z decays passing the Pass 1 EIT filter are processed by the Pass 2 EIT filter. The calorimetry information is reconstructed for the event using only the LAC contribution from towers above thresholds of 7 and 9 ADC counts for the EM and HAD sections respectively. The LUM and WIC contributions are not used and towers closest to the beampipe are also ignored. Clusters are constructed such that

- $E_{clus} > 100$ MeV
- $E^{EM}_{clus} > 0$ MeV.

Clusters that are inconsistent with being from SLC muons are used to construct the following quantities

- E_{TOT}: the total (uncorrected) cluster energy
- E_{imb}: the energy imbalance, the magnitude of the vector sum of the cluster energy divided by E_{TOT}
- N_{clus}: the number of clusters

The EIT2 cuts are shown in Table 15. Most physics events should have a symmetrical distribution of energy and the E_{imb} requirement removes some beam-related backgrounds. The other cuts identify hadronic Z decays by their characteristically large energy and high multiplicity (assuming that N_{clus} correlates with the particle multiplicity).

filter quantity	cut value
E	> 13.5 GeV
E_{imb}	< 0.6
N_{clus}	> 8 for $\cos\theta_{clus} < 0.8$
N_{clus}	> 11 for $\cos\theta_{clus} > 0.8$

Table 15: EIT Pass 2 cuts

Visible energy	$E_{vis} \geq 18.0$ GeV
Thrust axis	$\lvert\cos\theta_{thrust}\rvert \leq 0.71$
Number of tracks	$N_{ch} \geq 7$
Number of tracks with 2 VXD hits	$N_{Link} \geq 3$

Table 16: Hadronic event selection cuts

Events passing the cuts of the Pass 1 Z filter are reconstructed and processed by the pass 2 Z filter which has the same cuts as in Pass 1 which now acts on reconstructed quantities (see Table 14), and two additional cuts: $E_{imb} < 0.9$, and a cut to reject events that have fewer than two reconstructed jets.

4.3 Event Selection

The hadronic Z^0 event sample is constructed using events passed by the EIT filter. The selection cuts are shown in Table 16. The cuts are designed to find high charged multiplicity events with large energy deposition. Tracks are required to pass near the PV (z impact parameter < 5 cm) and have transverse momentum $p_t \geq 0.2$ GeV/c. The thrust axis cut contains the event within the barrel where the tracking is reliable. Visible energy is defined as the total energy of the charged tracks in the event. Plots of these quantities for data and Monte Carlo are shown before and after all the cuts have been applied (see Figures 24 and 25). One can see that the agreement is better after the cuts: beam-related backgrounds which are not well-modeled have been removed.

After applying these cuts to the 1993 data, 29400 events are selected. The non-hadronic background, which is predominantly $\tau^+\tau^-$, has been estimated to be $< 0.2\%$ [76] from the Monte Carlo. There are roughly equal proportions of uds, c, and b events in the sample and the subsequent analysis preferentially extracts b events.

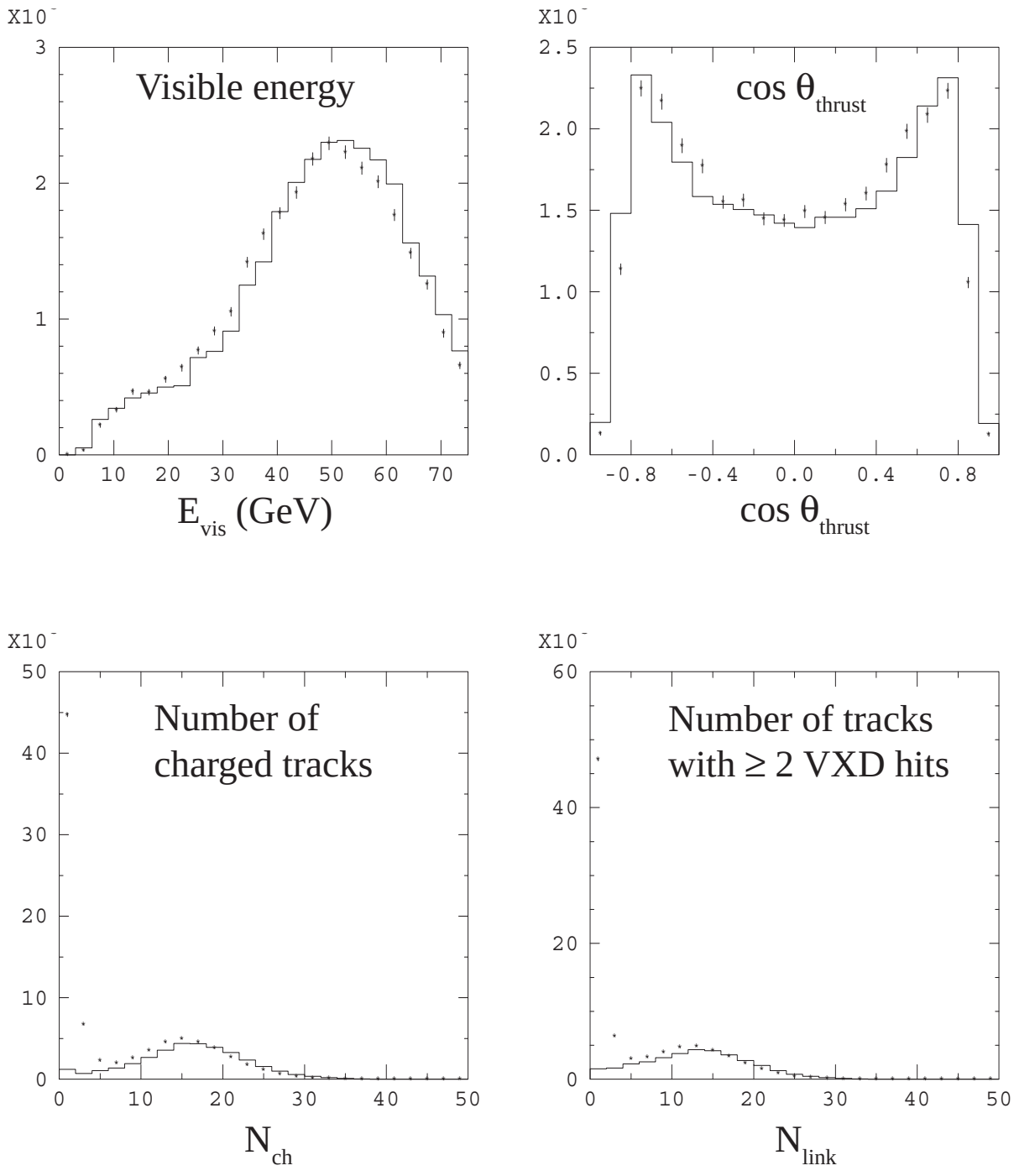

Figure 24: Comparison of data (points) and Monte Carlo (solid line) for event selection quantities before event selection

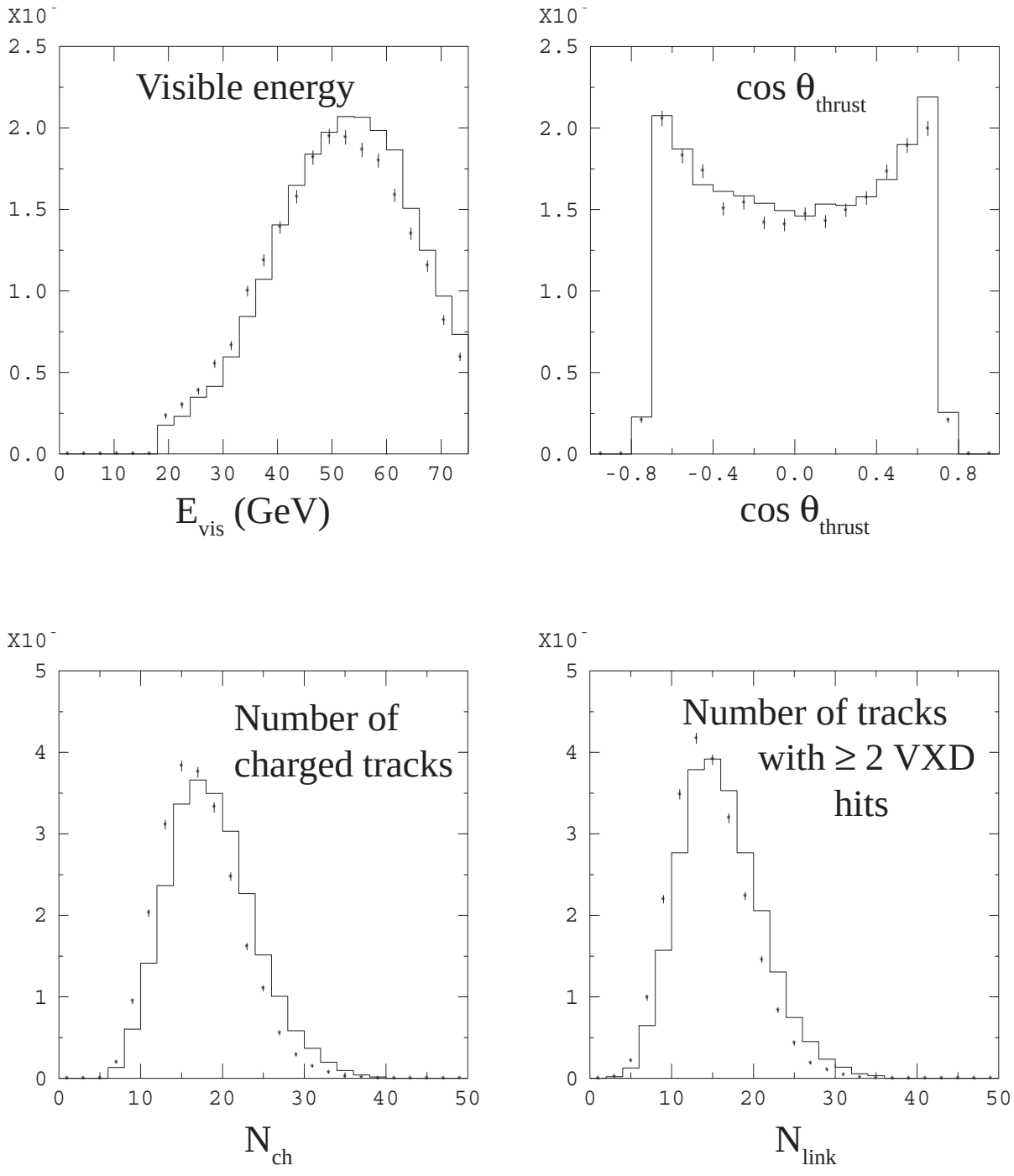

Figure 25: Comparison of data (points) and Monte Carlo (solid line) for event selection quantities after event selection

Chapter 5

Analysis

This measurement of the average B hadron lifetime takes advantage of the small beam spot and excellent vertex resolution available at SLD by using the CDC and VXD to reduce the data. The LAC is used only in event selection, as described in section 4.3.

This measurement of the average B hadron lifetime involves selecting vertices that are sensitive to the value of τ_B. The hadronic event sample described in section 4.3 is unbiased toward the quark flavor of the Z^0 decay, so one needs to construct an event sample that is predominantly $Z^0 \to b\bar{b}$ decays to reduce the background. This reduces the sensitivity of the analysis to the modeling of these backgrounds. $Z^0 \to b\bar{b}$ decays are selected at an early stage of the analysis by using an event tag to reduce the processing time required and to avoid the need for hard cuts at later stages.

The final sample is constructed from these tagged events in several steps. First, all possible vertices are constructed with the tracks in each tagged event, subject to very loose constraints. A set of independent vertices is extracted from this large set of vertices and a final sample is made by requiring one vertex per event hemisphere. The average B hadron lifetime is then obtained from a maximum likelihood analysis of these vertex positions in the data and the Monte Carlo. The final sample is quite large even with an event sample of modest size because of the inclusive nature of this measurement. The cuts in this measurement are comparatively loose, e.g. there is no high-p_T lepton requirement. However, the analysis is sensitive to the agreement

between the Monte Carlo simulation and the data, which needs to be investigated thoroughly for a full comprehension of the sources of systematic error.

5.1 Tagging $Z^0 \to b\bar{b}$ Decays

This analysis attempts to create an unbiased sample subject to very loose cuts. However, given the high tracking efficiency, a topological technique is easily swamped by backgrounds from random combinations of tracks. Events are tagged for use in this analysis in order to make this technique feasible with the computing power available.

Due to their long lifetimes and the large boost with which they are produced at SLD, B hadrons decay at a considerable distance from the IP (~ 2 mm on average). The large mass of the b quark means that the decay products of a B hadron will have high p_T on average. The tracks associated with these decays will on average miss the IP by a larger distance than other tracks in the event, and tracks in $udsc$ events. This characteristic of b events is used to tag them in this analysis. A description of this method first requires several quantities to be defined.

5.1.1 Jet Axis Determination

Jets are needed in this analysis to provide the approximate direction of the B hadron or b quark momentum in $Z^0 \to b\bar{b}$ decays. The jet axis is used to define whether a track that misses the IP is 'in front of' or 'behind' it, a property that is used in selecting $Z^0 \to b\bar{b}$ decays (as will be explained in the next section). The JADE [77] algorithm is used to construct these jets. This algorithm works by starting with a set of seed clusters, in this case charged tracks, which are assumed to be massless. A scaled invariant mass is calculated for every pair of clusters:

$$y_{ij} \equiv \frac{M_{ij}^2}{E_{vis}^2} = \frac{2E_iE_j\left(1-\cos\theta_{ij}\right)}{E_{vis}^2} \tag{154}$$

where E_{vis} is the total visible energy, in this case the total energy of the charged tracks, and E_i and E_j are the energies of clusters i and j. The pair with the smallest invariant mass is combined into a cluster k by summing their four-momenta. This

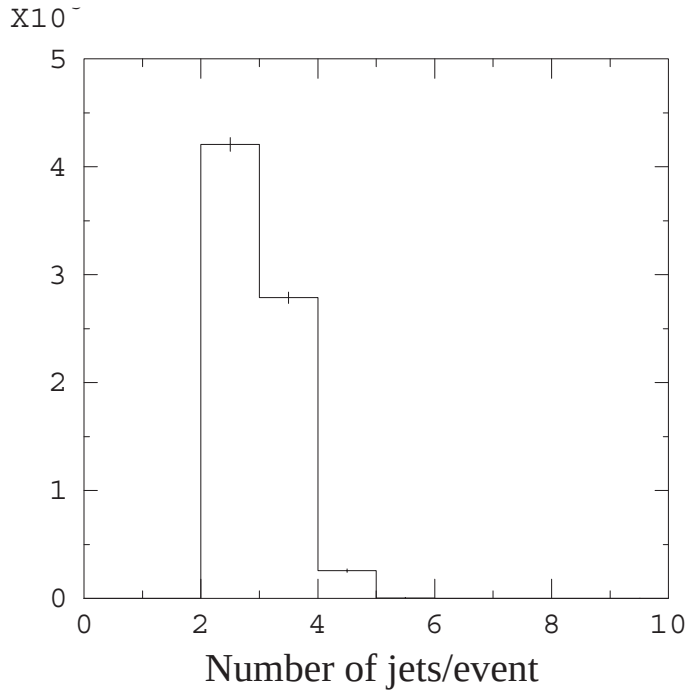

Figure 26: The number of jets per event in the hadronic event sample

process is iterated, reducing the number of clusters in the event, until all the scaled invariant masses are above a cutoff value y_{cut}. For this analysis, $y_{cut} = 0.02$, which gives ~ 2.5 jets per event on average in the hadronic sample as seen in Figure 26. This value of y_{cut} was chosen because it was found from the Monte Carlo to reproduce the B hadron direction most closely. This is turn made the jet axis more discriminating in tagging $Z^0 \rightarrow b\bar{b}$ decays. Figure 27 shows the distribution of the cosine of the angle between the jet axis and the B hadron momentum in b events for this y_{cut} as determined from the Monte Carlo; it can be seen that the directions are approximately equal within $\sim 12^\circ$.

5.1.2 The Signed Two-Dimensional Impact Parameter

The two-dimensional impact parameter b of a track is defined as the distance of closest approach in the xy (or $r\phi$) plane (i.e. the plane perpendicular to the beam axis) of the track to the IP (see Figure 28). The impact parameter is signed using a standard convention involving the axis of the jet that the track is assigned to. The sign effectively measures the sign of the decay length because it measures whether the

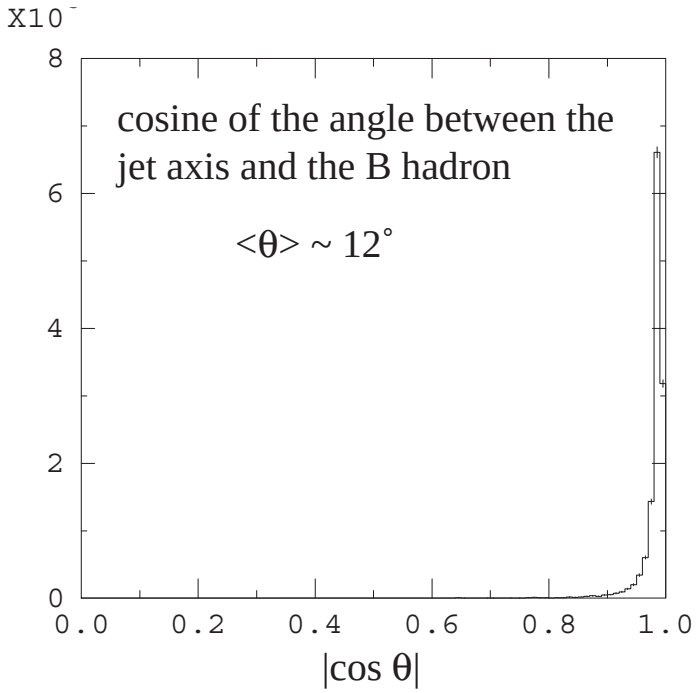

Figure 27: The angle between the b quark momentum and the nearest jet axis in $Z^0 \to b\bar{b}$ events

intersection of the track and the jet axis is in front of or behind the IP. Thus, if one draws a line from the point of closest approach (POCA) of the track to the IP, the sign of the impact parameter will be positive if the angle between this line and the jet axis is $< 90°$, otherwise it will be negative (see Figure 28). The impact parameter can be negative because of the detector resolution and differences between the true B hadron direction and the jet direction. Detector resolution will limit the precision of the measurement of the impact parameter, and for small impact parameters the smeared value can in fact be negative. The difference between the jet axis and the axis connecting the true B hadron to the IP means that a track with positive decay length can seem to come from behind the measured IP.

For tagging $Z^0 \to b\bar{b}$ decays, cuts are applied to remove badly measured tracks that would otherwise reduce the sensitivity of the impact parameter distribution to the quark species. Figure 29 compares the signed two-dimensional impact parameter distributions (after track cuts) for uds, c and b events as determined using the Monte Carlo. The distribution for b events is much wider reflecting the much higher b mass.

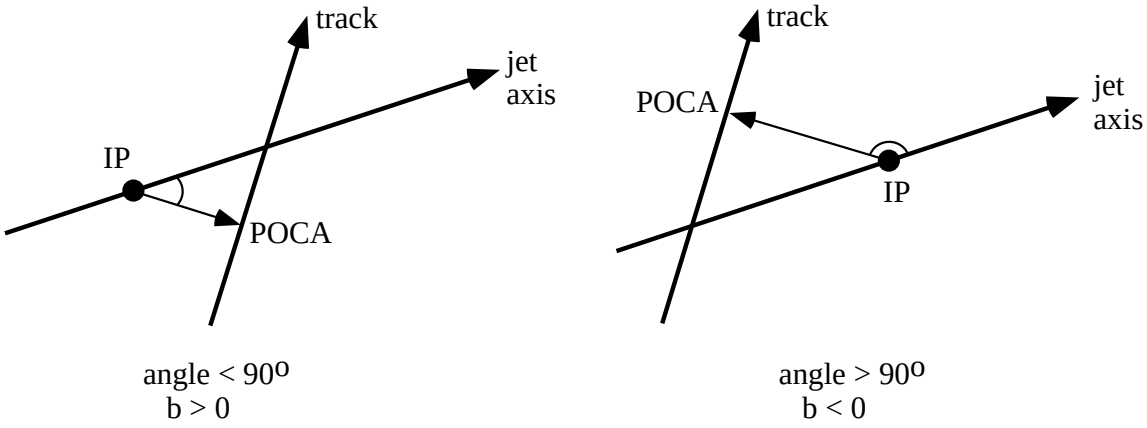

Figure 28: Assessing the sign of the 2-d impact parameter

This feature enables one to separate these events from the *udsc* background.

Further discrimination of b events is achieved using the normalized impact parameter which is defined as:

$$b_{norm} \equiv \frac{b}{\sigma_b}. \tag{155}$$

This quantity is used in tagging events for this analysis because it expresses how significantly a track misses the IP. Figure 30 shows the normalized 2-d impact parameter distributions for *uds*, c and b events using only the tracks passing selection cuts (described below).

5.1.3 Track Selection

The track reconstruction at SLD is designed to be very efficient with few checks on track quality, allowing one to choose how to make track selection cuts in one's own analysis. Poor quality tracks can be traced to three sources: a track can be mismeasured if there are insufficient numbers of CDC and VXD hits to provide a good fit; a track can interact with the materials of the detector and reconstruct less well; and a track can also originate from the decay of long-lived neutral particles, e.g. K^0 and Λ^0. These tracks can have large impact parameters and can therefore be mistaken for tracks associated with a b decay. They are removed, where possible, leaving a set of "quality" tracks that is more useful in discriminating between b events

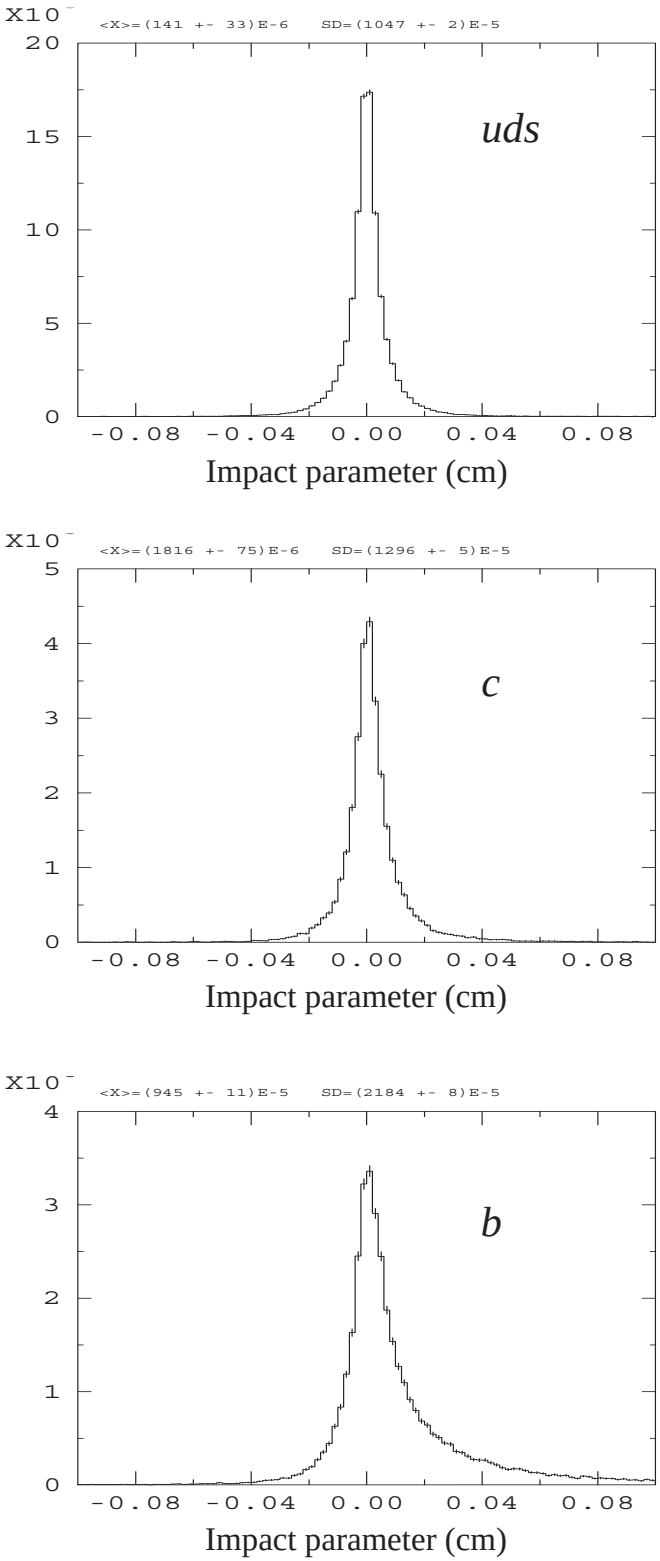

Figure 29: The 2-d impact parameter distributions for uds, c and b events

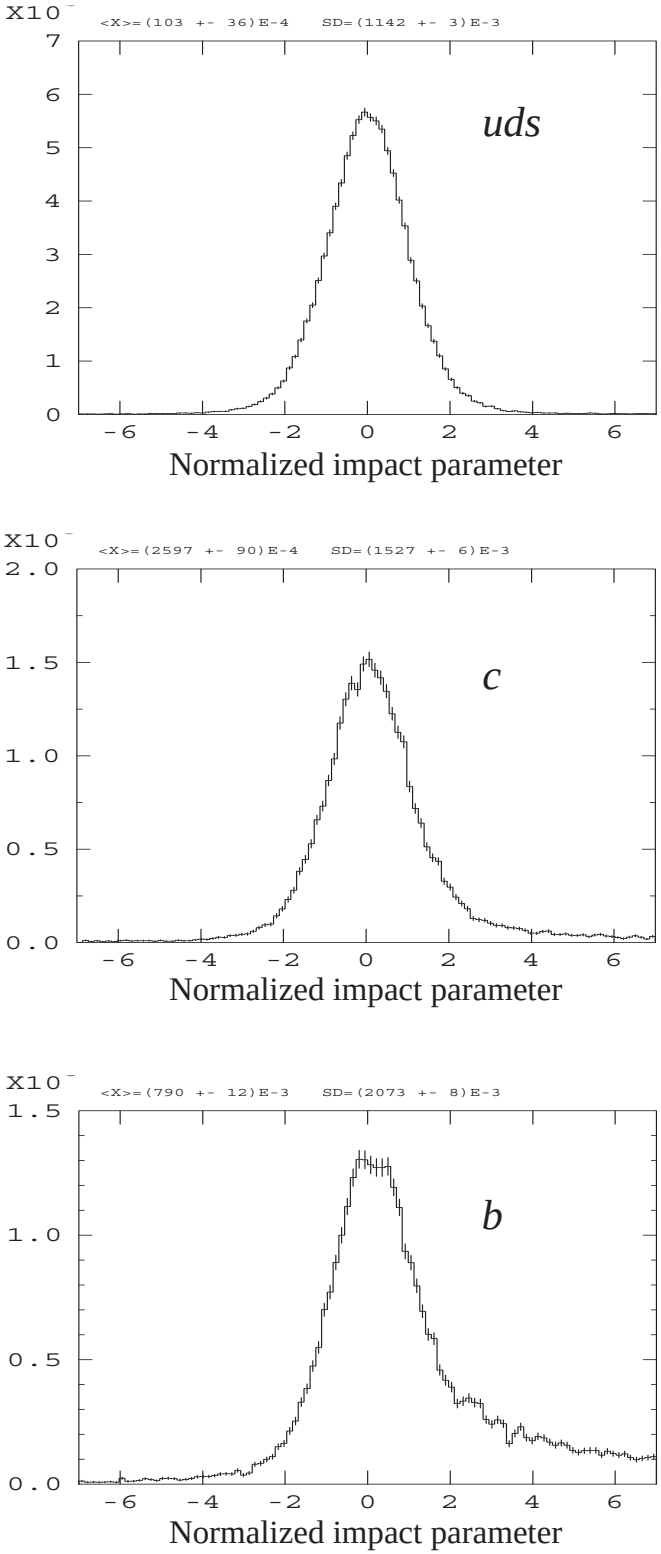

Figure 30: The signed 2-d normalized impact parameter distribution for *uds*, *c* and *b* events

Quantity	Cut range
starting radius, r_{CDC}	< 39.0 cm
number of CDC hits	> 40
number of associated VXD hits	≥ 1
$\chi^2/d.o.f.$ of CDC track fit	< 5
$\chi^2/d.o.f.$ of combined CDC & VXD track fit	< 5
xy impact parameter, $\|b\|$	< 0.3 cm
xy impact parameter error, σ_b	< 250 μm
xy impact parameter of CDC track, $\|b_{CDC}\|$	< 1.0 cm
z at POCA	< 1.5 cm
acceptance, $\|\cos\theta\|$	< 0.80
momentum, p_{xy}	> 0.40 GeV/c
track inconsistent with Λ^0 and K^0_S decay and γ conversion	remove V^0s

Table 17: "Quality" cuts used to select tracks for tagging and vertexing

and *udsc* events when using the impact parameter tag described here. There is less dependence on modeling of the *uds* and *c* backgrounds, and thus Monte Carlo and data match better. The track selection cuts are shown in Table 17 and distributions of the quantities that are cut on are shown in Figures 31, 32, and 33. The main effect of these cuts is to select well-measured tracks that extrapolate to the region near the IP, i.e. they are inconsistent with long-lived particles. Tracks from Λ^0 and K^0_s decays and γ conversions are identified by looking at all pairs of oppositely charged tracks that form vertices (V^0s). In the first two cases, if a vertex is displaced from the IP and has a mass consistent with either Λ^0 or K^0_s, its tracks are removed. In the case of γ conversions, tracks are removed if the mass of the vertex is consistent with zero when the tracks are assigned the mass of the electron.

If the Monte Carlo is well-tuned to the data, these selection cuts should work with equal efficiency on tracks in both cases. However, in the case of this analysis, a larger fraction of tracks in the Monte Carlo passes the cuts compared to the data. This is in part due to over-optimistic estimates in the Monte Carlo of the CDC hit efficiency and resolution as a function of position within a CDC cell [53]. An *ad hoc* series of corrections is applied to the tracks in the Monte Carlo to make the fraction of tracks passing the selection cuts equal to that in the data. The ratio between the Monte Carlo and data of the fraction of CDC tracks passing the cuts is tabulated

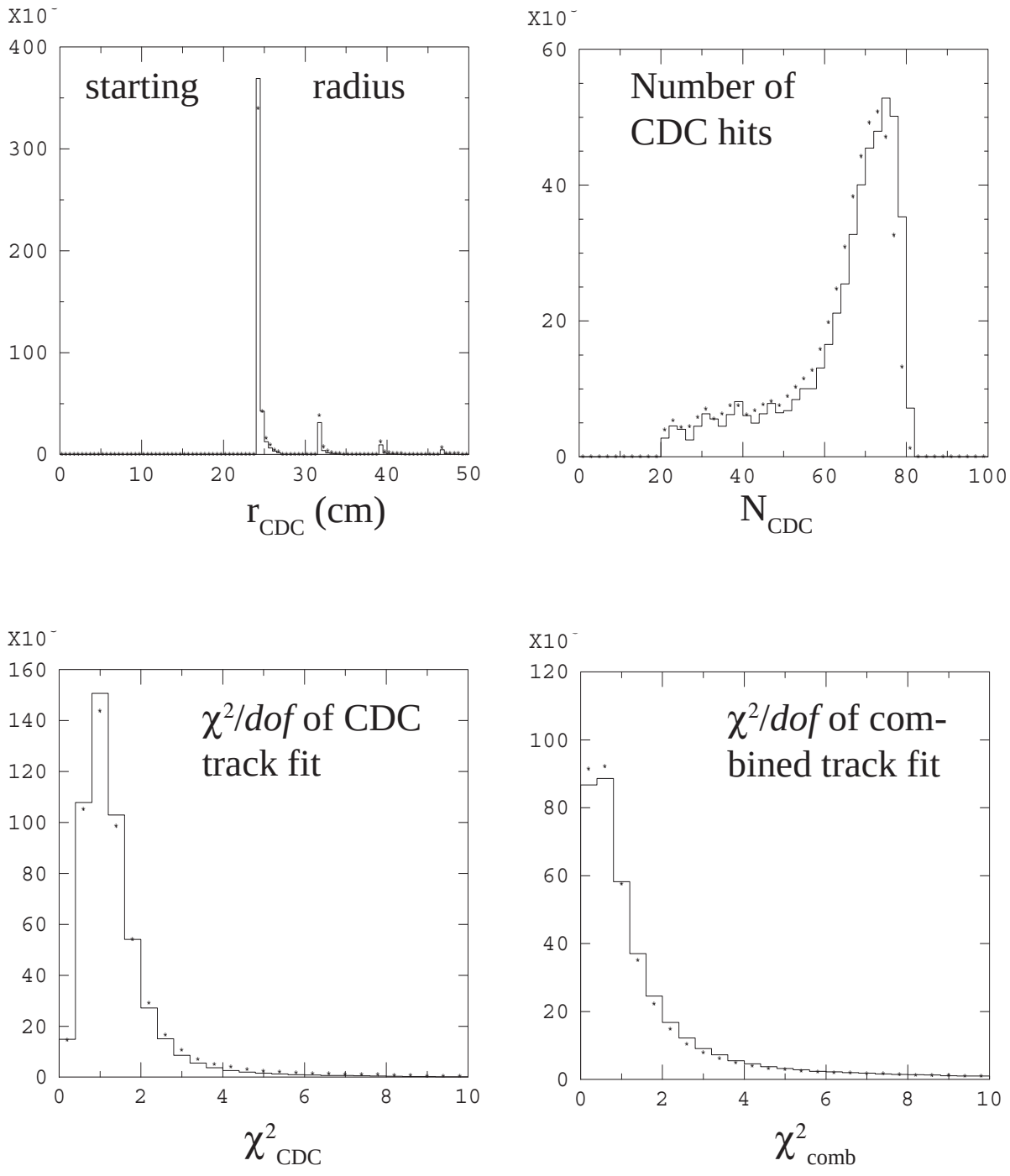

Figure 31: Distributions of the track selection quantities. MC (solid line) and data (points)

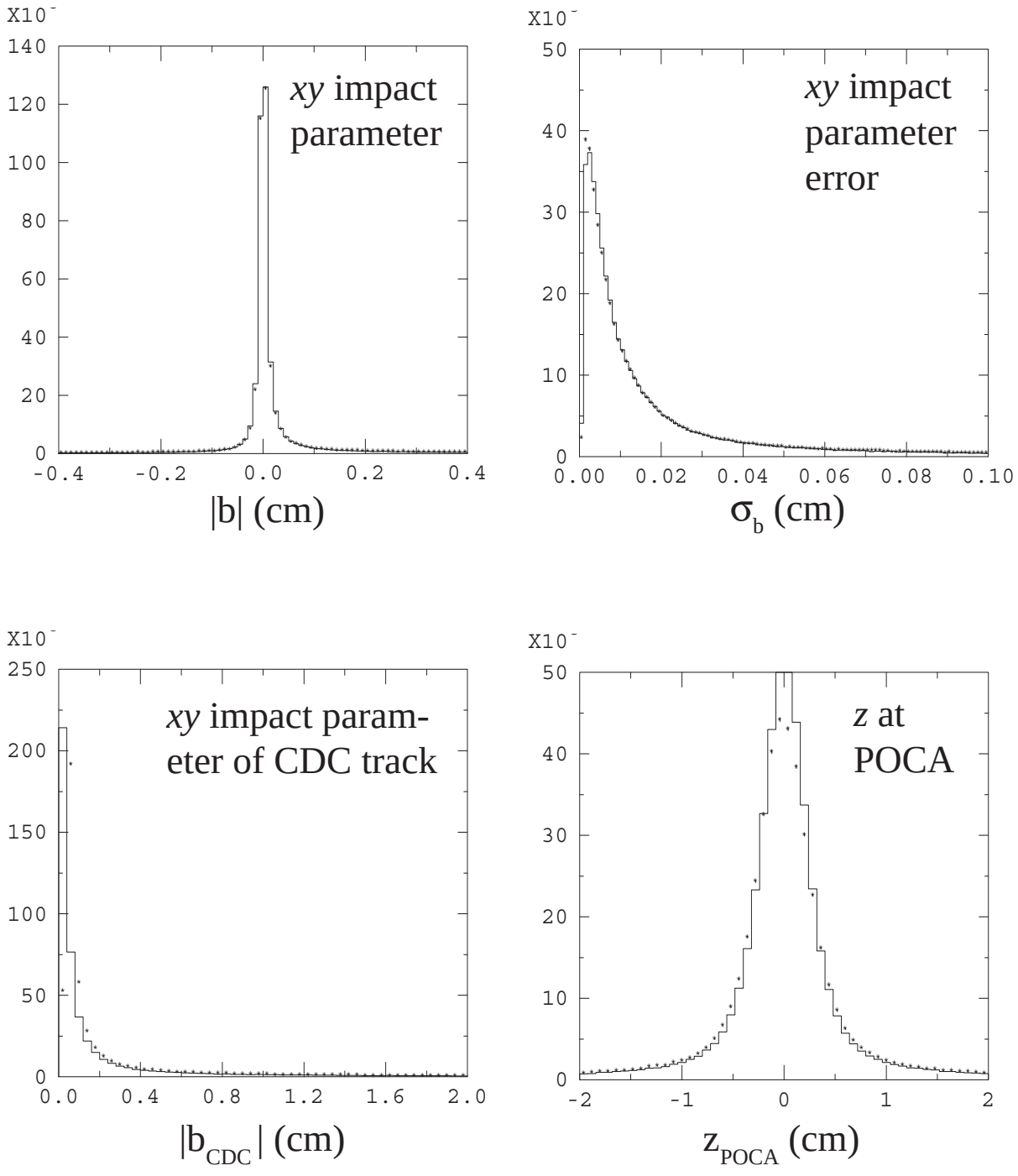

Figure 32: Distributions of the track selection quantities (cont.) MC (solid line) and data (points)

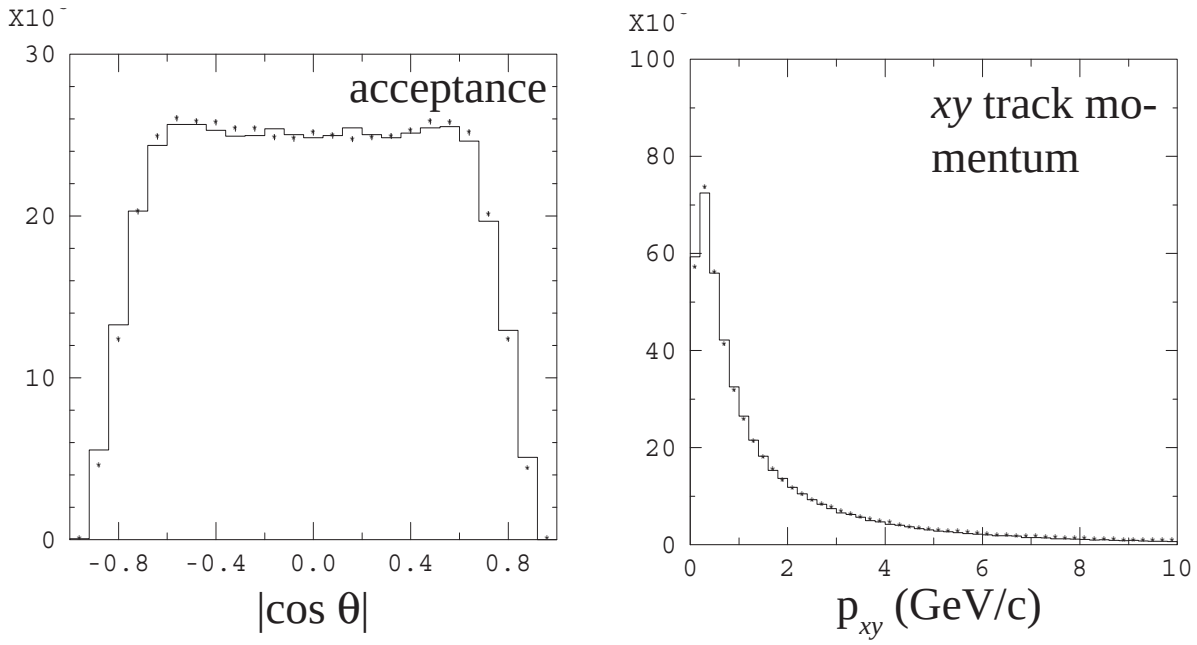

Figure 33: Distributions of the track selection quantities (cont.) MC (solid line) and data (points)

as a function of $p_\perp$, $\cos\theta$, ϕ and $\theta_{\rm jet}$. The fraction of CDC tracks classified as good in the Monte Carlo is reduced to match that in the data by systematically removing tracks as a function of these quantities. The fraction of good CDC tracks that can be linked to VXD hits is then adjusted in the Monte Carlo by removing tracks as a function of p, $\cos\theta$, and ϕ. Though the corrections are due to variations in hit efficiency within a CDC cell, they do not vary much with the parameters mentioned above. The staggered CDC geometry described in chapter 2 reduces the spatial (θ,ϕ) variation of the efficiency corrections. The fraction of tracks removed by these corrections is $\sim$ 6%. When the entire 1993 run period is considered, the tracking efficiency corrections are able to make the fraction of tracks in the data and MC that pass quality cuts agree within $\sim$ 0.3 tracks of each other. The effect that the tracking efficiency corrections and the remaining discrepancy between Monte Carlo and data have on the determination of the lifetime will be discussed as a source of systematic error in the following chapter.

quark flavor	purity (%)	efficiency (%)
uds	0.9	0.2
c	9.0	7.5
b	90	60

Table 18: Tagging efficiency and purity for different quark flavors

5.1.4 The Tagged Sample

Events are tagged by requiring an event to have a minimum number of "quality" tracks above a certain normalized impact parameter (or significance). The efficiency ϵ_b and purity Π_b of the tagged sample are defined as follows:

$$\Pi_q \equiv \frac{\text{Number of } Z^0 \to q\bar{q} \text{ events after tagging}}{\text{Total number of events after tagging}} \tag{156}$$

$$\epsilon_q \equiv \frac{\text{Number of } Z^0 \to q\bar{q} \text{ events after tagging}}{\text{Number of } Z^0 \to q\bar{q} \text{ events before tagging}} \tag{157}$$

The choice of tagging parameters for this analysis is

- a significant track has $\frac{b}{\sigma_b} \geq 3.0$
- a tagged event has 3 significant tracks

which gives a purity Π_b of 60% and an efficiency ϵ_b of 90%. These values are chosen as they give the best balance between statistics and uncertainties in the Monte Carlo modeling that might arise from using a less pure sample. Figure 34 shows the relationship between efficiency and purity for different levels of significance and numbers of significant tracks required by the tag. Consecutive points on each curve are separated by steps of 1 significant track. Table 18 lists the purities and efficiencies of events of different quark flavors after tagging. The main background is from c events due to the long lifetimes of charmed hadrons.

The efficiencies and purities are dependent on the accuracy of the Monte Carlo modeling. For example, if the value of τ_B in the data is different from the one in the Monte Carlo, the shapes of their impact parameter distributions for b events will not match. The proportion of b and $udsc$ events passing the tag will not be the same in the Monte Carlo and data, so the purity and efficiency of our sample as determined

from the Monte Carlo will not be correct. However, the uncertainty in τ_B is not large and so this effect is not as large as might be expected. In addition, later cuts in the analysis reduce the sensitivity of the result to this effect. This will be discussed further in the following chapter.

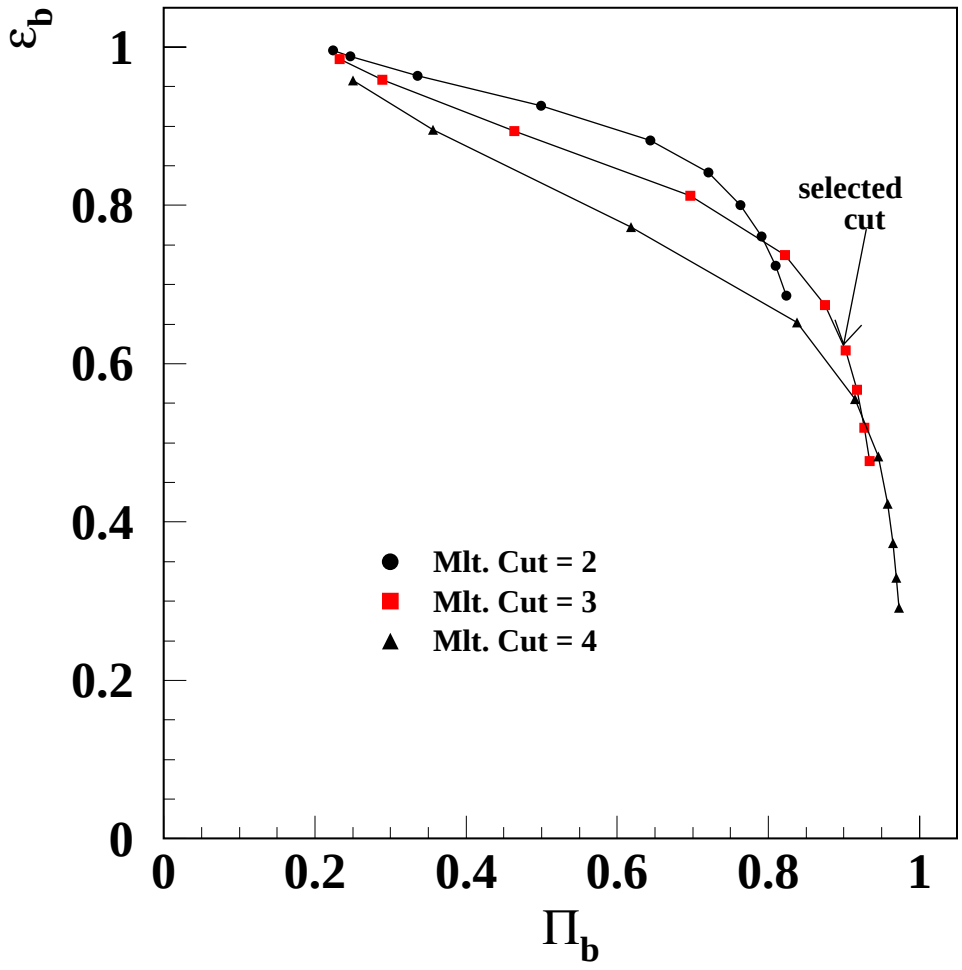

Figure 34: Efficiency vs. purity as a function of tagging parameters. Mlt.cut is the cut on the number of significant tracks required to tag the event.

An alternate tag is employed as a systematic check of tagging biases in the analysis. A hemisphere is tagged as follows

- a significant track has $\frac{b}{\sigma_b} \geq 3.0$

- a tagged hemisphere has 3 significant tracks in a jet opposite that hemisphere.

By tagging the hemisphere opposite the one used by the analysis, one reduces biases that the tag has towards long-lived B events. The statistics are obviously much lower and this tag is not used for the quoted result.

5.2 Vertex Construction

The goal of this analysis is to initially create vertices using a very general selection process that does not bias the composition of the sample towards specific combinations of tracks or event topologies (as much as is possible). In this way a nearly complete set of vertices can be constructed for each event, where a vertex is defined as a common point that can be assigned to tracks that intersect or nearly intersect. Because of constraints on processing time and memory, limits on the complexity of an event are necessary. This means that very occasionally not all vertices in the event can be constructed and analyzed. In this measurement, events are rejected if they have more than 200 vertices.

The vertices, which are not all independent of each other, are sorted into independent sets, of which one is chosen. One vertex per hemisphere from the chosen set is used in the lifetime measurement. This analysis does not attempt to specifically reconstruct the B hadron decay vertex by using high p_T leptons or otherwise. By extracting candidate vertices that have at least one track linked to the decay of a B hadron, a large sample can be collected from an event sample of modest size. The major background that needs to be reduced is tracks that come from the IP. Often, these tracks can also be consistent with secondary vertices, and can increase the dependence of the analysis on the modeling of these tracks, i.e. the fragmentation model, while decreasing its sensitivity to τ_B. Because these vertices are not reconstructed B decay vertices, one cannot cut on invariant mass while retaining the statistical power of this method. The power of this method resides in preserving as many candidates with sensitivity to τ_B as possible.

The initial vertex construction uses a standard vertexing package called ZXFIND which is very efficient at finding all the vertices in an event. Consequently many

vertices are constructed from chance combinations of tracks in the event. Some vertices have at least one track associated with the decay vertices of interest: secondary vertices from the decay of B hadrons. The task is to choose vertices in the event that are most useful for measuring the B hadron lifetime. Thus, ZXFIND may not construct the true B hadron decay vertex nor will it necessarily be chosen by the analysis that follows if the goodness of fit of another set of vertices is better (as will be explained below).

The process by which ZXFIND constructs vertices is as follows. By default, ZXFIND uses most of the tracks in an event. However, as described in section 5.1.3, there are low quality tracks from various sources that will create vertices that are not associated with the secondary decay vertices in the event. To limit this contamination of the sample, only "quality" tracks are used to construct vertices for this analysis. In order to simplify the topology of the event, vertices are rejected if they are closer than 1 mm to the IP. The motivation for this cut is that it significantly reduces the possible combinations of tracks, and thus the processing time and memory needed as well as reduce background. The effect of this cut is to remove vertices containing at least one track that can be associated with the IP (normalized 2-d impact parameter $b/\sigma_b < 2.5$). Vertices are also required to have at least one track that is inconsistent with the IP ($b/\sigma_b > 2.5$) and all tracks must have $p > 1$ GeV/c. These cuts reduce the background from combinatorics, mismeasured tracks, and tracks from the IP and primary charm decays. The cut on track momentum has been tuned to reduce the number of events that are later rejected by the limit on the number of vertices per event (which has the capability of biasing the sample if one is not careful). However, the momentum cut does not have a strong effect on the composition of the vertices in the final sample.

Vertices are constructed by fitting a common point to the region of closest approach of a set of tracks. Only the tracks in a particular event hemisphere can contribute to vertices in that hemisphere. The χ^2-probability of the vertex fit is required to be greater than 5%. Two-prong vertices are constructed out of all pairs of tracks that pass within 3 σ of a common point, where σ is the uncertainty in the fitted vertex position. Three-prong vertices are constructed out of all pairs of two-prong

track quality	passes "quality" cuts
decay length cut	$d > 1$ mm
impact parameter	$b/\sigma_b > 2.5$ for ≥ 1 track
track momentum	$p > 1$ GeV/c
fit probability	$> 5\%$
DOCA to vertex	$< 3\sigma$

Table 19: Requirements for constructing initial vertex sample

vertices that share a track, such that all tracks are within 3 σ of the new vertex position. Four-prong vertices are constructed out of combinations of two- and three-prong vertices such that all tracks are within 3 σ of a common point. Vertices with higher numbers of prongs are not constructed. It must be emphasized that three- and four-prong vertices are constructed in addition to the particular two-prong vertices that they are constructed from, and do not replace them in the vertex sample. Thus each track can be (and usually is) assigned to more than one vertex and the vertex sample is composed of vertices that share tracks between them. The vertex multiplicity is consequently quite high just from combinatorics, as shown in Figure 35. There are 6.5 vertices per hemisphere on average. It is interesting to note that the structure in the distribution can be explained by combinatorics. For example, the peak near 17 vertices per event is due to a 4-prong vertex and all its constituent 3-prong vertices and all their constituent 2-prong vertices being constructed:

$$N_{vtx} = 1 \times \text{four-prong} + 4 \times \text{three-prong} + 4 \times 3 \times \text{two-prong} = 17 \qquad (158)$$

This suggests that the method is efficient at constructing vertices from the tracks in the sample. From Figure 36, which shows the number of prongs per vertex, it can be seen that two-prong vertices predominate as expected from combinatorics, and very few five-prong vertices would have been expected if they had also been constructed. The data and the Monte Carlo match well in these two plots.

In every tagged event, an initial vertex sample is constructed out of all possible geometric vertices that pass the cuts just described. As a result, 97.8% of events have at least one vertex. In the 1993 run, 2 events are rejected by the 200 vertex limit. A study shows that these events would also have been rejected by a later cut on the number of partitions, as explained in the following section.

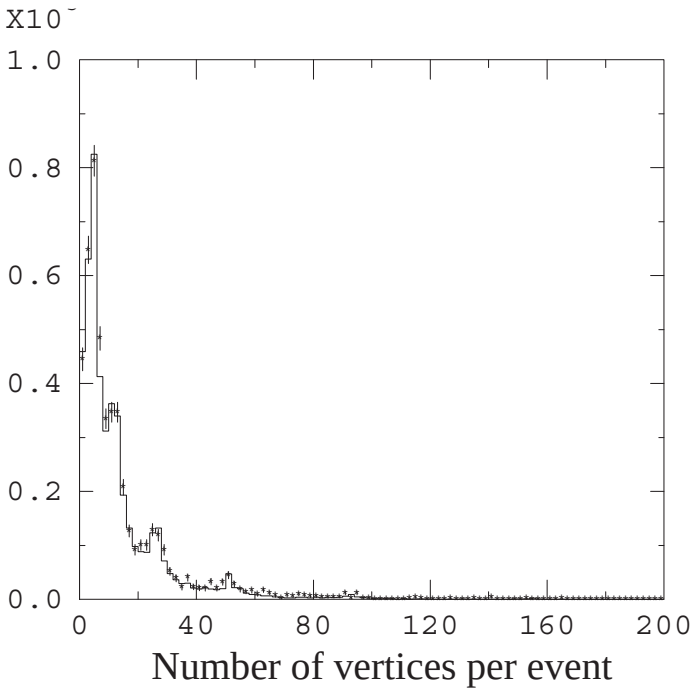

Figure 35: The number of vertices per event – MC (solid line) and data (points)

In the Monte Carlo sample, vertices are classified according to the origins of their tracks, as shown in the following list:

b	the weak decay of a B hadron
cascade c	the weak decay of a hadron containing a cascade c quark
b + **cascade** c	the weak decays of a B hadron and a hadron containing a cascade c quark
b + **other**	the weak decay of a B hadron and another source
cascade c + **other**	the weak decay of a hadron containing a cascade c quark and another source
primary c	the weak decay of a charm hadron in a $Z^0 \to c\bar{c}$ decay
IP	IP tracks only
other	combinations not covered above

This categorization is chosen so that the cuts can be tuned to reduce the contribution of vertex classes that are less desirable, e.g. **IP** vertices, in the final sample. The first five categories are the most sensitive to the B hadron lifetime and are described in

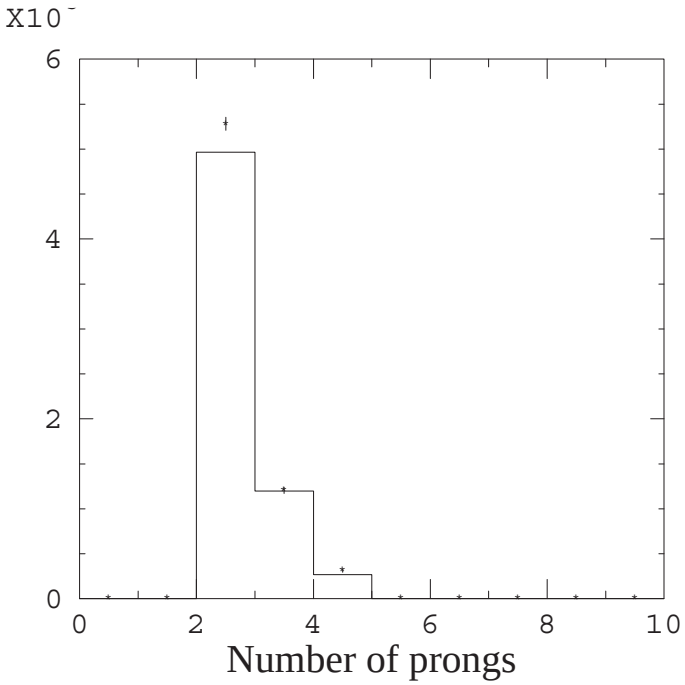

Figure 36: The number of prongs per vertex – MC (solid line) and data (points)

this analysis as containing 'B lifetime information'. The shape of the vertex decay length distribution of vertices with IP tracks does not depend on τ_B and the cuts that are applied, in particular the decay length cut of 1 mm, try to remove predominantly this component. Smaller cuts on the vertex-IP distance result in much higher vertex multiplicities and a smaller fraction of vertices with B lifetime information. The contribution of primary charm vertices is also reduced by a 1 mm cut.

Table 20 shows the vertex composition at this stage of the analysis as determined from the Monte Carlo. The contribution from IP-related vertices is already quite low at this stage of the analysis as expected from the minimum vertex-IP distance requirement of 1 mm.

5.3 Partitioning

The cuts in the initial stage of vertex construction are very loose, as described in the previous section, and all possible combinations of tracks that pass these cuts are considered to be vertices. These vertices are not independent of each other as a

vertex type	composition (%)
b	19
cascade c	14
b + cascade c	48
b + other	9
cascade c + other	5
primary c	3
IP	0.5
other	2

Table 20: Vertex composition of initial vertex sample

track can belong to several vertices (see Figure 37). The next stage of the analysis, called partitioning, creates subsets or partitions of these vertices in which each track is uniquely assigned to a vertex, as shown in Figure 38. The separation of the event into hemispheres for the vertex construction simplifies this task as the vertices can be partitioned by hemisphere. Nevertheless, each hemisphere can be partitioned in several ways. In each event, every possible unique assignment of tracks to vertices is constructed. As this is a pattern recognition problem, it requires a large amount of processing power. Limitations of memory and CPU time require events to be rejected if the number of partitions in the event as a whole (the product of the number of partitions in each hemisphere) or in a single hemisphere exceeds 1000. Events are also rejected if a track is shared by more than 60 vertices. These limits remove 1% of tagged events as shown in Table 21. The 200 vertex limit that is applied before partitioning is superseded by the cut on the number of partitions: the two events in the data that are are cut by this limit would have been cut by the partition limits. Thus, the cut is unnecessary but does help reduce the processing time required which is an important consideration in this analysis. The effect of all these limits is small and will be discussed in the next chapter.

A single partition is selected from an average of 28 partitions in an event hemisphere. The partition is chosen using the quantity M, similar to a joint probability, which is defined as

$$M = \prod_{\text{all vertices}} P(\chi^2, d.o.f.) \tag{159}$$

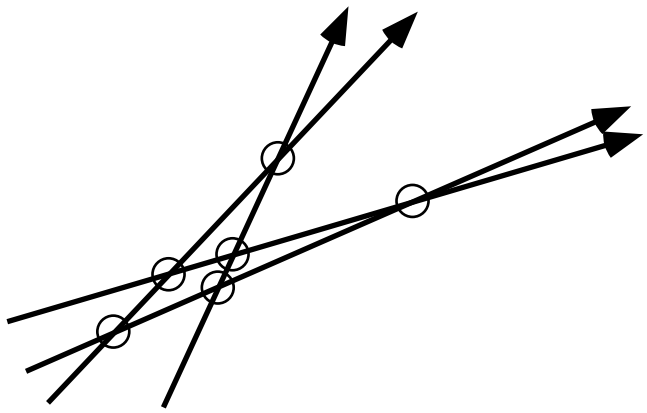

Figure 37: Tracks are shared between vertices in the initial sample

number tagged	> 1000 partitions in event	> 1000 partitions in hemisphere	> 60 vertices shared by 1 track	> 200 vertices in event
4299	41	7	3	2

Table 21: Events rejected by limits on the number of vertices, partitions and track sharing

where $P(\chi^2, d.o.f.)$ represents the vertex fit probability and the product includes all the vertices in a given partition. The partition selection criterion is chosen to provide low backgrounds and a high efficiency for finding vertices with B lifetime information. In the spirit of the rest of the analysis, the best partition does not necessarily contain the true B hadron decay vertex, even if this is fully reconstructed, because the fit probability of all the vertices in the partition determines the choice of the best partition. The joint probability distribution for data and Monte Carlo is shown in Figure 39.

The vertices in each selected partition then pass the following cuts which are tuned to remove vertices with tracks from the IP.

- angle between the vertex line-of-flight and the nearest jet axis, $\theta_{vtx-jet} > 150$ mrad
- transverse momentum of tracks relative to vertex line-of-flight $p_T > 0.07$ GeV/c

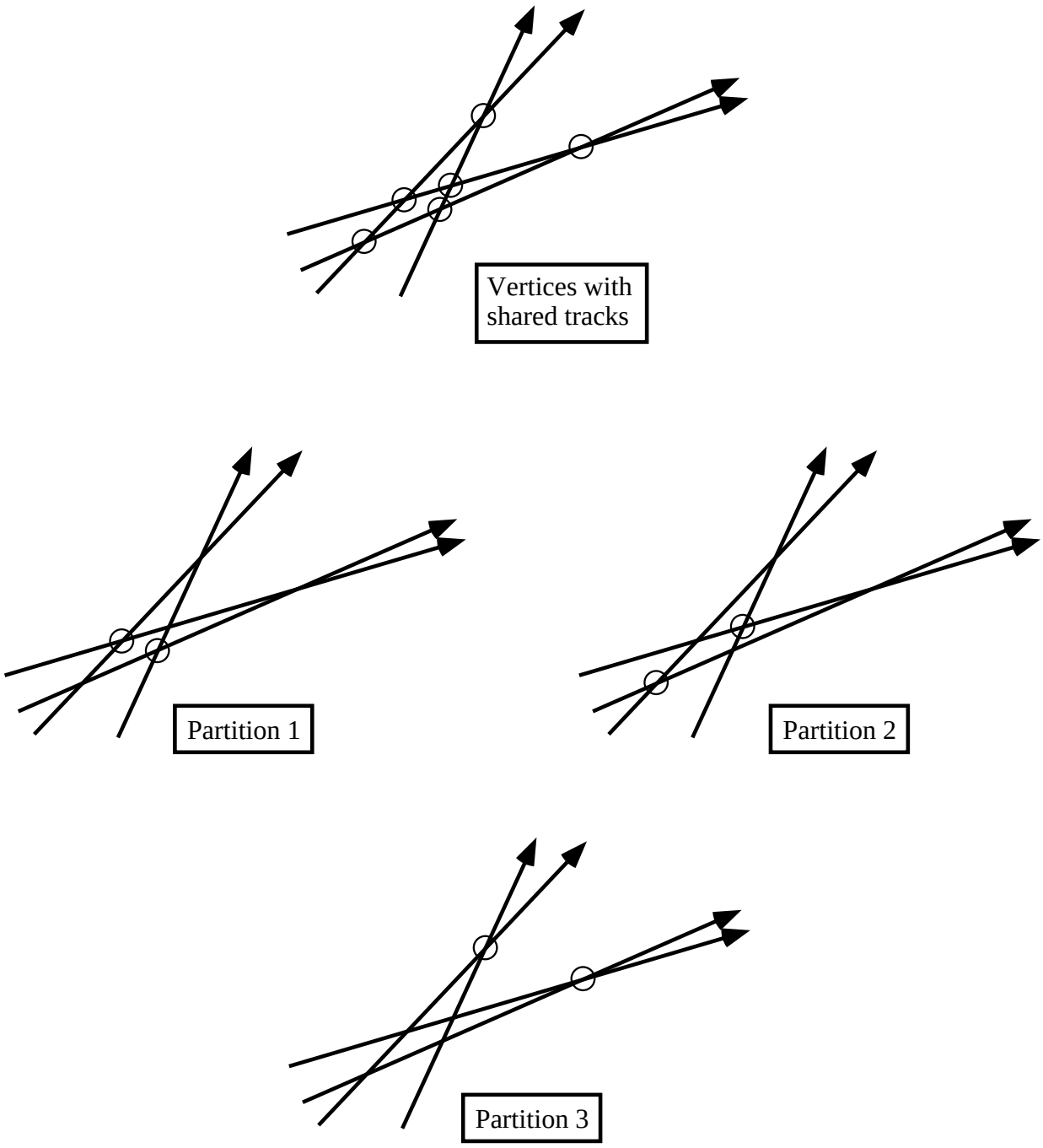

Figure 38: Partitioning: uniquely assigning tracks to vertices

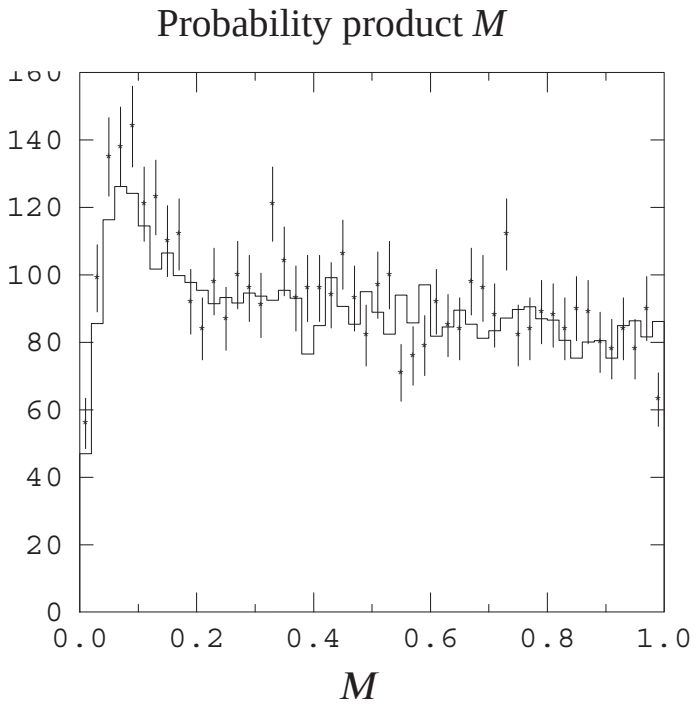

Figure 39: The probability product (M) distribution – MC (solid line) and data (points)

After these cuts, the vertex composition is as shown in Table 22. The percentage of vertices with B lifetime information is 91% which is lower than before partitioning (see Table 20), but the vertices are now independent of each other and the vertex multiplicity is much reduced. There are a total of 5856 vertices (0.69 vertices per hemisphere on average) at this stage of the analysis. Figures 40 and 41 show various track and vertex quantities for both data and Monte Carlo. The agreement between the two is good which is a good demonstration of the reliability of this method for a lifetime measurement. It is in these quantities that one might expect to see discrepancies if, for example, heavy quark fragmentation were incorrectly modeled.

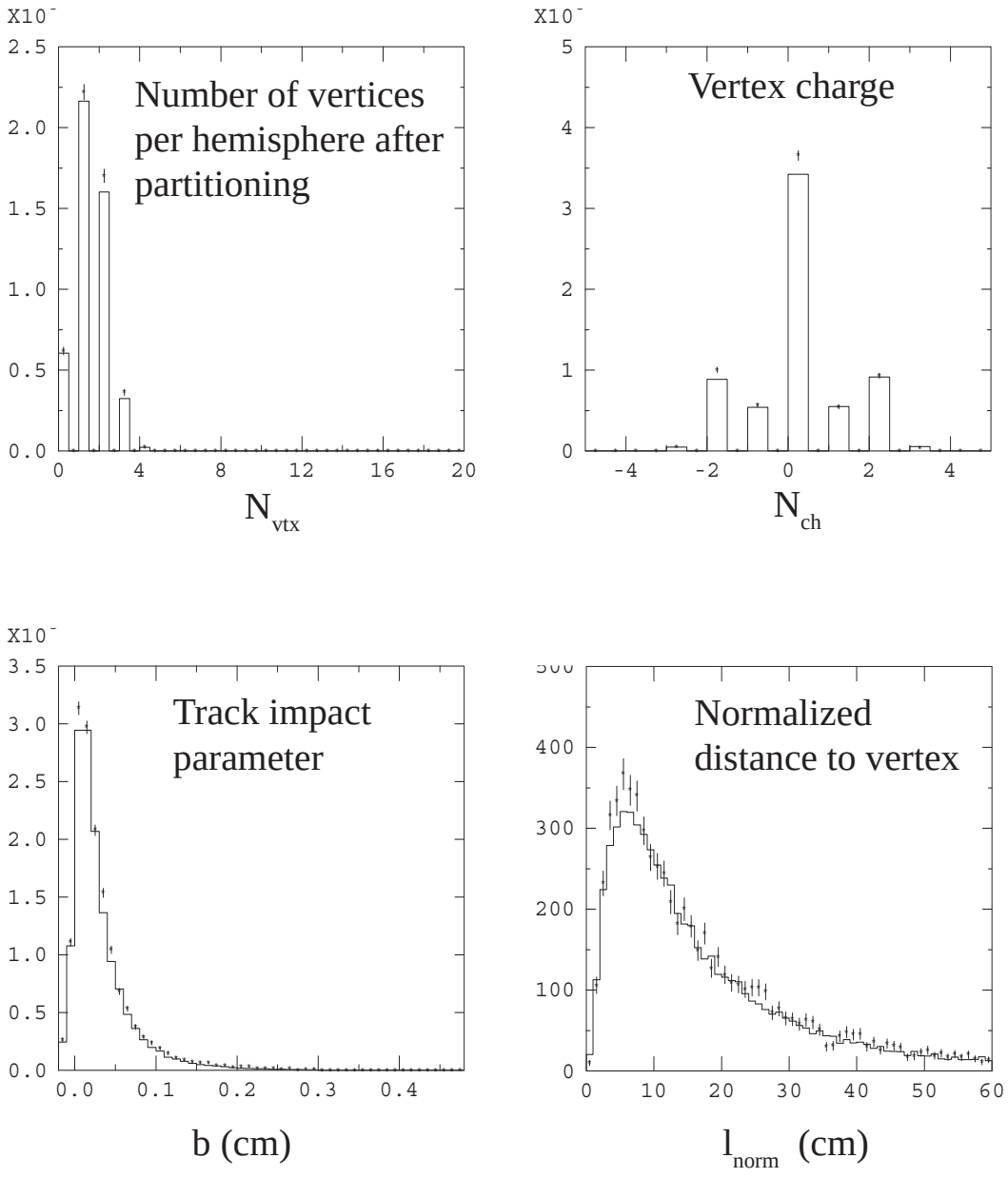

Figure 40: Comparison of MC (solid line) and data (points) for the following distributions after selection of the best partition (a) the number of vertices/hemisphere, (b) vertex charge, (c) track impact parameter, (d) normalized vertex distance

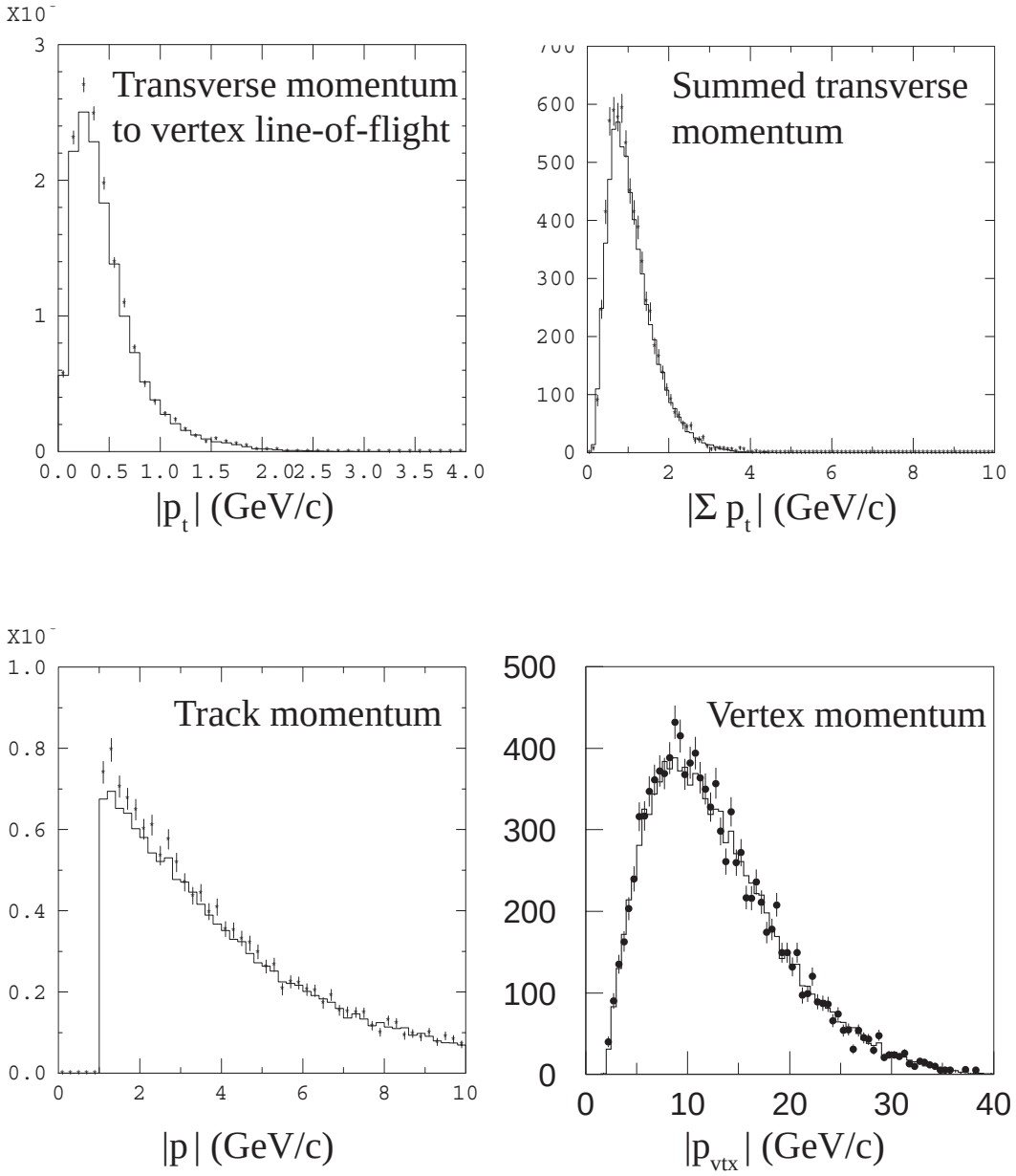

Figure 41: Comparison of MC (solid line) and data (points) for the following distributions after selection of the best partition (a) transverse momentum to vertex line-of-flight, (b) summed transverse momentum, (c) track momentum, (d) total vertex momentum

vertex type	composition (%)
b	21
cascade c	24
b + cascade c	35
b + other	5
cascade c + other	6
primary c	5
IP	1.3
other	3

Table 22: Vertex composition of vertex sample after selection of the best partition

5.4 The Final Sample

A maximum of one vertex per hemisphere is chosen for the final sample to avoid multiple counting. In hemispheres with more than one vertex in the best partition, the vertex closest to the IP is chosen. The choice of vertex has only a small effect on the measured lifetime, as will be discussed in the following chapter. One chooses the closest vertex because, after the 1 mm cut, this can be expected to be closer to the B vertex, and thus contain more tracks with sensitivity to τ_B. In the final sample, 60% of hemispheres in the 4299 tagged events have a selected vertex. The vertex composition of the final sample is shown in Table 23. The percentage of vertices with B lifetime information is 92%. The contribution from **IP** vertices is much less than after partitioning. The contribution of b + **other** and **cascade** c + **other** is small in the final sample. This is desirable as the modeling of these vertices is less accurate than pure b or **cascade** c vertices. The largest contribution comes from the b + **cascade** c category.

As this is a measurement of the average B hadron lifetime, it is important to know whether the process of producing the final sample changes the relative abundances of each B hadron species. In particular, the proportion of B baryons, which have a shorter lifetime [42] than B mesons, needs to be known. The very similar lifetimes expected for the different B mesons [33, 34, 35, 36, 37, 38, 39, 40, 41, 42, 43, 44] suggests that their abundances with respect to each other should not change much. Knowing these abundances allows this lifetime result to be compared to other measurements

vertex type	composition (%)
b	23
cascade c	26
b + cascade c	37
b + other	3
cascade c + other	3
primary c	6
IP	0.4
other	2

Table 23: Vertex composition of final vertex sample

B hadron species	abundance in generated Monte Carlo	abundance in final sample
B baryon	8.9	7.6
B_u	39.7	40.1
B_d	39.6	40.7
B_s	11.8	11.5

Table 24: Abundance of B hadron species before and after analysis

of τ_B. Table 24 lists these fractions before the analysis and after selection of the final sample. The sensitivity to the B baryon fraction is assessed in the following chapter.

5.5 Measurement of the Average B Hadron Lifetime

The average B hadron lifetime is extracted from the distribution of the vertex-IP distance (referred to as decay length) in the final sample using the method of maximum likelihood. The decay length distribution for the final sample of the data is shown in Figure 42. The Monte Carlo is composed of two sets of events generated with different values of τ_B, as described in section 3.1. In principle, one can generate many sets of Monte Carlo events with different values of τ_B and find the sample that best reproduces the data to determine the value of τ_B in the data. This is not really practicable because huge amounts of time are required to carry this out, and a

reweighting procedure is used instead.

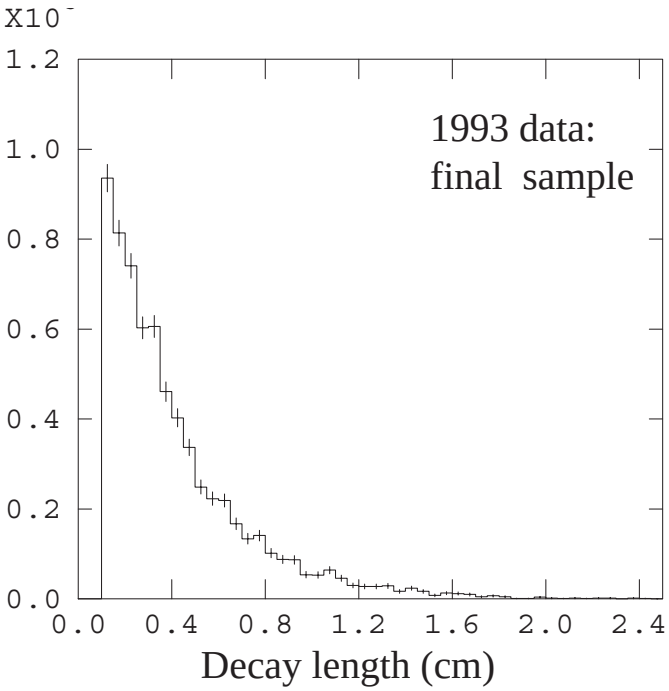

Figure 42: The decay length distribution for the final sample of vertices in the 1993 data set.

The vertices in the Monte Carlo final sample are sorted into 3 categories: primary charm, b-related and fakes. Primary charm vertices are vertices from the final sample in a $Z^0 \rightarrow c\bar{c}$ event that contain at least one track from the weak decay of the c quark. b-related vertices are vertices from the final sample in a $Z^0 \rightarrow b\bar{b}$ event that contain at least one track from the weak decay of the b quark or the cascade c quark. Fakes are all other vertices, i.e. vertices from uds events, and vertices from b events that do not contain a b-related track. The reweighting procedure is only needed for b-related vertices as the distributions of the other vertex categories do not vary with τ_B. The decay length distribution for b-related vertices is reweighted as follows to reflect a change in the B lifetime from τ_{gen} to τ_{new}. Each vertex in the final sample is assigned a weight W_1 based on the actual decay time τ_1 of the B hadron associated with it and a weight W_2 based on the decay time τ_2 of the B hadron in the opposite

hemisphere.

$$W_i = \frac{\frac{1}{\tau_{new}} e^{-\tau_i/\tau_{new}}}{\frac{1}{\tau_{gen}} e^{-\tau_i/\tau_{gen}}} \tag{160}$$

The decay length of each vertex is histogrammed with a weight equal to the product of these weights $W_1 \times W_2$, i.e. the weight is based on the probability of the two hemispheres having the decay times τ_1 and τ_2 at the new value of τ_B. Using this reweighting technique, the decay length distribution is generated at 81 values of τ_B from 0.2 ps to 2.3 ps in steps of 0.02 ps.

The procedure for constructing the MC decay length distribution for all the vertices in the final sample is explained below. Using the Monte Carlo, b-related vertices are further classified into 5 categories:

BB vertices with all tracks from the weak decay vertex of a B hadron.

CB vertices with all tracks from the weak decay of a hadron containing a cascade c quark.

BC vertices with tracks from the weak decay vertex of a B hadron and from the weak decay of a hadron containing a cascade c quark.

BO vertices with tracks from the weak decay vertex of a B hadron and from another source.

CO vertices with tracks from the weak decay of a hadron containing a cascade c quark and from another source.

Fake vertices are further subdivided into fakes from b events (FB) and fakes from $udsc$ events (FK). Primary charm vertices are sorted into only one category (CC). Thus, a total of 8 categories is used to describe all the vertices in the final sample. This division into 5 categories of b-related vertices is not necessary for the likelihood procedure but is used in understanding the different contributions to the decay length distribution. The decay length distribution for each category of vertex is shown in Figures 43 and 44. The fitting function $F_j(\tau_i)$ (for a given bin j) to which the data

is fitted is the sum of these distributions with suitable normalization factors.

$$F_j^{MC}(\tau_i) = \sum_{vtxtype} f_j^{MC}(\tau_i) \tag{161}$$

$$= \left[f_j^{CC} + f_j^{FK} + f_j^{FB} + f_j^{BB} N^{BB}(\tau_i) + f_j^{CB} N^{CB}(\tau_i) + f_j^{BC} N^{BC}(\tau_i) + f_j^{BO} N^{BO}(\tau_i) + f_j^{CO} N^{CO}(\tau_i) \right] H_{norm} \tag{162}$$

where

$$N^{xx}(\tau_i) = \frac{\text{Number of } xx \text{ vertices in original MC sample}}{\text{Number of } xx \text{ vertices in reweighted MC sample}} \tag{163}$$

and

$$H_{norm} = \frac{\text{Number of events in data}}{\text{Number of events in original MC sample}} \tag{164}$$

The normalization factors $N^{xx}(\tau_i)$ are necessary to normalize the contribution from the reweighted decay length distributions.

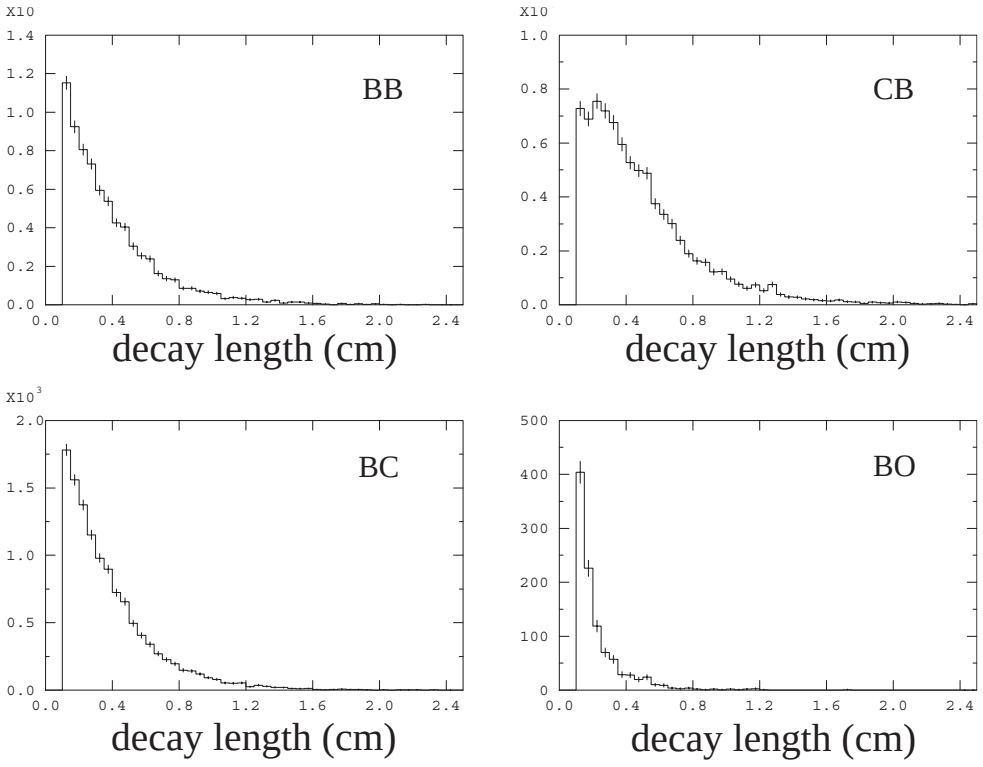

Figure 43: Decay length distributions of vertices from the Monte Carlo, classified according to track origin

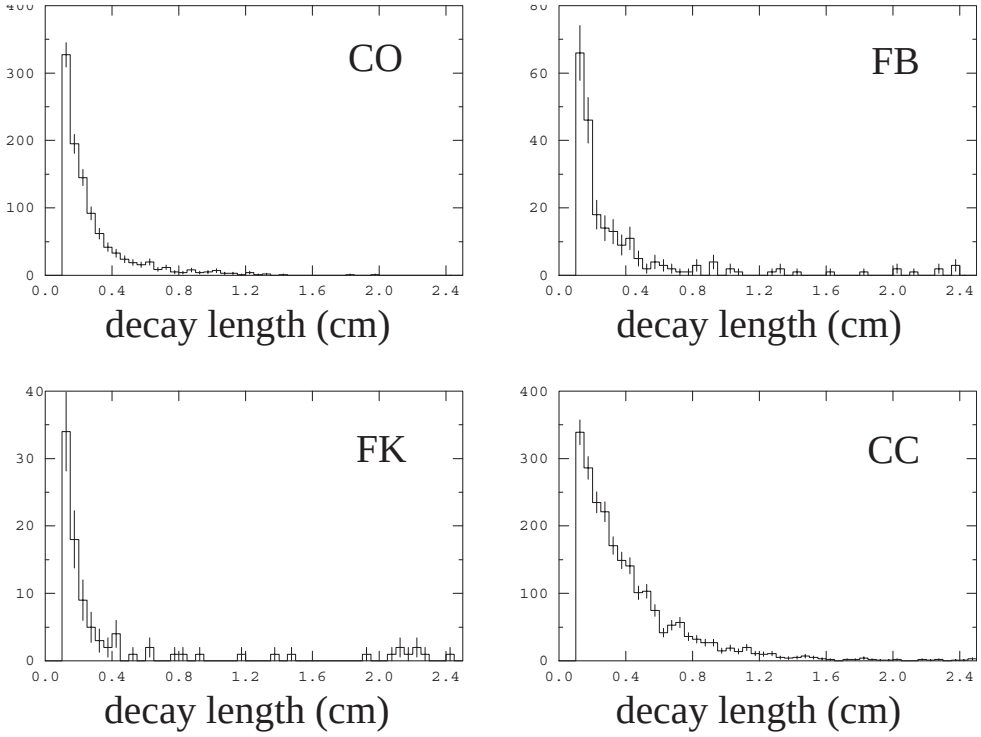

Figure 44: Decay length distributions of vertices from the Monte Carlo, classified according to track origin (cont.)

The data is fitted to the Monte Carlo by computing a log-likelihood in the fit using Poisson statistics and summing this over all bins. Thus, if the fitting functions of bin j are F_j^{data} and $F_j^{MC}(\tau_i)$ for the two distributions, the likelihood is

$$\mathcal{L}_j(\tau_i) = -2\ln\left(\frac{\left(F_j^{MC}(\tau_i)\right)^{F_j^{data}}}{F_j^{data}!}e^{-F_j^{MC}(\tau_i)}\right) \quad (165)$$

$$= 2\left(F_j^{MC}(\tau_i) - F_j^{data}\ln\left(F_j^{MC}(\tau_i)\right) + \ln\left(F_j^{data}!\right)\right) \quad (166)$$

A minimum of 10 entries per bin is required in the data, and bins are combined, if necessary, until this limit is reached. The fit is done over the range 0.1 cm to 0.6 cm in steps of 0.05 cm and from 0.6 cm to 2.5 cm in steps of 0.1 cm as this was found to improve the goodness of the fit. The log-likelihood sum is calculated for every value of τ_B in the analysis using the appropriate $F_j^{MC}(\tau_i)$. The lifetime is extracted by expressing the log-likelihood as a function of τ_B (see Figure 45) and finding the

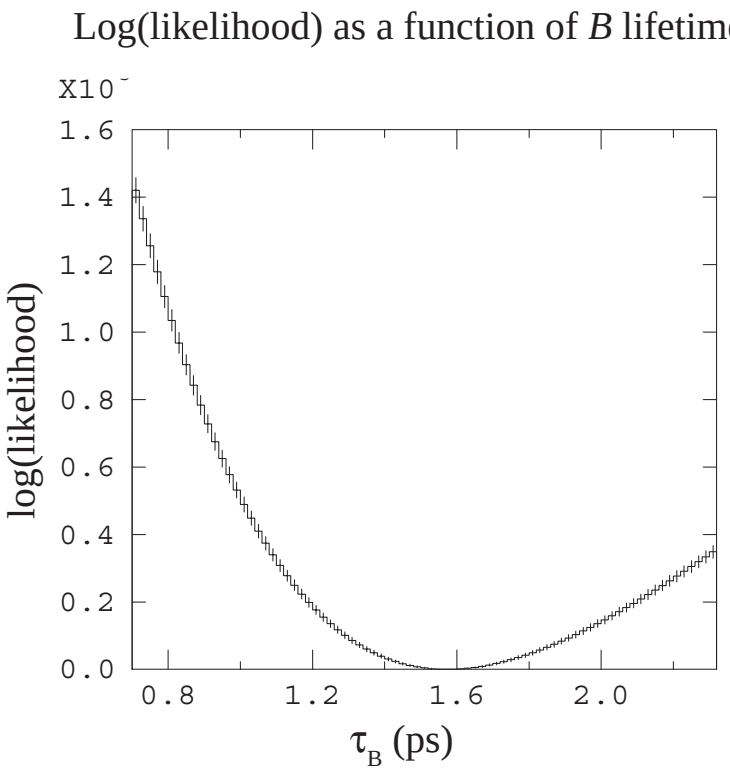

Figure 45: Distribution of log(likelihood) as a function of τ_B

minimum. The statistical error is calculated by fitting a parabola to the region around the minimum of $\mathcal{L}(\tau_i)$ and finding the change $\Delta\tau$ that produces a change $\Delta\mathcal{L}$ of $+1$. This is equivalent to a change in χ^2 of 1 [78] which results from a variation of ± 1 standard deviation from the fitted value.

Chapter 6

Results

In this chapter, the average B hadron lifetime resulting from the analysis detailed in chapter 5 is presented. The methods used to check the correctness of the method and of the simulation are detailed below. The calculation of the systematic errors assigned to the measurement is also explained below.

6.1 The τ_B Result

The average B hadron lifetime is extracted using the maximum likelihood method detailed in chapter 5. For the value presented in this thesis, all three sets of Monte Carlo events described in section 3.1 are used in the calculation of the main lifetime result in order to reduce the error arising from limited Monte Carlo statistics and to improve the goodness of fit. A further adjustment to the result comes from the fraction of D^+ mesons produced in $Z^0 \to c\bar{c}$ decays. In the Monte Carlo, 19.1% of charm hadrons produced in $Z^0 \to c\bar{c}$ events are D^+ mesons, which is lower than current experimental measurements [79], so the Monte Carlo sample is reweighted to change this fraction to 24.8%. The lifetime result quoted in this thesis after this reweighting is

$$\tau_B = 1.564 \pm 0.030 \text{ ps} \tag{167}$$

where the error is purely statistical. The χ^2 per degree of freedom at the fitted lifetime is 27.9/20.

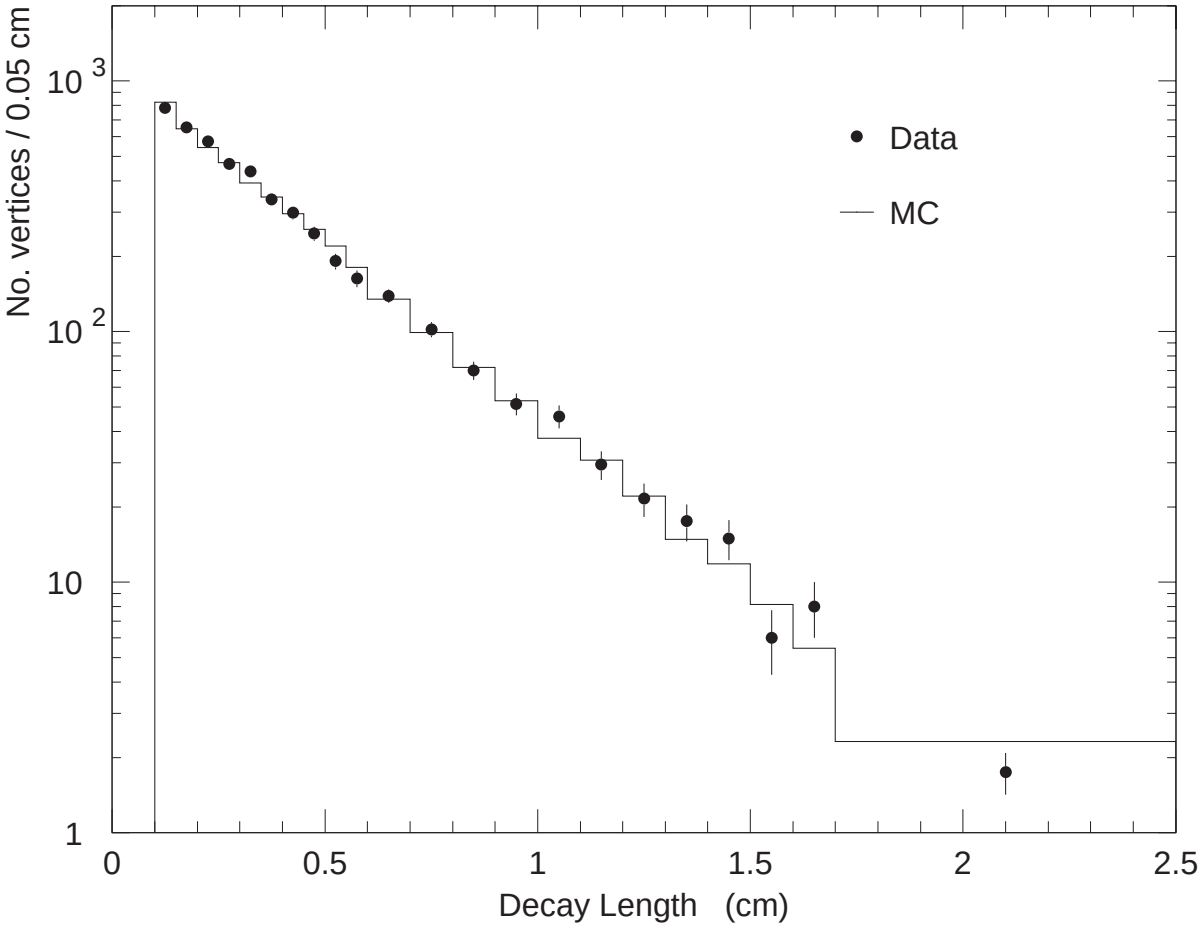

Figure 46: The decay length distribution for Monte Carlo (solid line) and data (points) at the fitted lifetime

The lifetime is also measured independently for each of the three Monte Carlo sets as a consistency check, giving the following values:

$$\tau_B = 1.576 \pm 0.032 \text{ ps for the 300000 event } udscb \text{ sample}$$
$$\tau_B = 1.555 \pm 0.030 \text{ ps for the 1.51 ps } b\bar{b} \text{ sample}$$
$$\tau_B = 1.558 \pm 0.028 \text{ ps for the 1.948 ps } b\bar{b} \text{ sample}$$

Figure 46 shows the decay length distribution for the full Monte Carlo sample and data at the fitted lifetime.

Figure 47 shows the χ^2 contribution for each bin in the fit. For this plot, the χ^2 of the fit between Monte Carlo and data is signed positive if the Monte Carlo entry

is greater than the corresponding data value for a bin. This 'signed' χ^2 distribution allows the contribution to the total χ^2 to be assessed for each bin. It is interesting to note that the bin at 1.05 cm contributes a large portion of the total χ^2.

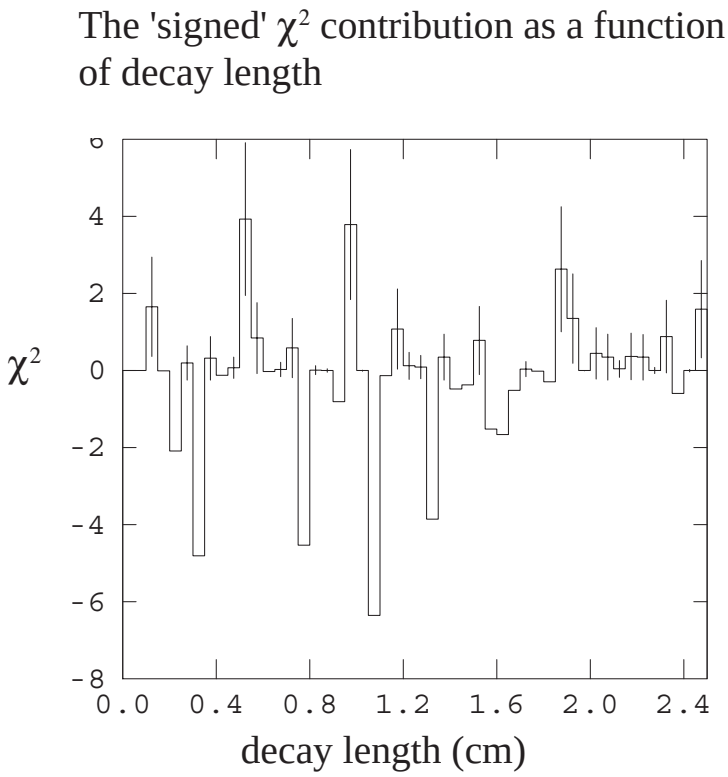

Figure 47: The 'signed' χ^2 distribution at the fitted lifetime

6.2 Consistency Checks

Several tests of the method and detector modeling are performed to assess biases inherent in the method used and are detailed below. In general, the 300000 event *udscb* Monte Carlo is used for these checks.

Sample	τ_B^{MC} (ps)
1	1.541±0.029
2	1.497±0.029
3	1.519±0.030
4	1.446±0.028
5	1.530±0.029
mean + RMS	1.507 ps and 0.038 ps

Table 25: Extraction of the generated lifetime using the Monte Carlo as a data set

6.2.1 Extracting the Generated Lifetime from the Monte Carlo

The analysis is tested to see if it can reproduce the generated lifetime in the Monte Carlo. The 300000 event Monte Carlo sample (τ_{gen} = 1.51 ps) is used; 20% of the events are used as a data set which is fitted to the remaining 80% of the Monte Carlo. The data set is assembled by picking events distributed throughout the Monte Carlo sample to eliminate possible biases. Five different data sets are constructed and the lifetime is calculated for each one. Table 25 shows the results of the five calculations. The mean measured lifetime is 1.507 ps with an RMS of 0.038 ps, which is consistent with the input lifetime and the statistical error expected for the sample size.

6.2.2 Azimuthal Variation

Azimuthal variation in the lifetime measurement is investigated by calculating the lifetime independently in four quadrants of the detector. The quadrants are chosen to be between axes at 45° to the x and y axes because this confines faulty hardware in the VXD to only two of the quadrants. The quadrant between 135° and 225° has bad CCDs and the quadrant between 45° and 135° has a faulty ladder, as described in section 2.2.1. The four lifetime measurements and the $\chi^2/d.o.f.$ of the fit between data and Monte Carlo at the measured lifetime are shown in Table 26. As might be expected the fit quality is worse in the quadrants with VXD hardware problems. The four values are all consistent with the nominal value of τ_B quoted above, and with each other.

Quadrant	τ_B (ps)	$\chi^2/d.o.f.$
$45° \leq \phi < 135°$	1.597 ± 0.061	32/17
$135° \leq \phi < 225°$	1.544 ± 0.044	24/18
$225° \leq \phi < 315°$	1.574 ± 0.065	15/14
$315° \leq \phi < 45°$	1.509 ± 0.060	18/15

Table 26: Azimuthal variation in the lifetime measurement

Run epoch	τ_B (ps)
pre-veto	1.535 ± 0.064
veto	1.604 ± 0.050
post-veto	1.558 ± 0.049

Table 27: The lifetime measured during different run epochs

6.2.3 Variation Between Parts of the Run

The CDC veto problem described in section 4.1 divides the 1993 run into three main epochs: pre-veto, veto period and post-veto. The sensitivity of the analysis to the veto is assessed by performing the measurement for the three epochs independently. The effects of the veto period are corrected in the Monte Carlo by rejecting a fraction of triggers. Thus one might expect a shift in the value of τ_B measured if this correction does not model the data well. With the statistics available, the three results are consistent with the main result and are shown in Table 27.

6.2.4 Sensitivity to the Tag

If the true value of the B hadron lifetime is very different from that in the Monte Carlo, the efficiencies and purities of the quark flavors used in the analysis may be biased. If no other cuts are applied, the sample composition used in the maximum likelihood analysis may be incorrect, leading to a biased measurement of the lifetime. The sensitivity to the choice of tagging criteria is investigated in several ways.

The vertex composition and decay length distributions for tagged and untagged $Z^0 \rightarrow b\bar{b}$ events that pass all the cuts in the analysis are compared (see Table 28 and Figure 48). There is little difference between these tagged and untagged final samples; the main reason a tag is used in the analysis is to reduce the amount of time

vertex type	Composition (%)	
	Tagged	Untagged
b	24	24
cascade c	27	27
b + cascade c	40	40
b + other	4	4
cascade c + other	4	4
IP	0.6	0.3

Table 28: Vertex composition of final vertex sample using tagged and untagged $Z^0 \rightarrow b\bar{b}$ events

spent processing background events. The lack of sensitivity to the tag in the final sample is due to the 1 mm decay length cut which removes backgrounds especially from $Z^0 \rightarrow c\bar{c}$ decays. The final sample is thus less dependent on the choice of cuts used in tagging b events.

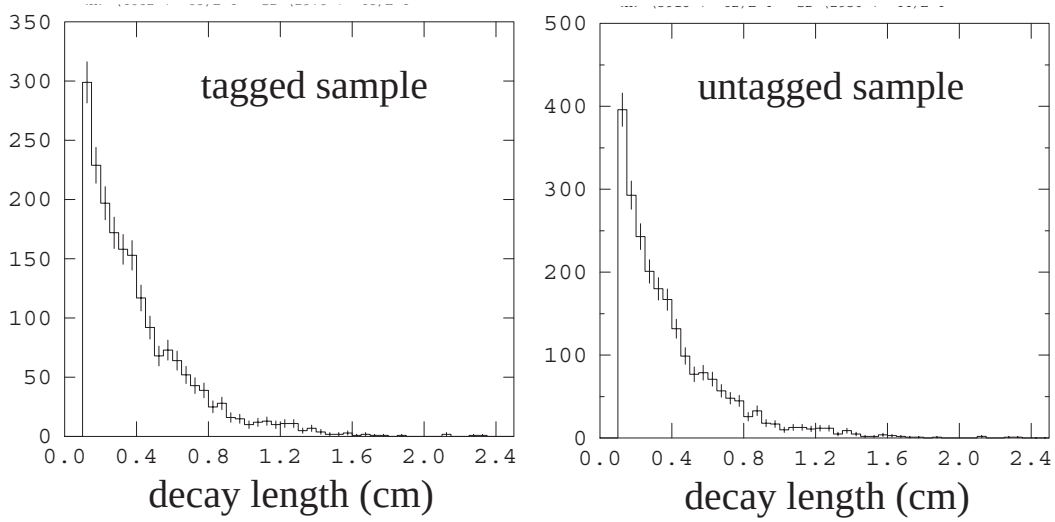

Figure 48: Decay length distributions of tagged and untagged $Z^0 \rightarrow b\bar{b}$ events

As described in section 5.1.4, an alternate tag can be employed in which a jet is tagged, and the hemisphere opposite the jet is used in the analysis. This reduces any bias the tag may have towards longer-lived particles, but suffers from much lower

statistics. The lifetime calculated using this tag is $\tau_B = 1.616 \pm 0.052$ ps, which is consistent with the result reported here.

6.2.5 Choice of Vertex

In hemispheres containing more than one vertex, the vertex closest to the IP is used in the lifetime calculation. As the average number of vertices per hemisphere is 0.69, most hemispheres are unaffected by this choice of vertex. As a cross-check, the farthest vertex from the IP is used, yielding a lifetime of 1.564 ± 0.031 ps, which is consistent with the reported result.

6.3 Systematic Errors

As explained earlier, this analysis does not reconstruct the true B decay vertex and instead relies on the Monte Carlo to relate the vertex decay length to the proper decay time of the B hadron. Thus, the analysis will be more model-dependent than other analyses, e.g. lepton impact parameter measurements, and all major sources of systematic error need to be identified. The simulation of vertex construction and selection will be sensitive to the modeling of quantities that affect the numbers of tracks from the B decay and from the primary vertex, e.g. fragmentation, decay multiplicities, and tracking efficiencies. The lifetime can be expected to be sensitive to the modeling of the b fragmentation because the B hadron momentum is not directly measured, but implicitly assumed from the fit to the Monte Carlo vertex decay length. The modeling of charm hadron decays is important as these still contribute non-negligibly to the vertex sample both in tertiary charm decays in b events and in the primary charm background. The sensitivity to the cuts in the analysis and fit must also be understood.

A comprehensive selection of sources of systematic error is investigated. A basic difficulty in assessing some of these errors is defining the range of the variation that corresponds to one standard deviation. Where possible, parameters are varied by the uncertainties in their world average values. In general, the errors are estimated

conservatively and there is probably some correlation between some of them. Systematic errors are measured by recalculating the lifetime after modifying the Monte Carlo sample to reflect the error being investigated. Events are reweighted to reflect these variations, as regenerating Monte Carlo events and reconstructing them is impractical. The 300000 event *udscb* sample is used for the calculation of systematic errors.

The errors can be divided into three categories: those due to uncertainties in the modeling of the detector, those due to uncertainties in the physics model, in particular, the B decay model, and those arising from the particular method of the analysis.

6.3.1 Detector Related Errors

Tracking Efficiency Corrections

As described in section 5.1.3, tracking efficiency corrections are applied to correct the fraction of tracks in the Monte Carlo that pass the "quality" cuts to match that in the data. These corrections are *ad hoc* and the sensitivity to them is probed by the following procedures. The corrections are applied as a function of the momentum (p) and direction (ϕ and θ) of a track. Thus, turning off the correlation in one variable at a time is a reasonable assessment of the uncertainty in the efficiency corrections. This is done by using the average of all the correlated efficiencies for that variable at the value of the other two variables. For example, the momentum correlation is turned off by using the average of all the efficiencies at a particular value of ϕ and θ.

$$\begin{aligned} \epsilon(p,\theta,\phi) &\rightarrow \epsilon(\langle p\rangle,\theta,\phi) \\ &= \langle\epsilon(p)\rangle\,\epsilon(\theta,\phi) \end{aligned} \tag{168}$$

The "quality" tracks passing the modified efficiency correction then go through the same tagging and analysis as before. A lifetime is extracted for each of the three modified corrections by fitting to the normal data sample. The changes in the lifetime are

$$\Delta\tau_B(p) = 0.003 \text{ ps},$$

$$\begin{aligned} \Delta\tau_B(\phi) &= 0.007 \text{ ps, and} \\ \Delta\tau_B(\theta) &= 0.005 \text{ ps.} \end{aligned} \tag{169}$$

As mentioned in section 5.1.3. after applying the nominal tracking efficiency correction, the multiplicities of "quality" tracks in the data and Monte Carlo fail to track each other over the full 1993 run: a discrepancy of ± 0.3 "quality" tracks remains. The effect of this on the lifetime result is assessed by reducing the average "quality" track multiplicity in the Monte Carlo sample by 0.3 tracks in the untagged sample. A full vertexing analysis is then done on this set of Monte Carlo events, and a lifetime is measured by a fit to the normal data sample. The lifetime changes by

$$\Delta\tau_B(\text{qual tk}) = 0.010 \text{ ps.} \tag{170}$$

Thus, the total error assigned to the tracking efficiency corrections is

$$\Delta\tau_B(\text{tk eff}) = 0.013 \text{ ps.} \tag{171}$$

Modeling the Primary Vertex Position

The Monte Carlo and data both display non-Gaussian tails in the distributions of the primary vertex position, as described in section 3.2.2. The uncertainty in the modeling of the tails of these distributions needs to be assessed because it can have a large effect on aspects of this analysis. For example, the fragmentation will not be properly modeled if tracks are not assigned to the primary or secondary vertex in the same way in the Monte Carlo as in the data. Decay length distributions of vertices will also not match, as the decay length is calculated with respect to the reconstructed primary vertex.

In x and y, the tails are small and are simulated by Gaussian-smearing the IP position in x and y by 100 μm in 0.25% of events. Vertex positions are recalculated relative to the new IP position and the lifetime is recalculated. There is negligible effect on the measured lifetime.

$$\begin{aligned} \Delta\tau_B(\text{IP}_x) &< 0.001 \text{ ps, and} \\ \Delta\tau_B(\text{IP}_y) &< 0.001 \text{ ps.} \end{aligned} \tag{172}$$

The tails of the longitudinal (z) IP position distribution are not modeled by the Monte Carlo because they cannot be measured from a comparison of data and Monte Carlo. This is because the luminous region along the beam axis is an envelope ~ 700 μm wide, while the primary vertex can be measured in each event to an accuracy of $\sim 30-50$ μm. The systematic error due to the lack of knowledge of these longitudinal tails is not assessed independently because it overlaps with other systematic errors, viz. those arising from b fragmentation and VXD alignment uncertainties.

VXD Alignment

The core of the rz impact parameter distribution is narrower in the Monte Carlo than in the data. This is found to be due to residual misalignment within the VXD and a ϕ dependence in the polar angle matching between the CDC and the VXD. The effect of this mismatch is simulated by adjusting the z coordinates of tracks in the Monte Carlo at the xy point of closest approach (z_{doca}). The misalignment can be represented by a Gaussian smear of $(16/\sin\theta)$ μm on the z_{doca}, and the ϕ dependence is assessed using a ϕ dependent shift of the z_{doca} of $\sim \pm 20$ μm. The primary vertex z position is recalculated using the smeared or shifted tracks and the lifetime is measured. The changes in the lifetime are

$$\begin{aligned} \Delta\tau_B(z\text{-smear}) &= 0.004 \text{ ps, and} \\ \Delta\tau_B(z\text{-shift}) &= 0.003 \text{ ps.} \end{aligned} \tag{173}$$

6.3.2 Physics Related Errors

b and c Fragmentation

The Monte Carlo models b and c fragmentation using the Peterson parameterization [61], as described in section 3.1.1. An uncertainty in one's knowledge of the fragmentation functions directly translates into an uncertainty in the modeling of the number of fragmentation tracks. This affects how well the simulation models the parts of the analysis related to tracking. For example, one's knowledge of the purity and efficiency

of the b-tagging is related to the uncertainty in the parameterization of the fragmentation. The vertexing efficiency and composition of the vertex sample, and thus the choice of partition, is also related to the accuracy of the fragmentation modeling. The uncertainty in the heavy quark fragmentation also affects the modeling of the primary vertex position and the impact parameter distributions. Thus, these systematic errors can have wide ranging effects and need to be assessed conservatively. In fact, the uncertainty in the b fragmentation is the largest source of systematic error in this analysis. The error due to b fragmentation comes from varying the Peterson parameter $\epsilon_b = 0.006 \pm 0.0015$, which corresponds to $\langle x_E \rangle = 0.700 \pm 0.011$. This is conservatively chosen to be larger than the error on several individual measurements [62]. The variation of the lifetime with a change in the hardness of the fragmentation is done by reweighting the vertices in the final sample. The correlation between the B hadron momentum in one hemisphere with that in the opposite hemisphere is accounted for in the calculation of the weights. The weights are calculated using a set of generator-level $Z^0 \to b\bar{b}$ events generated at each of three values of ϵ_b. The number of events is tabulated as a function of the two B hadron momenta in the event, and the weights are calculated by taking the ratio between corresponding entries in the tables. This correlation procedure is necessary to avoid grossly overestimating our dominant error. The uncertainty in the lifetime corresponding to this variation is

$$\Delta\tau_B = 0.016 \text{ ps}. \tag{174}$$

As a further check, the Monte Carlo sample is reweighted to simulate the effect of using the modified Bowler parameterization to describe b fragmentation at the same value of $\langle x_E \rangle$. The effect of this is

$$\Delta\tau_B = 0.009 \text{ ps}, \tag{175}$$

giving a total error due to b fragmentation of

$$\Delta\tau_B(b \text{ frag}) = 0.018 \text{ ps}. \tag{176}$$

The sensitivity to the c fragmentation parameterization [80] is assessed by the variation $\epsilon_c = 0.06 \pm 0.015$ which corresponds to $\langle X_E \rangle = 0.49 \pm 0.3$. The two event

hemispheres are not correlated as this is not as large a source of error as the uncertainty in the b fragmentation and doing so would not reduce the error estimate significantly. The error in the lifetime due to c fragmentation is

$$\Delta\tau_B(c \text{ frag}) = 0.010 \text{ ps}. \tag{177}$$

R_b and R_c

The uncertainties in the branching fractions $R_b = \Gamma_{Z\to b\bar{b}}/\Gamma_{Z\to\text{hadrons}}$ and $R_c = \Gamma_{Z\to c\bar{c}}/\Gamma_{Z\to\text{hadrons}}$ affect the composition of the sample. For example, if the data has a higher value of R_b than in the Monte Carlo, the final sample will contain more $Z \to b\bar{b}$ events. The lifetime would therefore be calculated by fitting to a Monte Carlo sample containing too large a fraction of $Z^0 \to c\bar{c}$ events, which would shift the fitted lifetime. R_b and R_c are varied by the uncertainties in their world averages[4], which are $R_b = 0.221 \pm 0.00003$ and $R_c = 0.171 \pm 0.0002$. These uncertainties are very small, consequently the effect on the lifetime is also small. The high purity ($\sim 90\%$) of the tagged sample also reduces the sensitivity to the variation in R_c. The resulting errors are:

$$\begin{aligned} \Delta\tau_B(R_b) &< 0.001 \text{ ps} \\ \Delta\tau_B(R_c) &= 0.002 \text{ ps}. \end{aligned} \tag{178}$$

D^{**} Production in B Hadron Decays

Semileptonic B hadron decays produce either D, D^*, or D^{**} mesons. The Monte Carlo produces these in the ratio $0.33 : 0.58 : 0.09$, respectively. However, measurements from CLEO [71] indicate that D^{**} mesons should be produced in $\sim 21\%$ of decays. Thus, semileptonic B decays can be expected to have a higher average multiplicity than is present in the Monte Carlo. Because this measurement uses all decay modes of B hadrons and not just the semileptonic decays, few events are affected by this correction. Changing the Monte Carlo sample to reflect the change in D^{**} production does not change the lifetime.

$$\Delta\tau_B(D^{**} \text{ fraction}) < 0.001 \text{ ps}. \tag{179}$$

Charm Hadron Lifetimes

The lifetimes of D^+, D^0, D_s, and Λ_c are varied by the uncertainties in their world averages [4], which are all quite small. The main effect comes from varying the D^+ lifetime, which is $\tau_{D^+} = 1.057 \pm 0.015$ ps, i.e. ~ 2.5 times greater than the others and similar to τ_B. Uncertainties in the charm hadron lifetimes create an uncertainty in modeling the size of the charm background. However, with the high-purity sample used in this analysis, this should not be a large effect. The position of the tertiary charm decay vertex in a b event is also sensitive to these uncertainties, which can directly affect the vertex position chosen for the lifetime measurement as over 50% of vertices in the final sample have some tracks from the tertiary vertex. However, only 19.1% of charm hadrons are D^+ in the Monte Carlo, so the effect is not as great as might be expected.

$$\Delta\tau_B(\text{charm lifetimes}) = 0.004 \text{ ps}. \tag{180}$$

B Baryon Fraction in the Final Sample

The absolute fraction of B baryons in $Z^0 \to b\bar{b}$ decays is varied by $\pm 5\%$. This variation is somewhat arbitrary and is thought to be a conservative estimate. From the previous chapter it is seen that the analysis selects B mesons with slightly higher efficiency than B baryons, which have a shorter lifetime. Therefore, if the fraction of B baryons in the data is lower than in the Monte Carlo, the lifetime will be measured systematically high because only the B meson lifetime is varied in the fit. From this variation, the error is:

$$\Delta\tau_B(B \text{ baryon frac}) = 0.004 \text{ ps}. \tag{181}$$

Charm Content of B Hadron Decays

The sensitivity to the charm content of B hadron decays is assessed using the uncertainty in the world average values [4] for the $B \to$ charm hadron branching ratios, which come from measurements made at the $\Upsilon(4s)$ resonance. Therefore, the branching ratios are only for B^+ and B^0 meson decays. In Z^0 decays, B_s and B baryons are also produced, so the sensitivity to the charm content of their decays needs to

be assessed. As a conservative estimate, the charm content in B^0 and B^+ decays is varied by its uncertainty and the resulting error is inflated by 100%. This systematic error also addresses the sensitivity to the D^+ contribution in both tagging and in the construction of a vertex position.

$$\Delta\tau_B(\text{charm content}) = 0.014 \text{ ps.} \tag{182}$$

D Momentum Spectrum in B Decays

The momentum spectra of D^+ and D^0 mesons in B decays in the Monte Carlo have been compared to recent measurements from CLEO [81] as shown in Figure 49. The Monte Carlo B decay model has been tuned to reproduce these spectra as much as possible but there is still some disagreement. The sensitivity of this measurement to this disagreement is estimated by measuring the change in τ_B that arises from forcing the Monte Carlo spectra to agree exactly with the CLEO results.

$$\Delta\tau_B(D \text{ momentum}) = 0.004 \text{ ps.} \tag{183}$$

Charm Hadron Fraction

The absolute fractions of D^+ and charm baryons in $Z^0 \to c\bar{c}$ events is varied by $\pm 3.6\%$ and $\pm 3.0\%$, respectively. The long lifetime of the D^+ can lead to a larger fraction of primary charm events being tagged.

$$\Delta\tau_B(D^+ \text{ fraction}) < 0.001 \text{ ps} \tag{184}$$

$$\Delta\tau_B(\text{charm baryon fraction}) = 0.012 \text{ ps.} \tag{185}$$

Thus, the total systematic error from varying the charm hadron fractions is:

$$\Delta\tau_B(\text{charm hadron fraction}) = 0.012 \text{ ps.} \tag{186}$$

B Hadron Decay Multiplicity

Variation in the charged track multiplicity in B hadron decays affects the proportion of events that are tagged and the number of vertices found, as well as other quantities

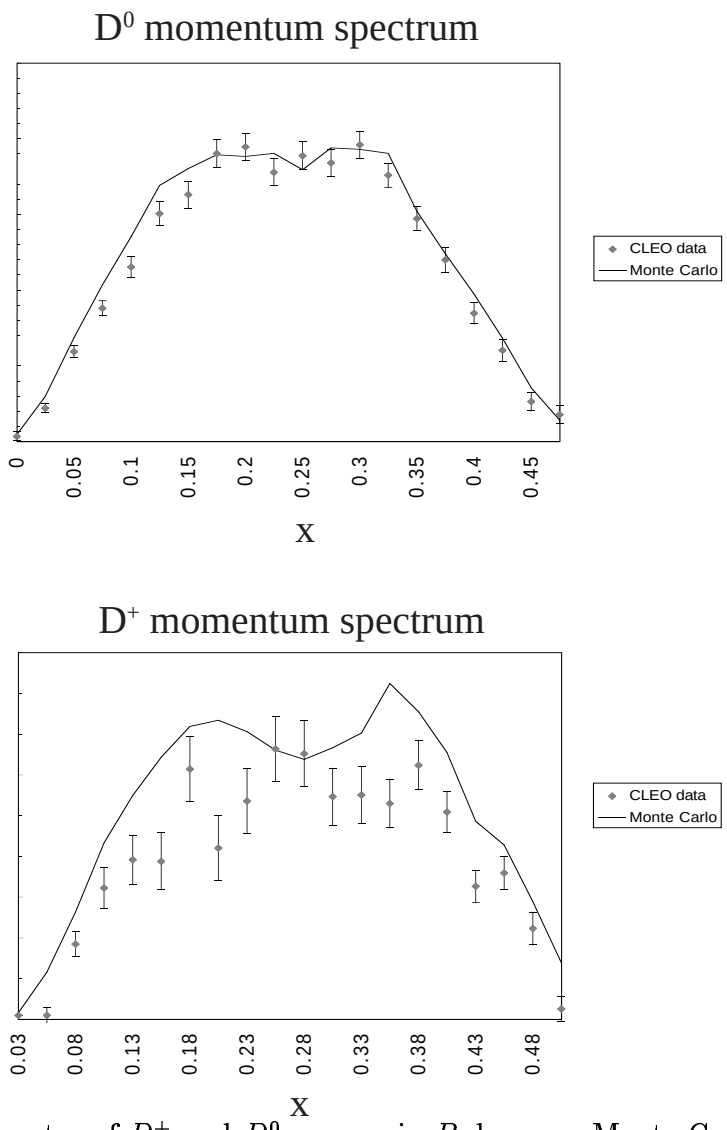

Figure 49: Momentum spectra of D^+ and D^0 mesons in B decays – Monte Carlo and recent CLEO data

dependent on tracking. The multiplicity is varied by ± 0.3 tracks to reflect the current uncertainty in its value [82]. This is ~ 2.5 times the error on the B meson decay multiplicity measured at the $\Upsilon(4s)$ [83, 84]. The large variation used here compensates for the lack of measurements of B_s and B baryon decay multiplicities. The change in the lifetime is

$$\Delta\tau_B(B \text{ mult}) = 0.009 \text{ ps} \tag{187}$$

6.3.3 Analysis Related Errors

Vertex and Partition Limits

The limits on the number of vertices and partitions per event are a possible source of biases in the final sample, especially as they are not cuts motivated directly by the physics but by limitations of computing power. The two events in the data that fail the 200 vertex limit are also rejected by the partition limit in the following stage of the analysis. Thus, the effect of the vertex limit need not be considered separately from the effect of the limit on the number of partitions. The partition limit rejects 1.0% of tagged events, all of which are $Z^0 \to b\bar{b}$ decays according to the Monte Carlo. The distribution of the true decay length of B hadrons in these events is different from that of the events in the final sample. The rejected events have a peak slightly removed from the IP, as seen in Figure 50, which suggests that tracks from these events may be able to form more fake vertices with IP tracks. The effect that these events have on the lifetime is measured by reweighting the vertex decay length distribution in the Monte Carlo as follows. The B hadron decay length distribution of the rejected events is added to that of the final sample and the ratio to the old distribution provides weights as a function of decay length. These are applied to the vertex decay length distribution and the lifetime is recomputed. The effect is small.

$$\Delta\tau_B(\text{ptn limit}) = 0.003 \text{ ps}. \tag{188}$$

Decay Length Cut During Vertex Construction

In order to assess the effect of the requirement that only vertices greater than 1 mm from the IP can be constructed, the analysis is run again on both the data and Monte Carlo with a 0.5 mm decay length cut. The lifetime is measured for each set from a fit over the same range as in the original analysis to isolate the effect of the cut, i.e. the fit does not start at 0.5 mm as this can not be directly compared to the fit in the original analysis.

$$\Delta\tau_B(\text{decay length cut}) = 0.007 \text{ ps}. \tag{189}$$

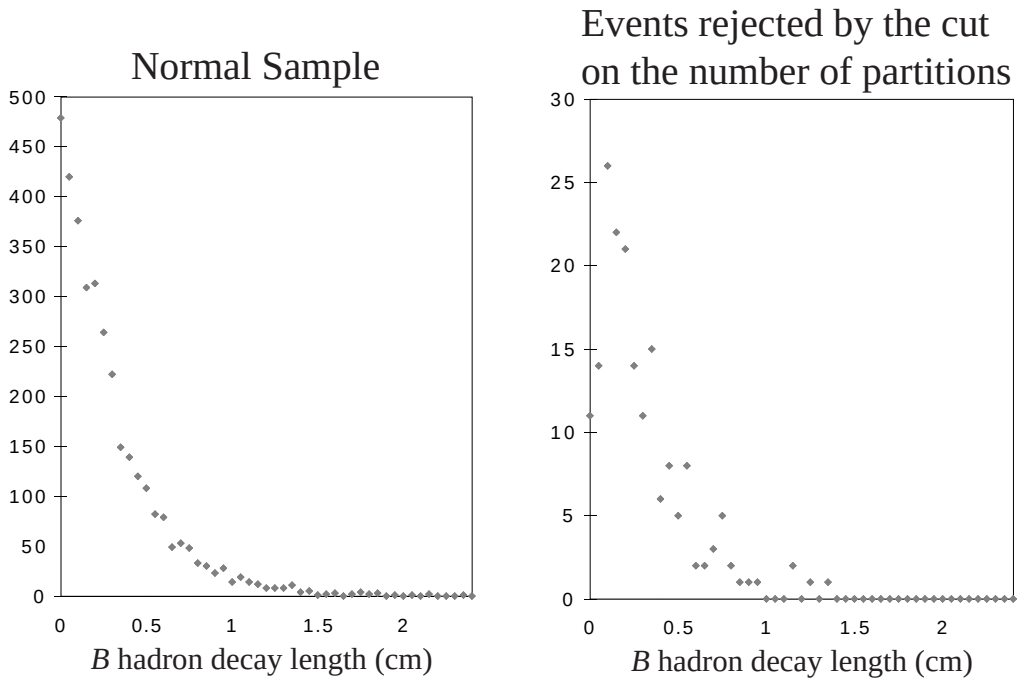

Figure 50: True decay length distributions of B hadrons in events passing and failing the cut on the number of partitions

Fit Related Errors

The starting bin of the fit is varied from 1 mm to 5 mm in steps of 0.5 mm. Because of the increasing statistical error as the lower end of the fit is raised, the error is taken to be the RMS of the first 5 results.

$$\Delta\tau_B(\text{fit range}) = 0.006 \text{ ps} \tag{190}$$

The fit is also done with a reduced upper limit, giving values consistent with the nominal value quoted. The bin size is varied from 0.25 mm to 2 mm and the results are shown below.

$$\tau_B(0.25 \text{ mm}) = 1.563 \pm 0.030 \text{ ps}$$
$$\tau_B(0.5 \text{ mm}) = 1.564 \pm 0.030 \text{ ps}$$
$$\tau_B(1.0 \text{ mm}) = 1.568 \pm 0.030 \text{ ps}$$
$$\tau_B(2.0 \text{ mm}) = 1.580 \pm 0.029 \text{ ps}$$

The RMS of these results is taken as the error.

$$\Delta\tau_B(\text{bin size}) = 0.007 \text{ ps} \tag{191}$$

Monte Carlo Statistics

In the lifetime fit, the fitting function provided by the Monte Carlo has an uncertainty due to its own limited statistics. The uncertainty in the lifetime measurement that arises from the finite Monte Carlo statistics is assessed by comparing the number of events passing event selection in the data to that in the Monte Carlo. The contributions of the two Monte Carlo sets that are pure $b\bar{b}$ samples are weighted by the ratio:

$$F = \frac{\text{Total number of } Z^0 \text{ decays passing event selection}}{\text{Number of } Z^0 \to b\bar{b} \text{ decays passing event selection}} \tag{192}$$

Thus the full Monte Carlo is equivalent to $\sim$ 800000 *udscb* events in its analyzing power. The statistical error of the τ_B measurement is scaled by the square root of the ratio of the number of events passing event selection in the data to the effective number of events passing event selection in the Monte Carlo, giving

$$\Delta\tau_B(\text{MC stat}) = 0.008 \text{ ps}. \tag{193}$$

6.3.4 Summary of Systematic Errors

The full list of systematic errors assigned to this lifetime measurement is shown in Table 29. The total systematic error is ± 0.036 ps.

error source	$\Delta\tau_B$
Tracking efficiency	0.013
Primary vertex position (x and y)	< 0.001
VXD alignment	0.005
b fragmentation	0.018
c fragmentation	0.010
R_b	< 0.001
R_c	0.002
D^{**} fraction	< 0.001
Charm lifetimes	0.004
B baryon fraction	0.004
Charm content of B decays	0.014
D momentum spectrum in B decays	0.004
Charm hadron fraction	0.012
B hadron decay multiplicity	0.009
Partition limit	0.003
Decay length cut in vertex construction	0.007
Fit range	0.006
Bin size	0.007
MC statistics	0.008
TOTAL	0.036

Table 29: Systematic errors for the lifetime measurement

Chapter 7

Conclusion

In this thesis we have measured the average B hadron lifetime at SLD using a sample of ~ 50000 Z^0 decays. The sample was enriched in $Z^0 \to b\bar{b}$ decays by selecting events with a large number of high impact parameter tracks. The tagged sample contained 4299 events with a purity and efficiency of 90% and 60%, respectively, for $Z^0 \to b\bar{b}$ events. Very loose criteria were used to construct all possible geometric vertices in three dimensions that were at least 1 mm from the IP. All possible ways (partitions) of uniquely assigning each track to a vertex were constructed. One partition per event hemisphere was chosen and the closest vertex to the IP in the selected partition was used in the lifetime determination. The analysis selected an average of 0.6 vertices per hemisphere in tagged events. The lifetime was measured from a maximum-likelihood analysis of the vertex-IP decay length distribution.

$$\tau_B = 1.564 \pm 0.030(\text{stat}) \pm 0.036(\text{syst}) \text{ ps} \tag{194}$$

This result is limited by the systematic error. The result is consistent with the 1994 world average [4] and, like other hadronic measurements [36], has a higher value than measurements made with semileptonic B decays. This small difference, if significant, may point to a difference between the B^0 and $B^{\pm}$ lifetimes.

This analysis has demonstrated the power of using vertices in a lifetime analysis at SLD. The small and stable beam spot, and the excellent vertex resolution allow the B hadron lifetime to be measured with a low statistical error, even with modest

numbers of events. However, the result is sensitive to the modeling of all aspects of the analysis and a comprehensive investigation of sources of systematic error was necessary. SLD now has an additional 100000 Z^0 decays from the 1994-95 run. These can be used in conjunction with tighter cuts to increase the purity of the sample and reduce the dependence on the modeling of the charm background. The larger event sample can also be used to make preliminary measurements of the charged-to-neutral lifetime ratio in which the vertex charge is also measured. Current results are not able to resolve a difference between the lifetimes and further results are needed.

Further work can be done to improve the measurement by reducing the dominant systematic errors. The systematic error due to the modeling of b fragmentation can be reduced by measuring the B hadron momentum in every event hemisphere. However, as the true B hadron decay vertex is not reconstructed in this analysis, care is needed in reconstructing the B momentum correctly from the vertices used by the analysis. Improvements have been made in the Monte Carlo simulation, particularly in the tracking, and these will change the systematic error, but work needs to be done to estimate any new biases that may have been introduced by these changes.

Bibliography

[1] F. Halzen and A. D. Marten, *Quarks and Leptons: An Introductory Course in Modern Particle Physics*, John Wiley & Sons, New York, (1984).

[2] K. Abe *et al.*, *Phys. Rev. Lett.* **73**, 25 (1994).

[3] K. Abe *et al.*, *Phys. Rev. Lett.* **74**, 2890 (1995).

[4] Particle Data Group, *Phys. Rev.* **D 45**, *Part 1*, 50(3):1, 1994.

[5] V. D. Barger and R. J. N. Phillips, *Collider Physics*, Addison-Wesley, 1987.

[6] P. Renton, *Electroweak Interactions*, Cambridge, 1990.

[7] T. E. Browder, K. Honscheid and S Playfer, *A Review of Hadronic and Rare B Decays*, CLNS-93/1261 (1994).

[8] M. Bauer and B. Stech, *Phys. Lett.* **152B**, 380 (1985).

[9] D. Green, *Lectures in Particle Physics*, chapter 2, World Scientific (1994).

[10] J. L. Cortes, X. Y. Pham and A. Tounsi, *Phys. Rev.* **D25**, 188 (1982).

[11] M. Suzuki, *Nucl. Phys.* **B145**, 420 (1978).

[12] N. Cabibbo and L. Maiani, *Phys. Lett.* **79B**, 109 (1978).

[13] H. Albrecht *et al.*, *Phys Lett.* **B255**, 297 (1991).

[14] R. Fulton *et al.*, *Phys. Rev. Lett.* **64**, 16 (1990).

[15] G. Altarelli and L. Maiani, *Phys. Lett.* **B52**, 351 (1974); M. Gaillard and B. W. Lee, *Phys. Rev. Lett.* **33**, 108 (1974).

[16] G. Altarelli *et al.*, *Nucl. Phys.* **B208**, 365 (1982).

[17] M. Wirbel, B. Stech and M. Bauer, *Z. Phys.* **C29**, 637 (1985).

[18] N. Isgur *et al.*, *Phys. Rev.* **D39**, 799 (1989).

[19] S. Stone, *Semileptonic B Decays* in *B Decays*, ed. S. Stone, World Scientific, Singapore (1992).

[20] J. Jaros, *B Lifetimes* in *B Decays*, ed. S. Stone, World Scientific, Singapore (1992).

[21] M. Bauer, B. Stech and M. Wirbel, *Z. Phys.* **C34**, 103 (1987).

[22] N. Isgur and M. Wise, *Phys. Lett.* **B237**, 527 (1990).

[23] D. H. Fujino, *Measurement of the Average Bottom Hadron Lifetime at the Z^0 Resonance*, Ph. D. thesis, Stanford University (1992).

[24] B. Blok and M. Shifman, *Phys. Rev.* **D47**, 2949 (1993).

[25] J. D. Richman and P. R. Burchat, UCSB-HEP-95-08 (1995).

[26] J. Bartelt *et al.*, *Phys. Rev. Lett.* **71**, 4111 (1993).

[27] M. Acciari *et al.*, *Phys. Lett.* **B335**, 542 (1994).

[28] T. Inami and C. S. Lim, *Prog. Theor. Phys.* **65**, 297 (1981); Erratum: **65**, 1772 (1982).

[29] S. Manly, *CP Violation at the Z^0* in *SLD Physics Studies, Proceedings of the SLD Physics Week*, Kirkwood, California, SLAC Report 354 (1989).

[30] The BaBar Collaboration, *The BaBar Technical Design Report*, (1995).

[31] I. I. Bigi, CERN-TH.7207/94 (1994).

[32] Particle Data Group, *Phys. Rev.* **D45**, *Part II* (1992).

[33] D. Decapm *et al.*, *Phys. Lett.* **B257**, 492 (1991).

[34] O. Adriani *et al.*, *Phys Lett.* **B317**, 474 (1993).

[35] P. D. Acton *et al.*, *Z. Phys.* **C60**, 217 (1993).

[36] P. Abreu *et al.*, *Z. Phys.* **C63**, 3 (1994).

[37] D. Buskulic *et al.*, *Phys. Lett.* **B314**, 459 (1993).

[38] F. Abe *et al.*, *Phys. Rev. Lett.* **71**, 3421 (1993).

[39] M. Athanas *et al.*, CLNS-94/1286 (1994).

[40] P. Abreu *et al.*, DELPHI 94-97 PHYS 414 (1994); R. Akers *et al.*, *Z. Phys.* **C67**, 379 (1995).

[41] J. D. Lewis *et al.*, FERMILAB-CONF-94/128-E (1994).

[42] R. Akers *et al.*, *Phs. Lett.* **B316**, 435 (1993).

[43] R. Akers *et al.*, *Phys. Lett.* B350, 273 (1995).

[44] F. Abe *et al.*, *Phys. Rev. Lett.* **74**, 4988 (1995).

[45] M. S. Alam *et al.*, *Phys. Rev. Lett.* **74**, 2885 (1995).

[46] J. T. Seeman, *Ann. Rev. Nucl. Part. Sci.* **41**, 389 (1991).

[47] The SLD and SLC Collaborations, SLAC-PUB-6313 (August 1993).

[48] T. Maruyama *et al.*, *Phys.Rev. Lett.* **66**, 2351 (1991).

[49] G. Blaylock, *SLD Physics Note #22* (June 1993).

[50] S. B. Gunst and L. A. Page, *Phys. Rev.* **92**, 970 (1953).

[51] The SLD Collaboration, *The SLD Design Report*, SLAC Report 273 (1984).

[52] The SLD Collaboration, SLAC-PUB-5970 (October 1992).

[53] K. Abe *et al.*, SLAC-PUB-6569 (1995).

[54] K. Abe *et al.*, SLAC-PUB-95-6693 (1995).

[55] S. González, SLD Physics Note # 24 (1993).

[56] C. Fan, *Measurements of Gluon Spin-Sensitive Quantities at the Z^0 Resonance*, Ph. D. Thesis, University of Colorado (1993)

[57] The SLD Collaboration, SLAC-PUB-4786 (November 1988).

[58] T. Sjöstrand and M. Bengtsson, *Comp. Phys. Comm.* **43**, 367 (1987).

[59] W. Braunschweig *et al.*, *Z. Phys.* **C41**, 359 (1988); P. N. Burrows, *Z. Phys.* **C41**, 375 (1988).

[60] M. Z. Akrawy *et al.*, *Z. Phys.* **C47**, 505 (1990).

[61] C. Peterson *et al.*, *Phys. Rev.* **D27**, 105 (1983).

[62] D. Buskulic *et al.*, *Z. Phys.* **C62**, 179 (1994); B. Adeva *et al.*, *Phys. Lett.* **B261**, 177 (1991); R. Akers *et al.*, *Z. Phys.* **C60**, 199 (1993); R. Akers *et al.*, *Z. Phys.* **C61**, 209 (1994); D. Buskulic *et al.*, *Z. Phys.* **C62**, 1 (1994); P. Abreu *et al.*, *Z. Phys.* **C59**, 533 (1993); R. Akers *et al.*, *Z. Phys.* **C60**, 601 (1993).

[63] D. Decamp *et al.*, *Phys Lett.* **B273**, 181 (1991); P. Abreu *et al.*, *Z. Phys.* **C50**, 185 (1991); B. Adeva *et al.*, *Phys. Lett.* **B259**, 199 (1991); P. D. Acton *et al.*, *Z. Phys.* **C53**, 539 (1992).

[64] *Z Physics at LEP 1*, ed. G. Altarelli, R. Kleiss and C. Verzegnassi, CERN 89-08, (September 1989).

[65] T. Sjöstrand, *Phys. Lett.* **B185**, 810 (1987).

[66] S. Bethke, *Z. Phys* **C29**, 175 (1985).

[67] J. Chrin, *Z.phys* **C36**, 131 (1988).

[68] M. G. Bowler, *Z. Phys.* **C11**, 169 (1981).

[69] D. Coffman *et al.*, *Phys. Lett.* **B263**, 135 (1991).

[70] F. Butler *et al.*, *Phys. Rev. Lett.* **69**, 2041 (1992).

[71] M. Artuso, HEPSY-7-93 (July 1993).

[72] GEANT 3.15 Program, *CERN Application Software Group*, **CERN Program Library** (1993).

[73] P. Billoir, *Nucl. Instr. and Meth.* **A238**, 472 (1993).

[74] List of trigger settings for the 1993 run, unpublished document (1993).

[75] *Workbook for SLD Offline Users*, WWW pages at SLAC (1995).

[76] D. C. Williams, *The Left-Right Forward-Backward Asymmetry for B Quarks at the SLD*, Ph. D. Thesis, MIT (1994).

[77] W. Bartel *et al.*, *Z. Phys.* **C33**, 23 (1986).

[78] P. R. Bevington and D. K. Robinson, *Data Reduction and Error Analysis for the Physical Sciences*, McGraw-Hill, New York (1992).

[79] R. Akers *et al.*, *Z. Phys.* **C65**, 17 (1995).

[80] see for example R. Akers *et al.*, *Z. Phys.* **C60**, 601 (1993); D. Buskulic *et al.*, *Z. Phys.* **C62**, 1 (1994); D. Buskulic *et al.*, *Z. Phys.* **C62**, 179 (1994); P. Abreu *et al.*, CERN PPE/95-08 (1995).

[81] M. Thulasidas, Ph. D. Thesis, Syracuse University (1993).

[82] H.Albrecht *et al.*, *Z. Phys.* **C54**, 13 (1992); R. Giles *et al.*, *Phys. Rev.* **D30**, 2279 (1984).

[83] H. Albrecht *et al.*, *Z. Phys.* **C54**, 13 (1992).

[84] R. Giles *et al.*, *Phys Rev.* **D30**, 2279 (1984).